D^{*+} reconstruction in proton-proton interactions at $\sqrt{s} = 8$ TeV with the ALICE detector at the Large Hadron Collider

Annelies Veen
Utrecht University, Institute for Subatomics Physics
Student number: 3345149
Supervisors: André Mischke and Alessandro Grelli

July 13, 2014

Abstract

One of the least understood states of matter in the creation of the universe is the Quark Gluon Plasma (QGP). In order to understand more about this state heavy flavour particles are measured in collisions containing QGP and in collision without QGP. The main observable for studying the energy loss differences between both is the nuclear modification factor (R_{AA}). In this factor both a cross-section for the QGP situation and a baseline measurement, which is extracted from pp collisions, are included. The reconstruction of the D^{*+} in the hadronic channel $D^{*+} \rightarrow D^0\pi \rightarrow K\pi\pi$ using the 2012 ALICE proton-proton data at $\sqrt{s} = 8$ TeV will provide such a baseline as well as improve current perturbative Quantum Chromo Dynamics (pQCD) calculations. Cross-sections extracted from reconstructions can be used to improve the current D-meson cross-section as well as the R_{AA} which currently have high uncertainties. The limiting of these uncertainties is done by measurements at higher collision energies but the uncertainties in a measurement can also be improved via higher transverse momentum references.

In this thesis the reconstruction for D^{*+} mesons is studied with respect to the EMCal trigger, which give higher transverse momentum references than minimum biased triggers. The focus will be on the quality assurance of the data sample with respect to all D-mesons and on the signal extraction for the D^{*+} mesons. As a perspective the full correction of the raw yield and the determination of the production cross-section for D^{*+} mesons are shown.

The combination of results hints that it would be useful to keep on measuring the cross-section for triggered data, in order to increase the momenta range of the measurements. The quality assurance concludes that a new reconstruction is necessary to correct local problems. The production cross-section should be re-evaluated once the new reconstruction and the Monte-Carlo simulation for this trigger are available.

Contents

1 Preface

Writing a proper introduction is perhaps the hardest part of a thesis to write. After spending a year on the same subject, trying to understand what every single technical term means and why something is done in a certain way, one has grown accustomed to this knowledge. Anyone who has ever really learned a language fluently will understand that some things are hard to translate. In this sense physics and especially particle physics can be seen as language on its own, with every project speaking its own dialect, which, once you have learned it, is so intertwined with your language that it is hard to unlearn.
Nevertheless the introduction is also a very important part, as a good introduction can be used to help explain the research from the specialist to the curious, explaining enough of the specialists terms to make it possible for anyone to ask relevant questions. In order to satisfy the curious our introduction will consist of both a theoretical explanation, be it of a very small subsection of modern day particle physics, as well as a motivation of the research that was done in this thesis from the physical point of view.

2 Introduction

The aim of this thesis is to measure the cross-section of D^{*+} mesons in pp collisions at $\sqrt{s} = 8$ TeV at the Large Hadron Collider by using data recorded by the ALICE experiment.
This thesis is organized, as can be seen in the table of contents, by first introducing the theory and the detectors, followed by the quality assurance of the data used and finally the reconstruction process of the D^{*+} will be discussed. The second part of the thesis that focuses on the reconstruction of D^{*+} mesons contains of the extraction of the yield and the production cross-section, which is determined using the $\sqrt{s} = 7$ TeV Monte-Carlo simulations. The first part can be used as a check on the quality of the data periods, while the second part is meant to give an approximation of the results that could be extracted from these data periods.

2.1 Theoretical background

Particle physics is the branch of physics that concerns itself with the smallest building blocks of our universe and the forces that exist between them.
The standard model, is the current and most complete model for particle physics in which the electromagnetic force, the strong force and the weak force have been combined and in which the elementary particles that have been proven to exist are included. However this model is not a theory of everything. Gravity is still not included in the standard model.

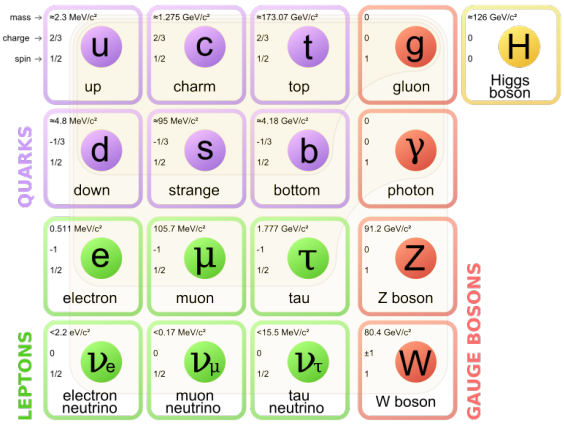

Figure 1: Standard model particles [11].

In this thesis the focus will be on the strong force, which is the force that confines quarks and gluons into hadrons. The gluons function for the strong force as photons function for the electromagnetic force; they carry the charge associated with their respective force. The strong force or strong interaction is described by Quantum Chromodynamics (QCD). Examining QCD rigorously is not within the scope of this thesis[1], but a short description of the theory will be given. Every quark has a QCD charge, which can come in three types. In order to visualize the interaction the QCD charge is called 'colour' and the different charges are named red, green and blue. In the same line of thinking every anti-quark has an anti-colour.
Given the observation that the hadrons which are detected are colourless, it has been deduced that any combinations of quarks that is allowed in this theory must give a colourless object. The combination of all three colours together is exactly neutral, thus the only particles that can be created either consist of three quarks or three anti-quarks or a quark anti-quark combination which annihilate each others colour[2]. Gluons are self-interacting force carriers, therefore it can be deduced they must contain a colour and a anti-colour.
In order to understand from the theory why there are only colourless particles the two main principles of QCD must be considered: confinement and asymptotic freedom.
Confinement is what makes it impossible to see separate colour charges. It means that if the distance between a quark-anti-quark pair increases, before it reaches a point where they could be considered separate, there is a point where it is energetically favourable to create a quark/anti-quark pair in between the two pairs and thus single quarks will not be seen.
However here the focus will be on the asymptotic freedom. This principle states that the strong interaction weakens when the distance between the particles diminishes. From this it can be imagined that if the energy and particle density are high enough, like in the situation is a few μs after a complex collision, a system of freely interacting quarks and gluons could be found. This hypothesized situation is a Quark-Gluon Plasma [14] (QGP), which is also the state in which we think the universe must have been a few μs after the big bang. However it is also one of the least understood "states" in current days physics.
As quarks cannot be measured directly because they are bound in hadrons different types of probes are used. For these probes hadronised quarks are used that are formed in different

[1] For that [21] or [25] would be suitable sources.
[2] In principle a multiple could also be possible but these states are not energetically favourable.

stages of the collision evolution and hadronise into particles. In order to see if this hypothesized state exists the difference between situations in which a QGP could be possible and situations in which this was not possible can be examined. This is for example done by measuring the amount of particles with a certain transverse momentum, momentum which is in the direction perpendicular to the direction of the partial beams, for both situations. The heavy flavour hadrons such as the D^{*+} can not be measured directly, thus its decay products are measured and then the yield is reconstructed. This is then corrected via Monte-Carlo simulations in order to compensate for detector effect and for the requirements that are used to extract a clean signal. A further explanation of the reconstruction and corrections can be found in chapter 5.

2.2 Physics motivation

The production of hadrons containing heavy quarks is studied in order to test the calculations of (perturbative) QCD processes. These pQCD calculation of the cross-section are done by using the parton distribution function for the incoming protons, the parton hard scattering cross-section is calculated perturbatively with the strong interaction coupling constant and the fragmentation functions are used to calculate the hadronization process to D^{*+} with a certain momentum. These calculations are done at the perturbation level of next-to-leading order or at fixed order with next-to-leading-log re-summation (FONLL) [9] and describe the production cross-section of charmed hadrons in proton-proton (pp) collisions at the CERN Large Hadron Collider. Experimental results for the production cross-section of the D^* can be used to further improve these pQCD calculations.
Moreover the results of this cross-section can also be used as a baseline for studies with respect to Quark Gluon Plasma (QGP). As mentioned in the theoretical introduction this is the state in which the universe was a few μs after the big bang, and this state is also found μs after a lead-lead (Pb-Pb) collision according to QCD calculations. As the creation time of a parton is of the order $1/m$ with m the mass of the particle the quarks and gluons from the primary collision are created at an earlier time then the QGP state arises, with the QGP forming a medium through which these particles travel. The quarks interact with the medium which results in parton energy loss, this energy loss comes from both gluon radiation and collisions with other particles. This energy loss is larger in gluons than in quarks, and in the heavy quarks, which will be studied in this thesis, the additional so called dead-cone effect reduces the small-angle gluon radiation[27]. Thus for these heavy quarks other in medium effects be stronger effect than the gluon radiation and collisions, and low momenta particles may to some extent be thermalized in the medium. Because these heavier quarks are less influenced by the medium, the chance that such a particle will be absorbed in the medium is very small, while this is a higher chance for light quarks and gluons.
The charm quark is studied here because hadronization of heavy quarks is only possible for the charm and beauty quark, these can either couple to a light quark creating B/D mesons or couple to their own anti-particle. Of the B/D mesons the D-mesons are more abundant, because they are lighter and thus more easily produced. To clarify the former, when the measurements of D-mesons are mentioned, what is meant is that these particles are reconstructed from the decay products that have been measured.
In order to calculate the strength of the aforementioned effects of the QGP a difference factor between the two situations is calculated: the nuclear modification factor the R_{AA}[26]. This observable is used to compare the yield with respect to momentum created in both, compensated ($\langle N_{bin} \rangle$) for the fact that there are more particles that collide in lead-lead (AA) collisions than in a simple pp collision. Thus,

$$R_{AA} = \frac{1}{\langle N_{bin} \rangle} \frac{\mathrm{d}^2 N_{AA}(p_T)/\mathrm{d}p_T \mathrm{d}y}{\mathrm{d}^2 N_{pp}/\mathrm{d}p_T \mathrm{d}y}, \tag{1}$$

which should be equal to 1 if there is no medium created in lead-lead collisions. However if a QGP was created then 'quenching' would be expected, lowering the momenta of those quarks traversing through the medium, creating a suppression of hadrons at higher momenta ($p_T \gtrsim 2$ GeV/c). The relative size of the suppression is an observable for the strength of the interaction with the medium, and can be compared with the R_{AA} for particles coming from

other quarks to test the mass dependence of the parton energy loss in this medium.[3]

[3]This section is based loosely upon [4] and [5]

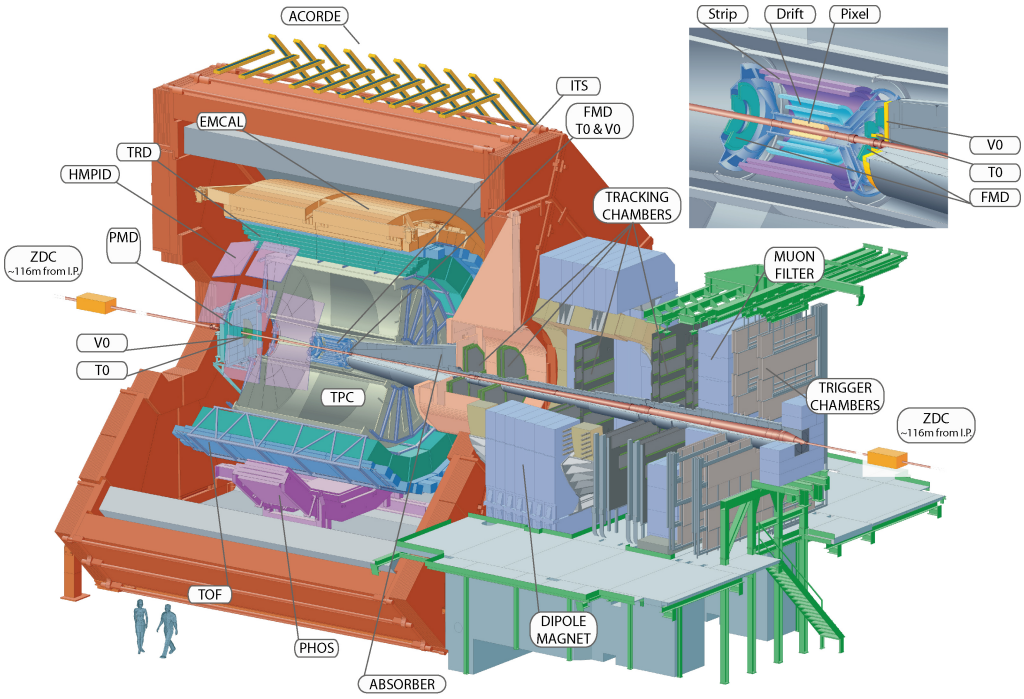

Figure 2: Layout of the Alice detector [22].

3 The ALICE experiment

3.1 General description

In this chapter a brief description of the detectors used in ALICE will be given. ALICE is the abbreviation of A Large Ion Collider Experiment, and it is one of the four major experiments at the Large Hadron Collider (LHC) at CERN, the European Organization for Nuclear Research. The ALICE detector has been build to study high multiplicity lead-lead collisions, focusing on the investigation of the existence of Quark Gluon Plasma (QGP) and searching for the properties of this plasma.
However the experiment does not only study the lead-lead collisions, which the ALICE detectors are specialized in. ALICE is also used to study proton-proton collisions as a baseline, as the difference between multiple proton-proton collisions and a lead-lead collision is how QGP effects are studied. At the same time these results are also used to confirm or disprove the other main experiments in the areas it can compete with them [24].
In this thesis some of the main detectors used in ALICE [3] will be discussed. For more information the ALICE homepage is advised, as well as the references given.
Figure 2 shows the layout of the detectors on the experiment barrel and zooms in on the central part containing some primary triggers, as well as the FMD and ITS.
The main primary triggers that are of particular interest to us are the T0 and V0, and in terms of the larger detectors the focus will be on (ordered from inside to the outside) the ITS, TPC, TOF and EMCal.
The primary triggers will be studied in comparison to the EMCal trigger, the ITS and TPC will be used for the tracking and the TPC and TOF will be used for the particle identification. There are many other (sub)detectors, however this thesis can not address them all. For those detectors that are not explained in detail the full name will be given and/or a short explanation of the possible uses of the detector will be given[4].
Starting from the beam and going to the outer detector components and ordered by significance to this analysis there are:

[4]In most cases a reference will be given, for those detectors that will be discussed in more detail the reference will be in the associated section.

- ITS, Inner Tracking System. (More information in section 3.2.3)
- TPC, Time Projection Chamber. (More information in section 3.2.4)
- TRD, Transition Radiation Detector. This is the main electron detector.[13]
- TOF, Time Of Flight detector. (More information in section 3.2.5)
- HMPID, High Momentum Particle Identification.[15]
- PHOS, Photon Spectrometer. [28]
- EMCal, Electro Magnetic Calorimeter. (More information in section 3.2.2)
- PMD, Photon Multiplicity detector.[6]
- FMD, Forward Multiplicity detector. It detects charged particles created in collisions with small angles with respect to the beam pipe. [10]
- ACORDE, Alice Cosmic Ray Detector. [17]

All these detectors are all centred around the beam interaction area, a little bit further along the beam pipe there are two more detectors:

- ZDC, Zero Degree Calorimeter [20]
- Muon Spectrometer (containing trigger and tracking chambers).

At the far end a dipole magnetic is placed which is used to maintain the magnetic field and a muon filter.
Having explained the names of the main detectors, the primary triggers and the EMCal, ITS, TPC and TOF will be discussed a bit more. This is structured in the following way: first the detectors that have a trigger which will be used in this analysis are discussed (T0,V0 and EMCal), followed by the ITS, TPC and TOF.

3.2 Main detectors for this analysis.

3.2.1 T0 and V0

The detectors that are used as basic unbiased triggers are called the T0 and V0 in figure 2. Both of them will be addressed in a bit more detail.

T0
The T0 has been designed to be a trigger detector, it consists of two sets of Photon Multiplier Tubes (PMTs) with Cherenkov radiators. These two sets are on opposite sites of the Interaction Point, covering $-3.3 < \eta < -2.9$ and $4.5 < \eta < 5$. By its position the detector works as a primary trigger, a signal for some of the other detectors to start measuring as well as giving a very precise timing of the collision (resolution σ better than 50ps).
As ALICE mainly focuses on lead-lead collision, the T0 has a trigger efficiency up to 100% for AA collisions, but only about 50% for pp collision.
The output of this trigger contains a collision time, an approximate position of the primary vertex and a rough idea for the multiplicity (only used in AA).
The triggers is build out of separate trigger units. These units contain Cherenkov radiators, which contains a small volume with a dielectric, in this case Quartz. Here the Cherenkov radiation[5] is created upon passing of a charged particle, this light will set of the PMTs. If there is a signal from the sets of PMTs on both sides, within reasonable time of each other, it is considered an event and gives the output as said before.
This vertex trigger is used as minimum bias trigger base for the "8" offline triggers, which will be mentioned in section 4.2.[6]

[5]Cherenkov radiation is seen when a charged particles goes through a dielectric medium at a speed greater than the phase velocity of light in that medium. Which polarizes the molecules, which then fall back to the ground state while emitting radiation.

[6]Note that this section in strongly based upon [10], which contains more information on both the T0 and the V0 detectors.

V0
The V0 is also used as trigger, usually a centrality trigger, and to reject background for the di-muon arm. This detector has a larger pseudorapidity coverage (mainly $-3.7 < \eta < -1.7$ and $2.8 < \eta < 5.1$) containing of 2 disk of plastic 8 segment scintillator tiles that are read out by optical fibres. However it is not precise enough to give the position of the vertex or the timing information.
This detector is quite simply built of scintillator plates, and is used as a minimum-bias trigger for the central barrel detectors. A very important role of this trigger is a centrality determination in $Pb-Pb$ collision through the signal amplitude that is measured by the scintillators. However, note that this means that not all particles will have arisen from the primary collision. Thus very precise cuts on this trigger are needed.
The V0 is not only of use in lead-lead collisions but also function as minimum-bias trigger for pp collision. The detection rate is 77% for situations in which the V0 only is studied and a detection is made if there is a signal in both sides of the detector, which is a about 1.5 times as much as that of the T0. This trigger is the base for the "7" triggers of the offline trigger as will be discussed in section 4.2.

Both triggers mentioned above are minimum bias L0 triggers.[7]

3.2.2 EMCal detector

As has been shown in figure 2 the EMCal detector is sandwiched between the magnet coils and the frame that supports the central detector. The azimuthal coverage is 107 degrees and the pseudorapidity coverage is $-0.7 < \eta < 0.7$[8].

The Electro Magnetic Calorimeter is a detector segmented into so called Super Modules that span approximately 20 degrees in the azimuthal direction. These Super Modules themselves contain modules that are approximately projective in the η direction, and each such a module (12,288 in total) is a self-contained detector unit. Each unit contains a detecting sandwich of Lead tiles, scintillator tiles and Bond paper sheets, of 538 layers (in total) thick.
Focusing on the triggers coming from the EMCal, it has a L0 trigger used for the EMCal 7 and 8 triggers. But it also contains a L1 trigger which is used in the first 6.5μs after an event and can be used to reject a certain event not qualifying for its trigger.

In the EMCal the basic trigger sends a readout of the Super modules to the Trigger Region Units (TRU), which digitizes it and gives the image its input projected on space time. There is one Trigger Region Unit per area. The trigger threshold has to be met in a Trigger Region Unit, so only local regions.
The second part of the trigger then uses all the data combined. It is therefore called the Summary Trigger Unit or STU. This part is mainly used in studies of QCD jets as these will hit more then just one TRU's area and as a way to get rid of heavy ion background (ions not produced as a product of some hard scattering in the primary collision) it also requires a V0's multiplicity input. A further explanation of the trigger for the 8 TeV pp-collision situation can be found in section 4.2.

3.2.3 Inner Tracking System

The ITS, or Inner Tracking System, consists of 6 layers equipped with 3 different silicon detector technologies. It has vertexing, tracking and particle identification capabilities. In particular it extends the ALICE tracking and particle identification down to $p_T > 100$ MeV/c. The two innermost layers are made of Silicon Pixel Detectors, (SPD) which have a very good spatial resolution (precision is 12 μm in the $r\phi$ direction), followed by two layers of Silicon Drift Detectors (SDD) which are both flat plates wrapped around the central tube. For the outer two layers less precision is needed and thus these have been made out of Silicon Strip Detectors (SSD), instead of the plates of the others. The SPD layers allow to achieve the required impact parameter resolution and serve also as a trigger. The SDD and SSD

[7]Name for a trigger that is within 1.2 μ s after collision.
[8]Information in this section is taken from [19].

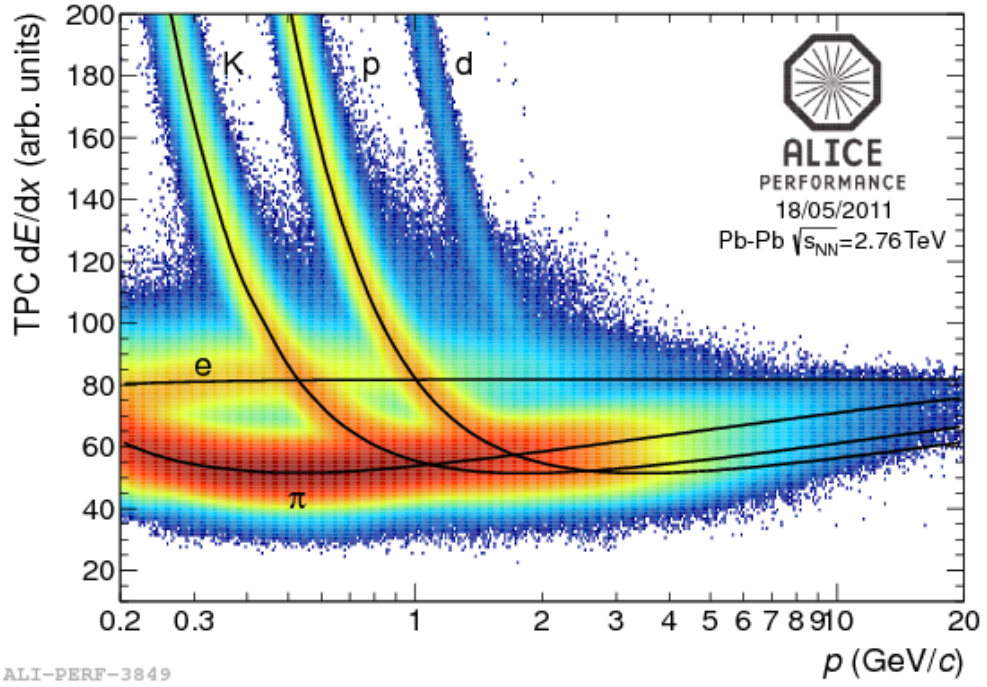

Figure 3: Specific ionization energy loss versus momentum in Pb-Pb collisions at $\sqrt{s_{\rm NN}} = 2.76$ TeV [16].

have particle identification capabilities via the measurement of the energy loss dE/dx in the material.[9]
From the primary tracking and because of the good resolution the ITS is used for finding the primary and secondary vertices, and it is optimized to do that.

3.2.4 Time Projection Chamber

The Time Projection Chamber is a gas chamber with multi wire readout chambers on both ends (based upon Multi-Wire Proportional Chamber). It has an central electrode and a Field Cage to keep an uniform electro-static field in the gas.[10] In principle the detector works by using that charged particles traversing through the detector ionize the gas and lose energy. The ionization electron then drifts to the detector chamber under the influence of the electro-static field. Thus giving the energy loss of the particle travelling through and a very precise path it has travelled, using also the arrival time with respect to the collision time. The last two combined also give us the momentum of the particle.
The amount of energy loss will thus be the amount of signal that is received from the particle. A typical distribution for the specific energy loss is shown in figure 3.

From figure 3 it can be seen that the low momentum particles are easy separable, thus the TPC Particle Identification would be expected to make the best difference in relatively low p_T.
In the previous section it was mentioned that the ITS measures energy loss in the two outer layers. For this analysis this will not be used. Instead the TPC will be used as a particle identification detector, because this probes higher momenta. With tracking the path (track) a particle takes through the detector is meant, using the extra information the different detectors give us to find the momentum, the mass and thus the identity of the particle. The tracking is usually done via a combination of TPC and ITS signals. The low p_T reach of the

[9]For more information see the technical report https://edms.cern.ch/file/398932/ 1/ ITS_TDR.pdf, on which this section has been based.
[10]For more information please see [7].

tracking is possible via the ITS and it complements the TPC elsewhere. The combination is the most common form of tracking and thus a rough explanation of how that is done will be given. The actual tracking is backtracking, as it start from the outer edge of the TPC and then works back with use of a Kalman Filter algorithm through the TPC. Finally it compares such a track with the the most likely paths in the ITS, by checking the χ^2 and using a vertex constraint. In this way the most likely path is found, in order to also see the low energy particles that would not hit the TPC, after the tracking has finished all clusters (hits in the ITS) that were used in the tracking are removed. As a final step those tracks that are not yet used are studied to find the low momenta particles that would not have reached the TPC.

3.2.5 Time of Flight detector

The Time of Flight detector also works with gas, but instead of it being a gas chamber it has gas between its plates. It consists of so called Multi-gap Resistive Plate Chamber detectors. It looks like a cylindrical shell around the other detectors. The TOF measures the exact time in which a particle reaches it, and if possible compares it with the event time as given by the T0. However if this is not triggered (as happens more often in pp then lead-lead collisions), it can also calculate the zero-time from its own hits. In order for it to be able to calculate the event time, it does however need to have at least 3 hits, and this method of calculating the zero-time produces a significantly larger uncertainty.
The found time difference is then compared to the momentum of the particle and from this the mass of the particle can be extracted, using basic relativity principles. The difference is found to be around 3σ for particles with momentum above 1 GeV/c and below 2.5 GeV/c for the difference between pion and kaon or above 1 GeV/c and below 4 GeV/c for kaon and proton. The detectors can be used from a momentum of 0.3 GeV/c but gets increasingly better till 1 GeV/c. After that point it is stable in signal quality, but as the mass difference with respect to the momenta becomes very small at some point it becomes less reliable than 3σ.
These two identification methods of the TOF and the TPC are very different and using them next to each other will decrease the error on the results. Furthermore the momentum ranges on which each detector is most effective [11] do not completely overlap so for the lowest sector the TPC is more accurate while for the particles above 2 GeV/c the TOF is more accurate than the TPC.

3.3 Software environment

For this thesis the software packages ROOT [2] and AliRoot [23] were used. ROOT is a framework written in `C++` that is used by many of the LHC experiments, it has been built especially with particle physics in mind and contains many pre made packages. For their use, the ALICE collaboration has assembled a set of useful packages called AliRoot, as an extension of the packages given by ROOT. AliRoot contains folders that are specific to either a detector or a research group. The main folder used in this analyses was the PWGHF (Physics Working Group Heavy Flavour), and then mainly the codes inside the vertexingHF folder.
Specifically, the *AliAnalysisTaskSEHFQA* task has been used for the quality assurance and has been improved with some extra distributions necessary for questions that arose from the quality assurance. In the same way the macro *DrawQAoutput*, which is used to give the output, has been changed to deal with multiple datasets or trigger in the same figure, the changes in both have been propagated to the central code repository.
As most of the calculations would take too much time on a regular desktop, the World Wide Computing GRID [12], was used to perform calculations. This is a network of computer farms across the world working mainly on physics calculation. In order to interface fluently with the GRID AliEN [1] was used, which is the specific GRID-handler used by the ALICE experiment, as well as using the web interface MonALISA, also known as the Alimonitor.

[11] Very low momenta for the TPC and slightly higher momenta for the TOF with an optimum between 1 and 2.5 GeV/c

4 Data sample and quality assurance of 8 TeV pp collision data

Large amount of quality assurances are done in order to guarantee the quality of the measurements as much as possible. First during the data taking, later at the reconstruction level and finally at the analysis level. This last check is done both to guarantee the quality and to make sure that data that had earlier been discarded, or labelled for special purposes is not accidentally used in normal physics analyses. In this thesis the quality assurance at analysis level will be discussed in finer detail.
For the 2012 pp collisions at $\sqrt{s} = 8$ TeV data these last checks, with respect to all the D-mesons, were done by a large subsection of the D2H group. A short overview of the results will be given in order to put the results obtained at later stage in proper perspective.
At the analysis level the multiplicity distributions of the tracks, the tracklets[12] and the selected tracks are studied, in order to check the trigger (effects) and the pile-up removal settings.
The p_T distribution of the good tracks[13] is also checked.
The vertex position distribution is checked in the z direction for the selected events, to see if the required restriction was performed properly.
The functioning of the ITS is checked by the amount of tracks with a point in a certain layer, which is of special interest as the SPD improved during the data periods.
Specifically for the D-meson group the impact parameters $d_{0,r\phi}$ and $d_{0,z}$ have also been checked for the selected tracks versus the decay products of the D^0 mesons.
And last of all the particle identification was checked by checking the results found from the TOF and TPC detectors.
The functioning of the most primary detectors for all data groups is checked partially during the data taking. However, just because a detector worked correctly does not mean that the reconstructed results are automatically correct. Differences can occur due to for instance a small change in the normalization of a detector or a shift in the threshold of a trigger. While these changes can be a positive influence for the data collection, they will effect the measurements and normalisations must be taking into account for the reconstruction.
Before mentioning the results of the quality assurance, the data sample will be defined and the different triggers for which the quality assurance has been done will be addressed. To the earlier mentioned quality assurance a check on the possible overlap between the triggers was added. Overlap between triggers is not a bad thing in first principle. If, for instance, a minimum bias trigger data sample is wanted the trigger should not be excluded because there are other active triggers. Elaborating on this, if a biased trigger selects events in which there is a particle with a certain momentum, the minimum bias trigger would become biased if no overlap is allowed. However to make sure problematic or atypical events are not used multiple times because of overlap, the fired triggers after selection were checked for overlap with other triggers.

[12] Tracks that come purely from the ITS
[13] Tracks that are reconstructed and have at least one cluster reconstructed in the SPD as well as $p_T > 0.3$.

4.1 Data sample

In table 1 the run lists are given for data sets A till G.

Period	run list
LHC12A	177182, 177173, 177167, 177160, 177157, 177011, 176929, 176927, 176926, 176924, 176859, 176854, 176849, 176753, 176752, 176749, 176730, 176715, 176704, 176701, 176661
LHC12B	178163, 177942, 177938, 177869, 177861, 177860, 177858, 177804, 177799, 177798, 177671,177624, 177620, 177612, 177601, 177597, 177592, 177580
LHC12C	182744, 182741, 182740, 182730, 182729, 182728, 182725, 182724, 182692, 182691, 182687, 182684, 182635, 182624, 182325, 182324, 182323, 182322, 182302, 182300, 182299, 182297, 182295, 182289, 182207, 182111, 182110, 182106, 182023, 182022, 182018, 182017, 180720, 180719, 180717, 180716, 180569, 180567, 180564, 180562, 180561, 180517, 180515, 180510, 180501, 180500, 180230, 180201, 180200, 180199, 180195, 180133, 180132, 180131, 180130, 180129, 180127, 180044, 180042, 180000, 179920, 179919, 179918, 179917, 179916, 179859, 179858, 179803, 179802, 179796, 179639, 179621, 179618, 179591, 179585, 179584, 179571, 179569
LHC12D	186320, 186319, 186318, 186229, 186208, 186205, 186200, 186167, 186165, 186164, 186163, 186162, 185912, 185909, 185784, 185778, 185776, 185775, 185768, 185765, 185764, 185757, 185756, 185738, 185735, 185734, 185701, 185699, 185698, 185697, 185695, 185687, 185680, 185589, 185588, 185583, 185582, 185581, 185580, 185578, 185575, 185574, 185565, 185563, 185474, 185465, 185461, 185457, 185375, 185371, 185363, 185362, 185361, 185360, 185359, 185356, 185351, 185350, 185349, 185303, 185302, 185300, 185299, 185296, 185293, 185292, 185291, 185289, 185288, 185284, 185282, 185221, 185217, 185208, 185206, 185203, 185198, 185196, 185189, 185164, 185160, 185157, 185134, 185132, 185127, 185126, 185116, 185031, 185029, 184786, 184784, 184687, 184682, 184678, 184673, 184371, 184215, 184209, 184208, 184188, 184138, 184137, 184135, 184132, 184127, 183916, 183913
LHC12D-M	184990, 184988, 184987, 184968, 184967, 184964, 184938, 184933, 184928
LHC12E	186602, 186601, 186598, 186514, 186511, 186508, 186507, 186460, 186459, 186453, 186429, 186428, 186389, 186388, 186387, 186386, 186385, 186365
LHC12F	188101, 188093, 187849, 187796, 187791, 187785, 187753, 187749, 187739, 187698, 187697, 187695, 187656, 187633, 187627, 187624, 187623, 187561, 187560, 187537, 187536, 187510, 187508, 187489, 187488, 187487, 187486, 187485, 187484, 187343, 187341, 187340, 187339, 187203, 187202, 187201, 187152, 187151, 187150, 187149, 187143, 187136, 187084, 187047, 186992, 186990, 186989, 186987, 186969, 186967, 186966, 186965, 186938, 186937, 186857, 186853, 186851, 186845, 186844, 186838, 186815, 186809, 186807, 186692, 186690, 186668
LHC12G	188503, 188500, 188499, 188490, 188455, 188454, 188449, 188448, 188447, 188446, 188444, 188443, 188442, 188440

Table 1: Run lists for the 2012 pp data.

Furthermore for future references table 2 has been added containing the amount of events per trigger for those triggers mentioned either in the quality assurance or in the D^{*+} reconstruction later on. Note that this is the amount of events that is useful for analysis, so those events which cannot be used, because they have reconstructed vertices outside 10 cm from the centre of the ITS for instance, have not been taken into account.

In order to further explain the data the various triggers used in this set will be explained in more detail. This explanation will contain the trigger details for the trigger that will be mainly used for the D^{*+} analysis, the EMC7 trigger.

Period	Trigger	Number of events
LHC12A	INT7	12.5 M
	EMC7	0.11 M
	SPI7	1.04 M
LHC12B	INT7	11.6 M
	EMC7	0.84 M
	SPI7	0.75 M
LHC12C	INT7	12.9 M
	EMC7	11.8 M
	SPI7	11.8 M
	EMCJET7	0.82 M
	EMCGAMMA7	0.35 M
LHC12D	INT7	13.6 M
	EMC7	13.9 M
	SPI7	9.65 M
	EMCJET7	1.52 M
	EMCGAMMA7	0.91 M
	EMCJET8	0.2 M
	EMCGAMMA8	0.1 M
LHC12E	INT7	0.82 M
	EMC7	1.31 M
	SPI7	0.99 M
	EMCJET7	0.11 M
	EMCGAMMA7	0.04 M
	EMCJET8	0.02 M
	EMCGAMMA8	0.01 M
LHC12F	INT7	5.32 M
	EMC7	5.60 M
	SPI7	4.77 M
	EMCJET7	0.45 M
	EMCGAMMA7	0.2 M
	EMCJET8	0.16 M
	EMCGAMMA8	0.07 M
LHC12G	INT7	4.52 M
	EMC7	1.23 M
	SPI7	1.27 M
	EMCJET7	0.09 M
	EMCGAMMA7	0.04 M
	EMCJET8	0.03 M
	EMCGAMMA8	0.01 M

Table 2: Statistics per trigger in the 2012 pp data, per data period.

4.2 Different offline triggers

There are different trigger detectors, as was explained in chapter 3. These detectors have some sort of threshold. One, or a combination of those thresholds, couples to an offline trigger. There are minimum bias and biased triggers that were considered for these data periods. The minimum bias triggers were INT7, INT8, SPI7 and SPI (which is of the SPI8 class). Between these triggers the INT7 and INT8 look respectively at the V0AND and the 0TVX trigger[14]. While the biased triggers were EMC7 and EMC8 as EMCal triggers[15] with the EMCEJE(7/8) and EMCEGA(7/8), the jet (patch) and photon triggers triggers using the EMC7/EMC8.
First the method used by the EMCal trigger will be explained and then a short explanation of the effects of triggering with the biased EMCal trigger will be given. The EMCal triggers on the energy of photons/pions/ηs or electrons, setting a threshold on this, selecting only those collisions that have enough energetic particles available. If there are such particles found in the EMCal that implies that the primary collision must have created particles with high energy.
The trigger works as shown in figure 4.

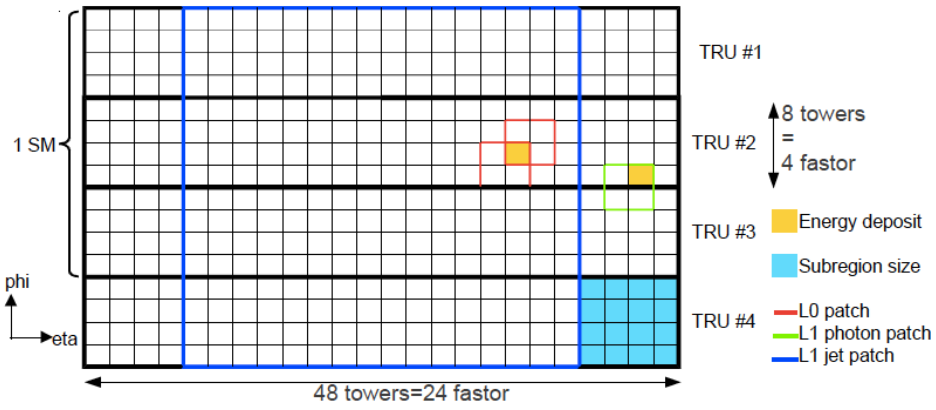

Figure 4: Sketch of the EMCal triggers

The L0 trigger is the one used for the EMC7 and EMC8 triggers, and triggers at a minimum energy in one of the EMCal towers. For periods LHC12A and LHC12B this was varying a lot between 106,92 and 80 ADC, which correspond to ADC energies of 8.3, 7.2 and 6.3 GeV and cluster energies of 2.01, 1.75 and 1.52 GeV. The cluster energy of the trigger could be expected to strongly influence the results, as events with particles with energies below or around this threshold have a far smaller chance of being inside this trigger. As periods LHC12C till LHC12G all have the same energy scales of 106 ADC and 2.01 cluster energy these data periods should be used for any EMCal triggered data set. The L0 trigger uses patches as shown in figure 4 (4×4 cells) sliding over each other (by slides of 2 cells), to cover uniformly the acceptance of the L0 unit. The L1 triggers are used for the EMCEJE and the EMCEGA, with first patch taking a trigger over 32×32 cells while sliding 8 cells, and the second calculation over the hardware borders of the detector. The thresholds are 200 ADC and 130 ADC, therefore some overlap between these last two triggers would be expected.
Thus by triggering in this way the chance that heavy hadrons have been created, with respect to the amount of collisions measured, increases due to the exclusion of collisions with too low energy. As a downside, low momenta heavy hadrons will created low momentum decay products which do not set of the trigger, thus a collision with slow heavy hadrons will also be excluded. Thus less of these slow hadrons will be found then were available in all collisions.
So by choosing to use an EMCal trigger, the data sample used becomes biased, as certain certain sets of data are excluded. Only those collision with electrons or photons of a certain

[14]The V0AND is a V0 vertex trigger and the 0TVX is a T0 vertex trigger, See section 3
[15]The former is CINT7 suite, and the later CINT8 suite. (A trigger being suite means the biased should be looked at with respect to that trigger)

energy are chosen, thus ensuring there are multiple charged particles. This increasing the chance of finding the heavy hadrons, such as D-mesons on which the D2H focuses. However it should be taken into account that there will have to be a correction for this chosen bias. For instance there will be no or very little heavy hadrons with a transverse momentum (GeV/c) below the threshold in GeV and that especially the lower momenta range could be underestimated with respect to the higher range. However this bias is worth it if a clearer and easier extractable signal can be found, which should be the case because some background, that would normally be hard to extract, will be eliminated.
For the D^{*+} reconstruction the EMC7 trigger will be considered and for comparison the SPI7 and the INT7, but for possible correlations also the jet and photon triggers should be considered. This thesis will not contain all figures, but mainly those for the last named triggers.[16]

4.3 Multiplicity distributions and momenta distributions.

4.3.1 Multiplicity distribution of the tracks

Firstly the differences between the multiplicity of the tracks in the different data taking periods will be discussed. For the periods 12A till 12G. In order to compare them a trigger that was used in most periods had to be chosen, in this case the EMCal JET 7.[17]

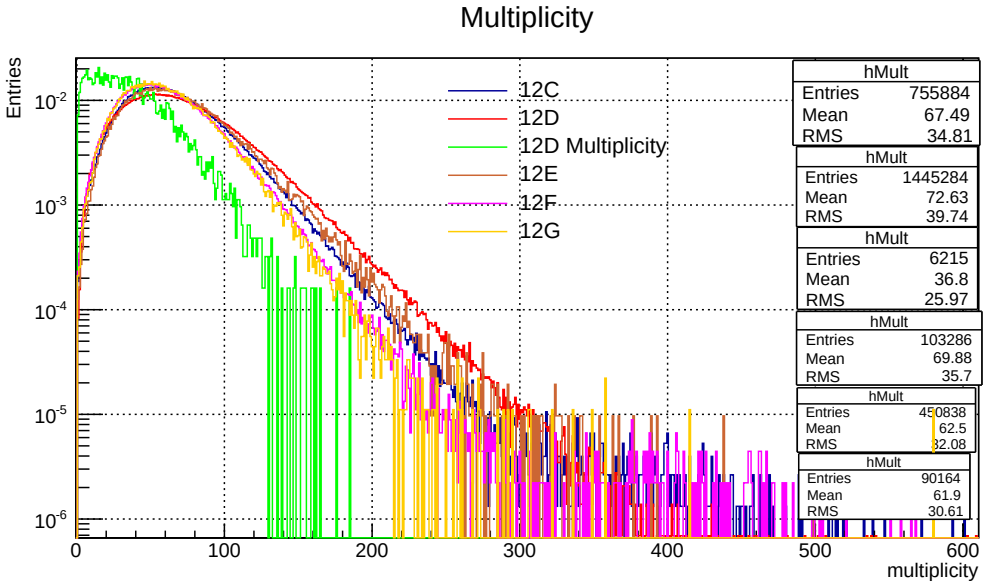

Figure 5: Multiplicity distribution of data period LHC12C/D/E/F/G, with trigger EMCal JET7, normalized with respect to the integral.

[16] For more information on the QA figures one is referred to the presentation that was given by Chitrasen Jena (University of Padova and INFN) during the ALICE miniweek (12 November 2013) and the analysis note written by Chiara Bianchin (Utrecht University). Note that the analysis note will contain a reasonable overlap with this thesis as the plots have been discussed by the author and Chiara Bianchin and some conclusion are based upon this analysis note.

[17] To finalize the QA also data periods 12H and I were discussed, however as the differences between the triggers were not considered interesting, only the multiplicity distribution for the INT7 trigger was discussed and has been found to be reasonable for both data periods

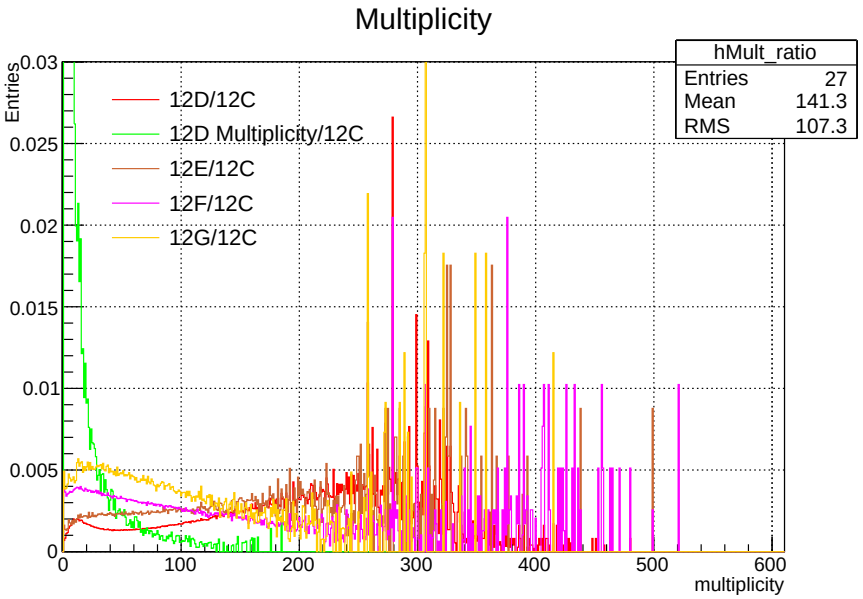

Figure 6: Ratio between the Multiplicity distributions of data period LHC12D/E/F/G with respect to period LHC12C, with trigger EMCal JET7, normalized with respect to the integral of each ratio.

As can be seen in figure 5 the set (incorrectly) called 12D multiplicity is completely off. This is not so strange per se, as the runs in this group were not meant for normal analysis, but for calibration purposes. These runs are therefore not used in this analysis. Note that there are quite some differences between the runs, which is something that had not been expected a priori. For period LHC12F there is a strong tail in the multiplicity (see figure 6) which was not expected to be there, for period D an overall slightly higher multiplicity distribution is noticed.

To give a more complete picture the the other multiplicity checks on EMCal JET 8 and EMCal GAMMA 7 and 8 will be shown. The distributions are shown in the same way as the EMCal JET 7: containing only one trigger and comparing the different periods, figures 7 to 12, the first two are concerned with the EMCal JET 8 trigger, followed by the EMCal GAMMA trigger 7 and finally EMCal GAMMA 8.

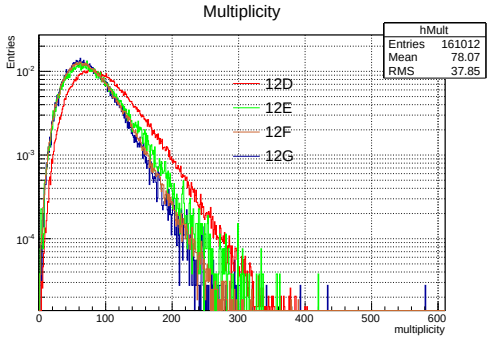

Figure 7: Multiplicity distribution of data period LHC12D/E/F/G, with trigger EMCal JET8, normalized with respect to the integral.

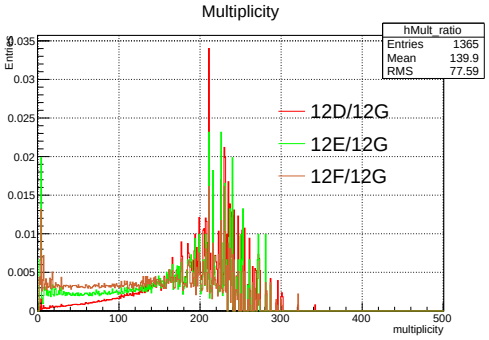

Figure 8: Ratio between the Multiplicity distributions of data period LHC12D/E/F with respect to period LHC12G, with trigger EMCal JET8, normalized with respect to the integral of each ratio.

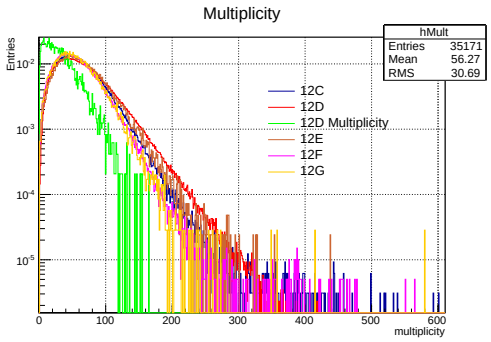

Figure 9: Multiplicity distribution of data period LHC12C/D/E/F/G, with trigger EMCal GAMMA7, normalized with respect to the integral.

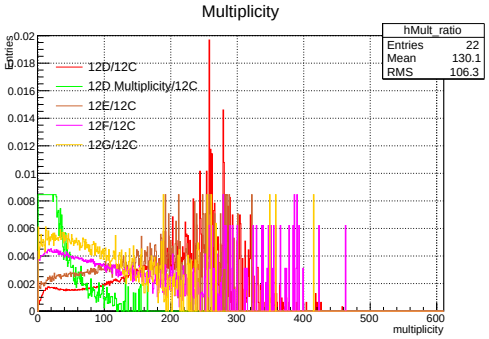

Figure 10: Ratio between the Multiplicity distributions of data period LHC12D/E/F/G with respect to period LHC12C, with trigger EMCal GAMMA7, normalized with respect to the integral of each ratio.

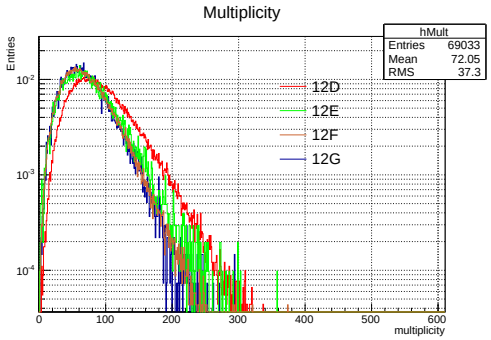

Figure 11: Multiplicity distribution of data period LHC12D/E/F/G, with trigger EMCal GAMMA8, normalized with respect to the integral.

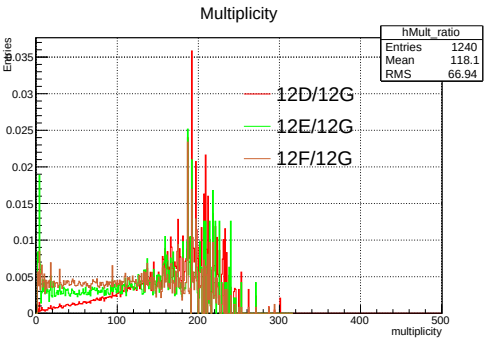

Figure 12: Ratio between the Multiplicity distributions of data period LHC12D/E/F with respect to period LHC12G, with trigger EMCal GAMMA8, normalized with respect to the integral of each ratio.

From figures 7 till 12 one can conclude that the same effects are visible in the other triggers, there is a hint that the EMCal 8 triggers might be less influenced then the EMCal 7 triggers. In order to confirm this suspicion the triggers within one period are compared to each other for data taking period for data periods LHC12D, LHC12E, LHC12F and LHC12G.

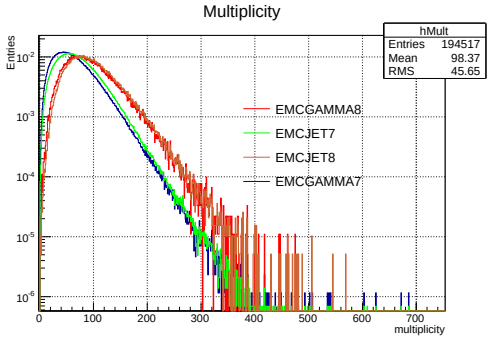

Figure 13: Multiplicity distribution of data period LHC12D with triggers: EMCal JET7, JET8, GAMMA7 and GAMMA8. The distribution have been normalized with respect to their integral.

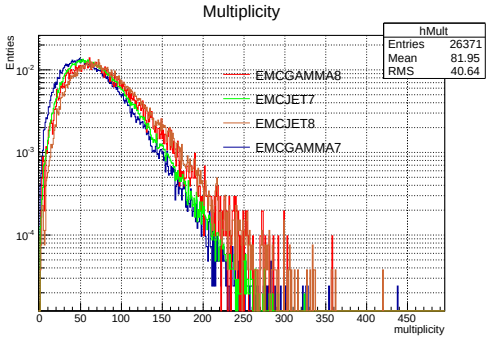

Figure 14: Multiplicity distribution of data period LHC12E with triggers: EMCal JET7, JET8, GAMMA7 and GAMMA8. The distribution have been normalized with respect to their integral.

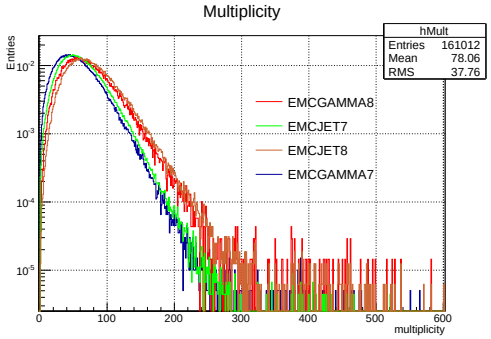

Figure 15: Multiplicity distribution of data period LHC12F with triggers: EMCal JET7, JET8, GAMMA7 and GAMMA8. The distribution have been normalized with respect to their integral.

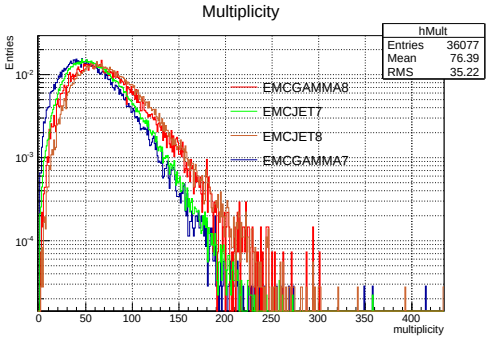

Figure 16: Multiplicity distribution of data period LHC12G with triggers: EMCal JET7, JET8, GAMMA7 and GAMMA8. The distribution have been normalized with respect to their integral.

Figures 13, 14, 15 and 16 imply that a larger difference exists between the EMCal7 and EMCal8 types than between the gamma and jet triggers. Only these data periods are shown as EMCal 8 type triggers were only seen in period 12d,e,f and g. The difference between these triggers is most likely due to the fact that the EMCal 8 triggers have a more effective background rejection for non physics interactions. However as the number of events is a lot smaller for these triggers one can not simply choose these triggers for the D mesons analyses. To check if the multiplicity tail for period F and the higher multiplicity for period D, are inside the ITS part the tracklet multiplicity distribution has to be checked as well. The tracklets are those (parts of) tracks, purely coming from at least two points in the ITS with small radial distance with respect to the primary vertex. The tracklet multiplicity distribution has an increased low multiplicity distribution. There is a stronger deviation between 12D and the other periods than was seen for the multiplicity distributions of the tracks with respect to the other periods.

4.3.2 Multiplicity distribution of the tracklets.

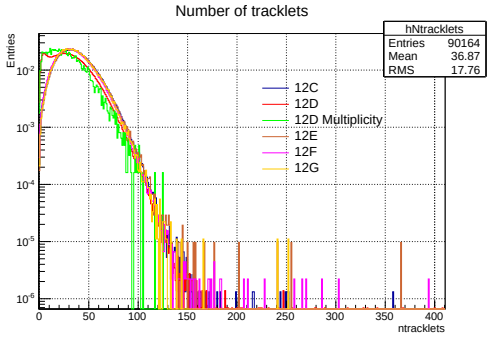

Figure 17: N-tracklets distribution for data period LHC12C/D/E/F/G with trigger EMCal JET7. The distributions have been normalized with respect to their integral.

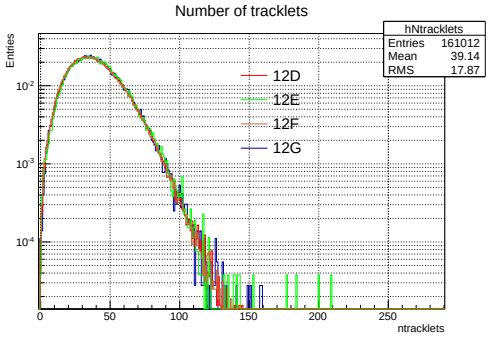

Figure 18: N-tracklets distribution for data period LHC12D/E/F/G with trigger EMCal JET8. The distributions have been normalized with respect to their integral.

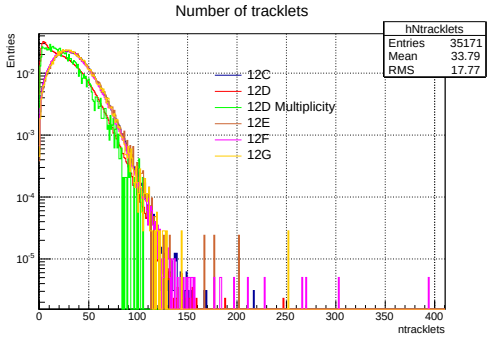

Figure 19: N-tracklets distribution for data period LHC12C/D/E/F/G with trigger EMCal GAMMA7. The distributions have been normalized with respect to their integral.

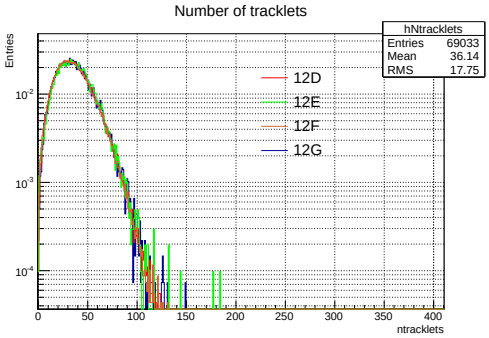

Figure 20: N-tracklets distribution for data period LHC12D/E/F/G with trigger EMCal GAMMA8. The distributions have been normalized with respect to their integral.

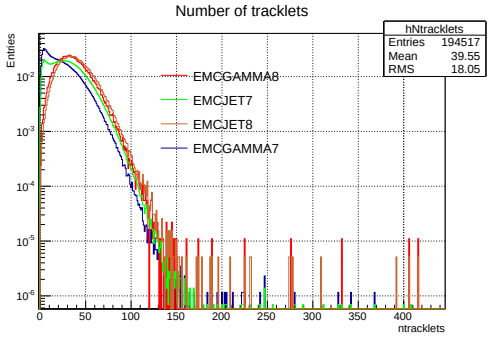

Figure 21: N-tracklets distribution for data period LHC12D with triggers: EMCal JET7, JET8, GAMMA7 and GAMMA8. The distributions have been normalized with respect to their integral.

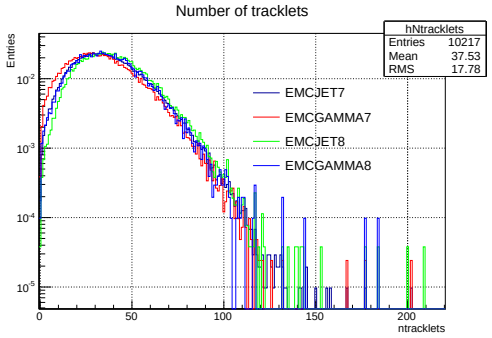

Figure 22: N-tracklets distribution for data period LHC12E with triggers: EMCal JET7, JET8, GAMMA7 and GAMMA8. The distributions have been normalized with respect to their integral.

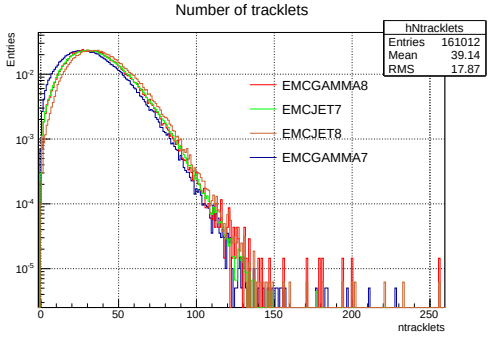

Figure 23: N-tracklets distribution for data period LHC12F with triggers: EMCal JET7, JET8, GAMMA7 and GAMMA8. The distributions have been normalized with respect to their integral.

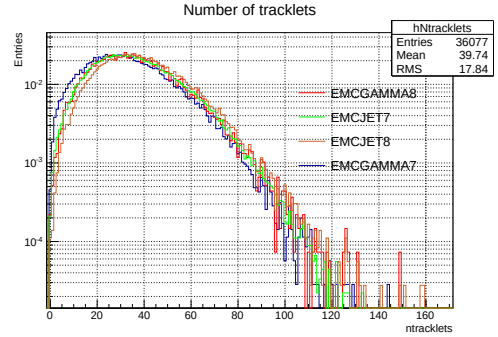

Figure 24: N-tracklets distribution for data period LHC12D with triggers: EMCal JET7, JET8, GAMMA7 and GAMMA8. The distributions have been normalized with respect to their integral.

Figures 17 to 24 show it is necessary to check whether these tracks are also selected for data taking in 12D because there seems to be some strange behaviour that was not seen before in the EMCal7 based sets. Notice that the high multiplicity tail earlier found for period 12F is not found in the tracklets. This suggest that this is a problem in the TPC part of the tracks. There is an agreement with the multiplicity distributions of the tracks with respect to the difference between the 7 and 8 graphs, and there is some difference between the Jet and Gamma as well that was also shown in the multiplicity distributions. The effects vary a bit but can be located inside the ITS as well. Only the strange, nearly minimum bias looking, low N-tracklets region of 12D causes concern, because the bias should move the maximum N-tracklets region up to above 20. While for 12D it can be seen that for the EMCal 7 based trigger the peak is far closer to zero. A main-main collision filling scheme was used for part of period D from which a smaller multiplicity distribution in the 7 trigger with respect to the other periods was seen. If the tracklets multiplicity distribution is compared to multiplicity distribution of the tracks a smaller percentage of pile-up is observed in the tracklets than was observed for the tracks. Thus most of the pile-up is expected to be due to effects in the TPC and not in the ITS.

To see if the effects mentioned on the tracks and tracklets are as strong on the selected tracks as on the overall distribution, those tracks that will be selected for analyses will be discussed[18].

[18]The selected tracks have to be good tracks ($\geq$ 1 SPD cluster, $p_T \geq 0.3$ GeV/c and ITS refit and TPC refit true) as well as have $|z| < 10$ cm, ≥ 70 TPC clusters and $\chi^2/\text{ndf} < 2$ for the TPC as well as $p_T \geq 0.4$ GeV/c and $|\eta| < 0.8$.

4.3.3 Multiplicity of selected tracks

For the selected tracks the differences between the data taking periods and the triggers will again be discussed with respect to the distribution found for the tracks and tracklets. This is done to examine the extent of the influence of the effects found on track/tracklet distribution on the data used for analyses.

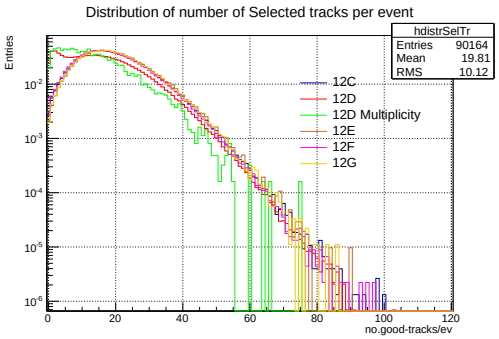

Figure 25: Selected track distribution for data period LHC12C/D/E/F/G with trigger EMCal JET7. The distributions have been normalized with respect to their integral.

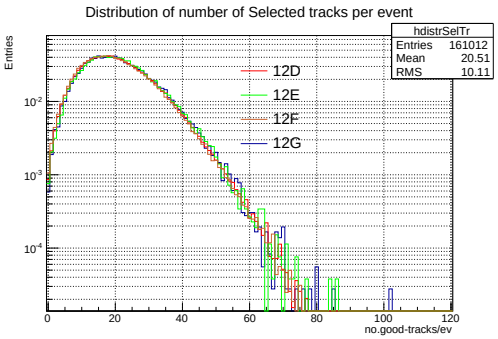

Figure 26: Selected track distribution for data period LHC12D/E/F/G with trigger EMCal JET8. The distributions have been normalized with respect to their integral.

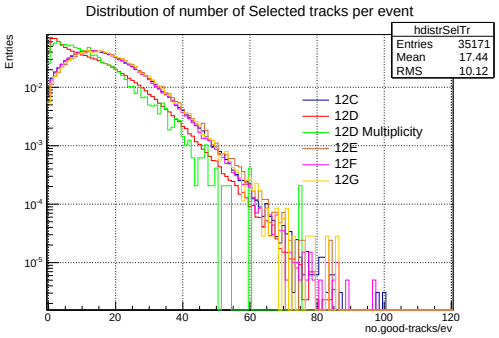

Figure 27: Selected track distribution for data period LHC12C/D/E/F/G with trigger EMCal GAMMA7. The distributions have been normalized with respect to their integral.

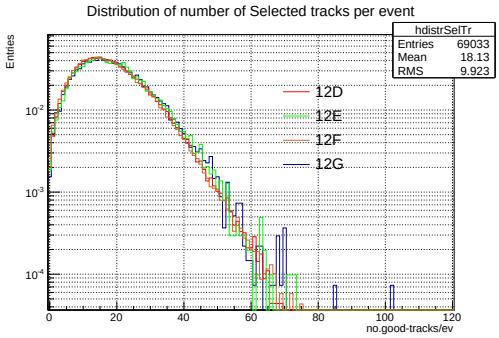

Figure 28: Selected track distribution for data period LHC12D/E/F/G with trigger EMCal GAMMA8. The distributions have been normalized with respect to their integral.

As can be seen in figure 25 the 12D set behaves slightly different. The 12D-multiplicity will be excluded again, however the normal 12D behaves very different. In order to compare the difference between the EMCal 7 based triggers and the EMCal 8 based triggers for period 12D figure 29 is shown.

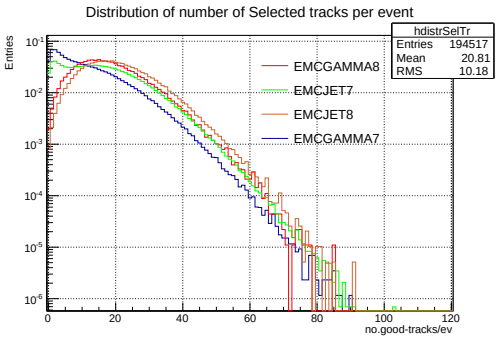

Figure 29: Selected track distribution for data period LHC12D with triggers: EMCal JET7, JET8, GAMMA7 and GAMMA8. The distributions have been normalized with respect to their integral.

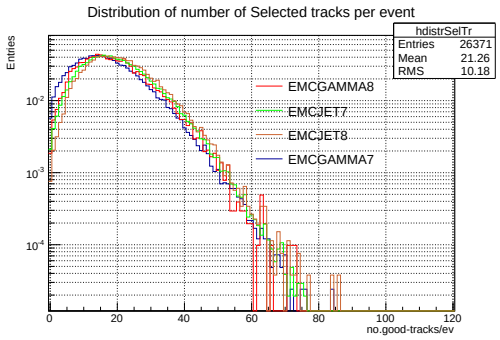

Figure 30: Selected track distribution for data period LHC12E with triggers: EMCal JET7, JET8, GAMMA7 and GAMMA8. The distributions have been normalized with respect to their integral.

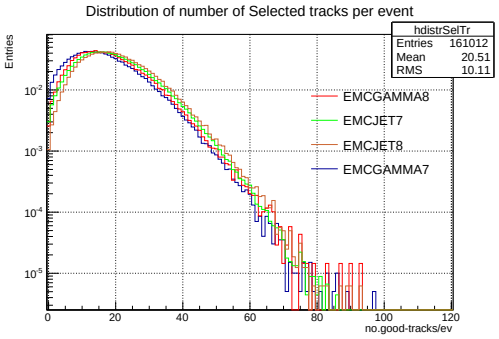

Figure 31: Selected track distribution for data period LHC12F with triggers: EMCal JET7, JET8, GAMMA7 and GAMMA8. The distributions have been normalized with respect to their integral.

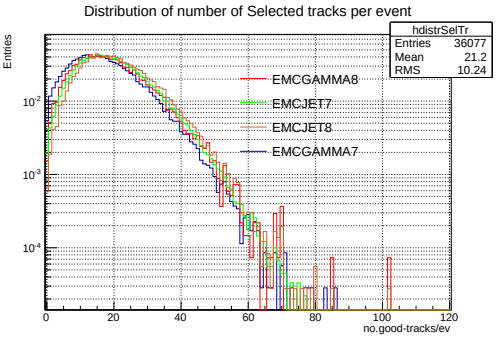

Figure 32: Selected track distribution for data period LHC12G with triggers: EMCal JET7, JET8, GAMMA7 and GAMMA8. The distributions have been normalized with respect to their integral.

These figures show that the difference lies in the EMCal7JET/GAMMA trigger, which behaves differently for period D. This is probably due to the different filling scheme in part of period 12D. As comparison the multiplicity distributions for the other triggers and data taking periods (figures 26 to 28 and 30 to 32) are shown, to conclude that this effect is limited, with respect to those triggers mentioned, to the EMCal JET 7 and EMCal GAMMA 7 trigger in period 12D. Thus only the V0 trigger seems to be influenced by this different filling scheme.

4.3.4 Transverse momentum distribution of good tracks

The difference between the trigger for period 12D is also visible in the ratio of the p_T distribution of good tracks, which shows a preference for low p_T particles with respect to the p_T distribution of the other data sets. This difference is most extreme in the EMCal7 triggers mentioned, but is also visible, more subtle, in the EMCal8 data set (figure 33).

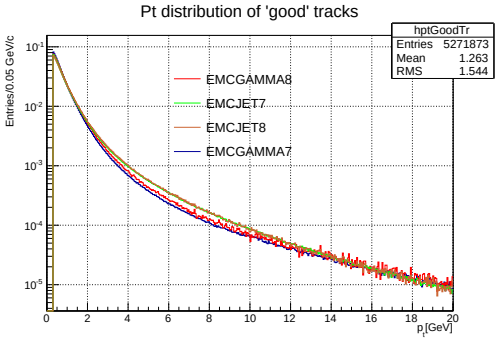

Figure 33: p_T distribution of good tracks for data period LHC12D with triggers: EMCal JET7, JET8, GAMMA7 and GAMMA8. The distributions have been normalized with respect to their integral.

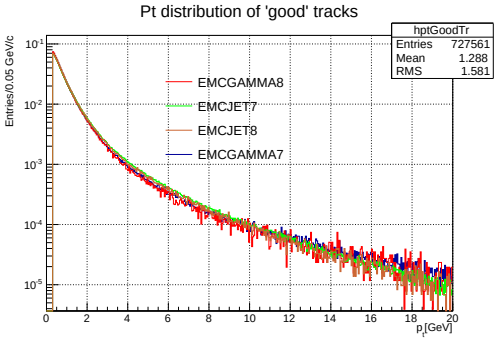

Figure 34: p_T distribution of good tracks for data period LHC12E with triggers: EMCal JET7, JET8, GAMMA7 and GAMMA8. The distributions have been normalized with respect to their integral.

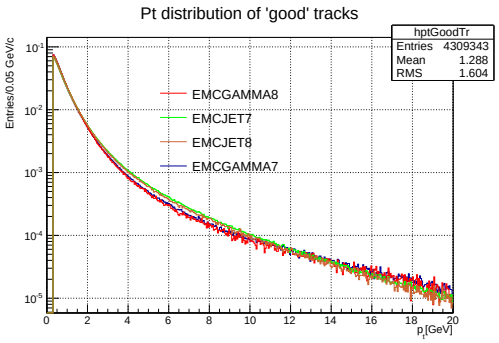

Figure 35: p_T distribution of good tracks for data period LHC12F with triggers: EMCal JET7, JET8, GAMMA7 and GAMMA8. The distributions have been normalized with respect to their integral.

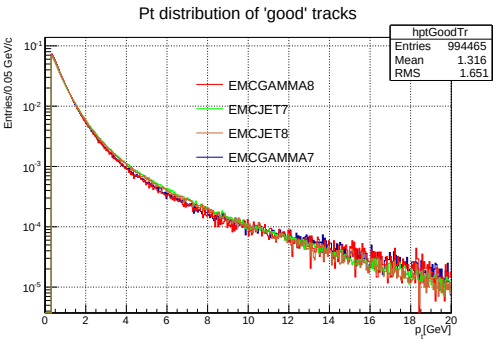

Figure 36: p_T distribution of good tracks for data period LHC12G with triggers: EMCal JET7, JET8, GAMMA7 and GAMMA8. The distributions have been normalized with respect to their integral.

From these figures a difference between the gamma and jet triggers is seen, but this is to be expected as the triggers are slightly different in range and threshold. As it is difficult to see if this difference is stronger in period 12D than in for instance in period 12F, the different trigger are also shown with respect to all periods. Figure 37 to 40 show that indeed the difference is bigger in the the GAMMA7 and JET7 than in the other periods.

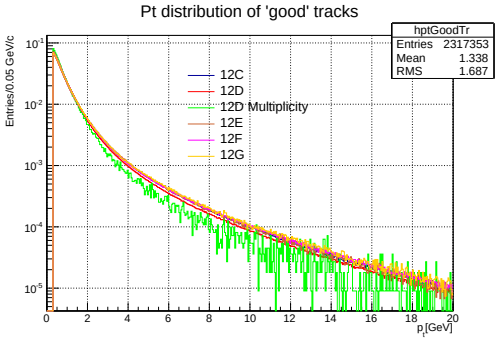

Figure 37: p_T distribution of good tracks for data periods LHC12C/D/E/F/G with trigger EMCal JET7. The distributions have been normalized with respect to their integral.

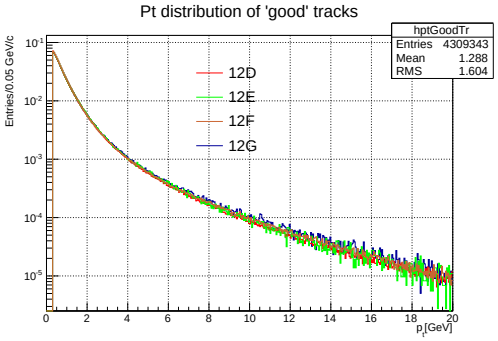

Figure 38: p_T distribution of good tracks for data periods LHC12D/E/F/G with trigger EMCal JET8. The distributions have been normalized with respect to their integral.

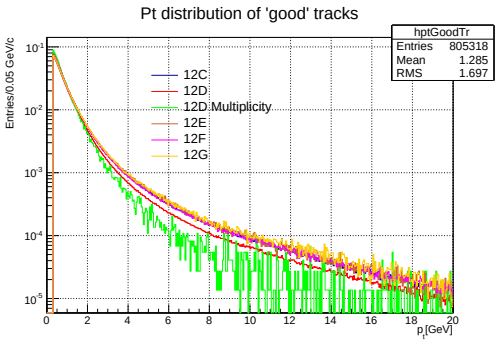

Figure 39: p_T distribution of good tracks for data periods LHC12C/D/E/F/G with trigger EMCal GAMMA7. The distributions have been normalized with respect to their integral.

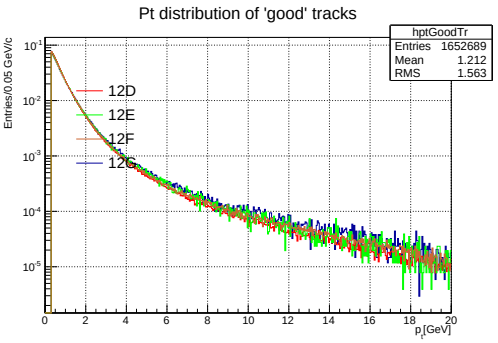

Figure 40: p_T distribution of good tracks for data periods LHC12D/E/F/G with trigger EMCal GAMMA8. The distributions have been normalized with respect to their integral.

In order to exclude overlap as the reason for these differences, the overlap between triggers in different data periods was studied.

4.3.5 Trigger selection fraction.

In order to see the extent of the overlap of the triggers an EMCEJE7 (EMCal JET 7) trigger was used and shown is how much of all triggers was selected. This shows that there is a rather large overlap between the triggers. This implies that given an EMCal Jet 7 trigger is selected, a certain percentage of the total amount available for the other triggers is also selected. This would be expected for the EMCal gamma trigger, as was already mentioned in the explanation of the triggers.

The overlap in the selection seen in figures 41 and 42 is due to the threshold of multiple triggers being met and is not considered problematic. It cannot be the reason that data period 12D is behaving different with respect to other data periods. The only differences that can be found is that in period 12C the EMCEJE 7 trigger is used also in combination with the the normal EMCal triggers, in later periods the data taking periods have been separated. However data period 12D is similar to periods for 12E/F/G. The overlap should be kept in mind if multiple triggers are to be combined.

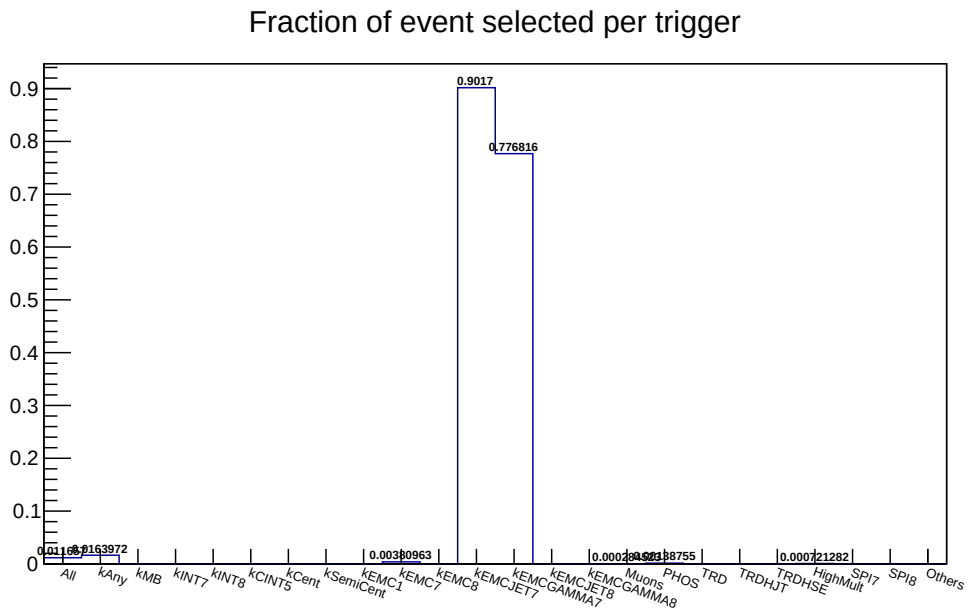

Figure 41: Multiplicity fraction with respect to all triggers fired versus trigger type for data period LHC12C after selecting trigger EMCal JET 7 and using physics selection criteria.

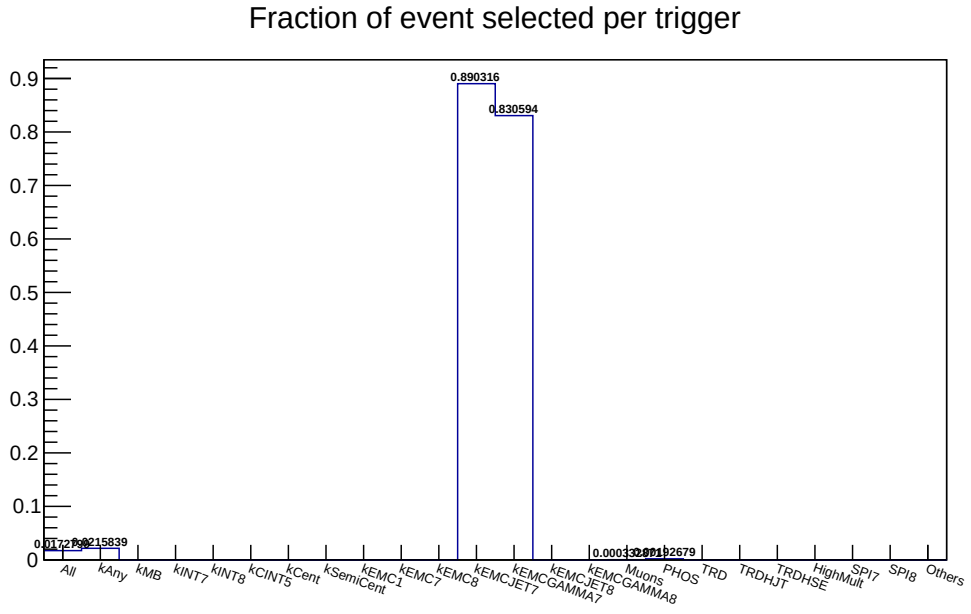

Figure 42: Multiplicity fraction with respect to all triggers fired versus trigger type for data period LHC12D after selecting trigger EMCal JET 7 and using physics selection criteria.

4.4 Primary vertex position and ITS tracking quality

4.4.1 Primary vertex position of selected events

For the selection of physics events used for D-meson reconstructions, one of the criteria is that the reconstructed primary vertex lays within 10 cm of the centre of the ITS. In this section the distribution of the primary vertex within the selected events will be shown. This is done to check that this selection criteria is indeed met by those particles passing this check. The shape of the distribution is studied to look for a possible difference between the data sets.

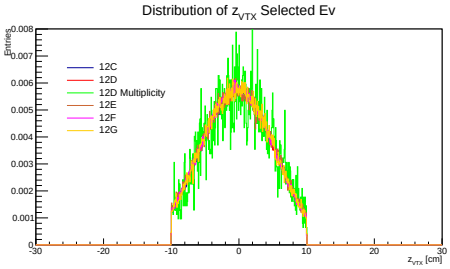

Figure 43: Data periods 12C/D/E/F/G trigger EMCal JET7, Z-vertex distribution of the selected events. These distributions have been normalized with respect to their integral.

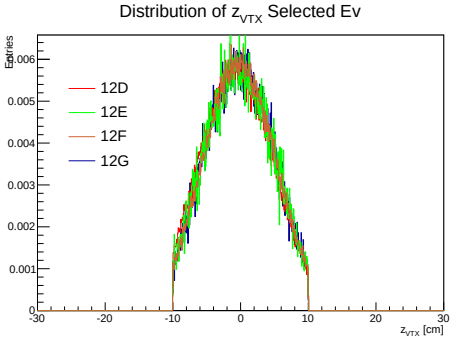

Figure 44: Data periods 12D/E/F/G trigger EMCal JET8, Z-vertex distribution of the selected events. These distributions have been normalized with respect to their integral.

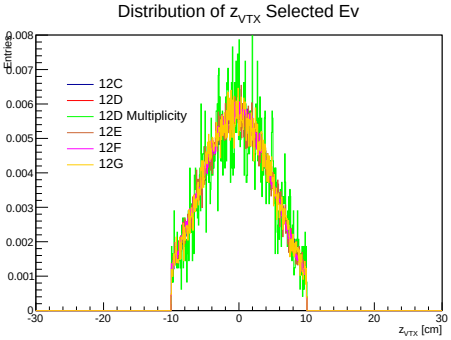

Figure 45: Data periods 12C/D/E/F/G trigger EMCal GAMMA7, Z-vertex distribution of the selected events. These distributions have been normalized with respect to their integral.

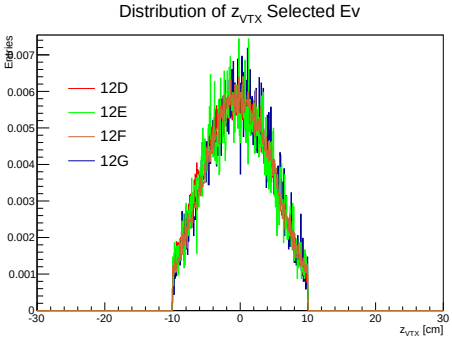

Figure 46: Data periods 12D/E/F/G trigger EMCal GAMMA8, Z-vertex distribution of the selected events. These distributions have been normalized with respect to their integral.

Figures 43 to 46 indicate that there is no significant difference between the periods with respect to the Z-vertex and the selection criteria with respect to the position of the vertex have been met[19].

[19] Maximally 10 cm from the centre to either side is allowed inside this criteria

4.4.2 ITS tracking quality

The distribution of the tracks with a point in a specific layer will be checked. If there was a problem with the ITS, due to overheating or other issues, that layer would be expected to have a lower amount of tracks than usual.

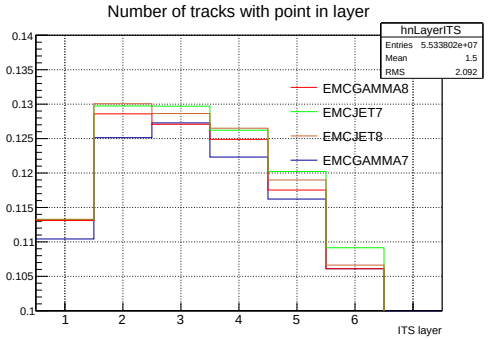

Figure 47: Amount of tracks with a point in a certain layer in data period LHC12D, normalized with respect to the total amount of tracks.

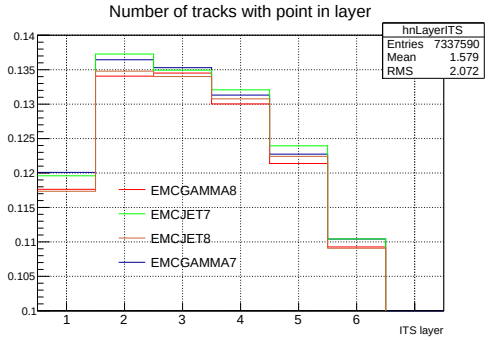

Figure 48: Amount of tracks with a point in a certain layer in data period LHC12E, normalized with respect to the total amount of tracks.

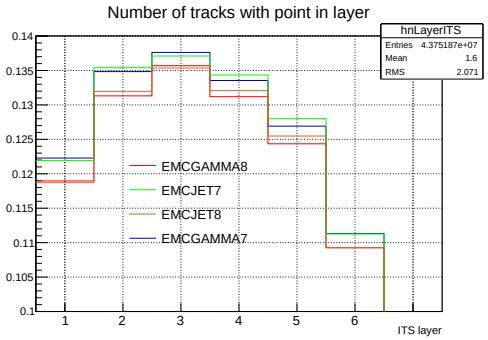

Figure 49: Amount of tracks with a point in a certain layer in data period LHC12F, normalized with respect to the total amount of tracks.

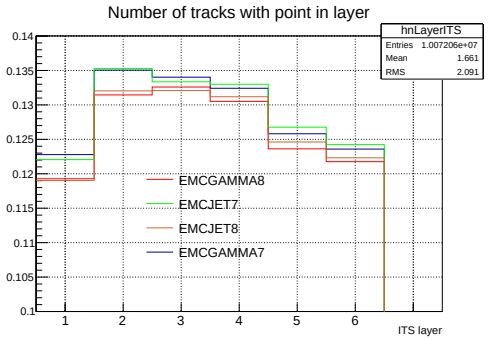

Figure 50: Amount of tracks with a point in a certain layer in data period LHC12G, normalized with respect to the total amount of tracks.

In 2008 there used to be some problems with the ITS, mainly due to the overheating of certain parts of the SPD. During the 2012 data period certain parts of the SPD were brought back to life as the cooling of these parts was improved, this explain the slight improvements that is seen in the number of tracks with point in layer. These points are normalized with respect to the tracks found. The rough shape is within expectations.

4.5 Impact parameters distributions of D-meson decay.

The selection of the trigger is in itself a very important selection criterion. For the selection of the daughter particles of the D0 a basic topological selection was added. This can be found in the file: **PWGHF/vertexingHF/macros/makeTFile4cutsD0toKpi** as the basic *pp* cuts.

As mentioned in this section the behaviour of the impact parameters will be studied. A bump in the distribution of the impact parameter r_ϕ and z with respect to the daughter particles has been found, and is found to be in the same data sets that have strange multiplicity distributions.

The EMCalJET7 triggered data is used to show the difference between the periods, there was no significant difference between the triggers.

Comparing figures 51, 52 with the multiplicity figure 5 shown earlier, indicates that the strange data periods overlap. However the reason for them to coincide has not been identified.

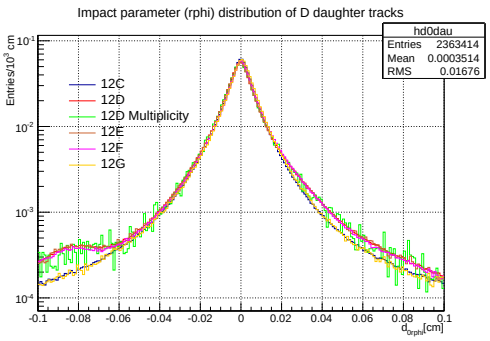

Figure 51: Impact parameter $d_{0,r\phi}$ of D-daughters distribution, normalized on its integral.

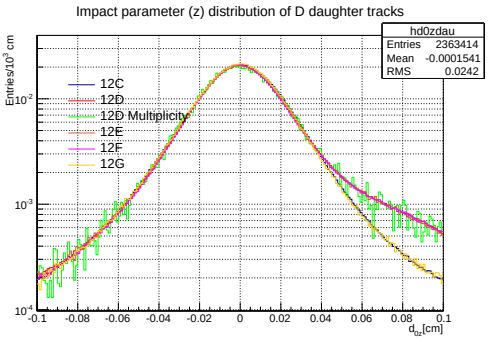

Figure 52: Impact parameter $d_{0,z}$ of D-daughters distribution, normalized on its integral.

As has been shown in the previous section there is no a priori reason to expect this to be connected to the parts of the SPD that were brought back to life. However a χ^2 check[20] mentioned some misalignment in the SPD around an angle of $\phi = 6$ radians. In response to those results the bumps in the impact parameters were studied with respect to the ϕ-angle of the prompt particle.

[20] Done by Chiara Bianchin (Utrecht University), Marta Verweij (Wayne State University) and Ruben Shahoyan (CERN).

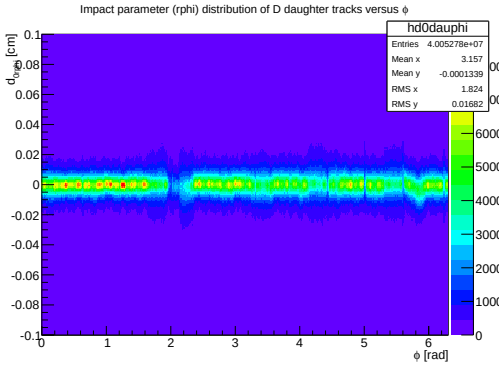

Figure 53: Data period 12A trigger INT7, Impact parameter $d_{0,r\phi}$ versus ϕ.

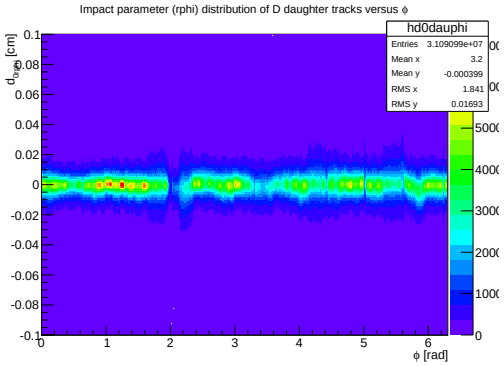

Figure 54: Data period 12B trigger INT7, Impact parameter $d_{0,r\phi}$ versus ϕ.

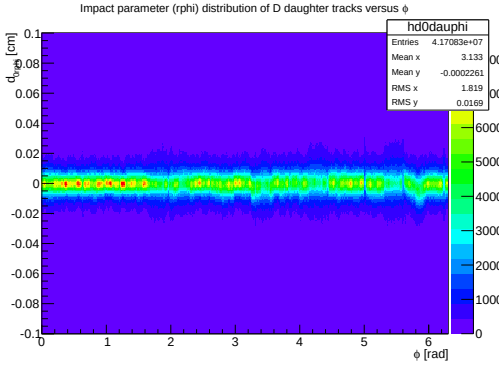

Figure 55: Data period 12C trigger INT7, Impact parameter $d_{0,r\phi}$ versus ϕ.

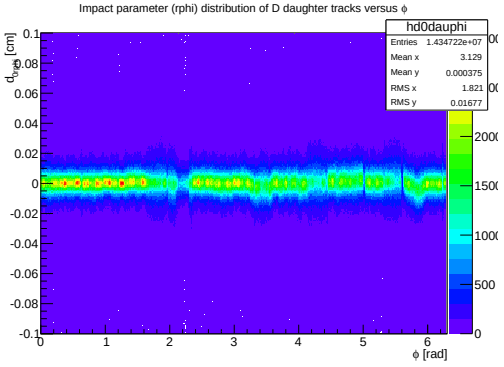

Figure 56: Data period 12G trigger INT7, Impact parameter $d_{0,r\phi}$ versus ϕ.

As can be seen in figures 53, 54, 55 and 56 the alignment was not perfect in these periods, though there is no bump in the impact parameter distribution for these periods. There still is a small shift visible around 5.8 radian in ϕ.

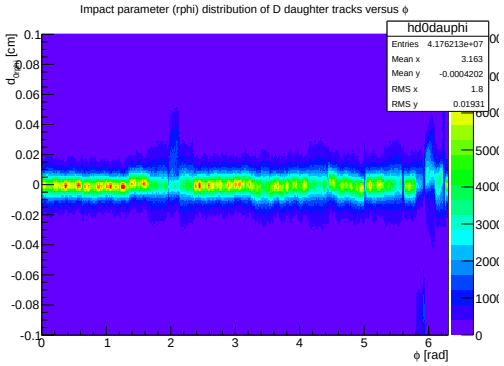

Figure 57: Data period 12D trigger INT7, Impact parameter $d_{0,r\phi}$ versus ϕ.

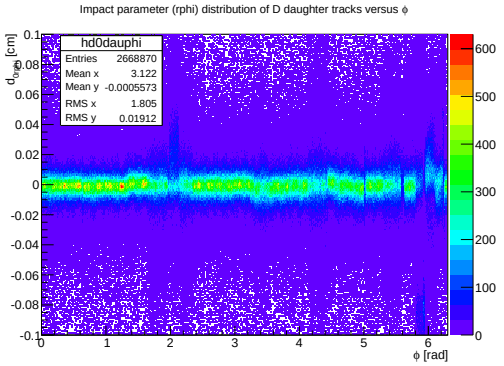

Figure 58: Data period 12E trigger INT7, Impact parameter $d_{0,r\phi}$ versus ϕ.

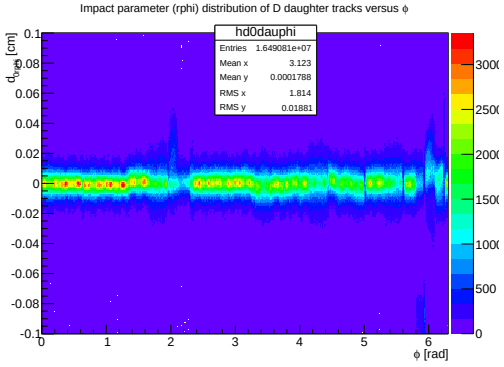

Figure 59: Data period 12F trigger INT7, Impact parameter $d_{0,r\phi}$ versus ϕ.

In the periods containing the bump a strong displacement is seen close to $\phi = 5.8$ rad. This displacement is stronger in figures 57, 58 and 59 than in the periods not containing the bump in distribution. Note that there seem to be to less statistics in all periods for prompt tracks with an angle close to $\phi = 2$ rad. A possible explanation for this could be that this is an area with more dead SPDs.
The first hypothesis drawn from these figures was that the displacement at $\phi = 5.8$ rad could be the reason for the problems with both the impact parameters. In order to falsify this the same check was done for the $d_{0,z}$ impact parameter.

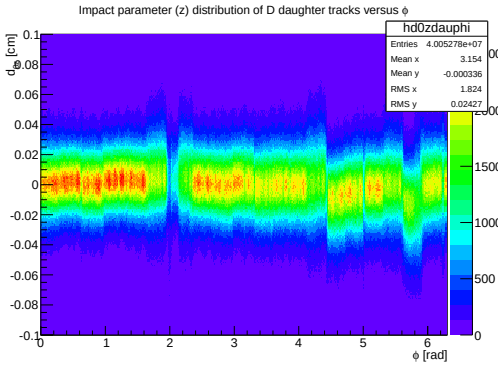

Figure 60: Data period 12A trigger INT7, Impact parameter $d_{0,z}$ versus ϕ.

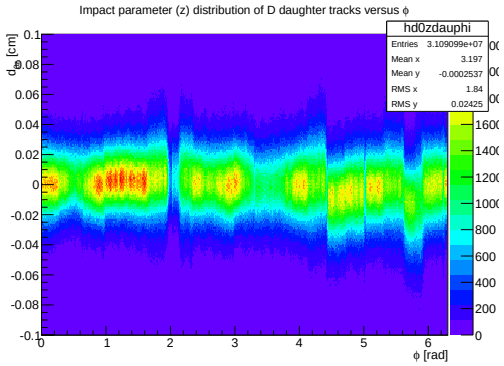

Figure 61: Data period 12B trigger INT7, Impact parameter $d_{0,z}$ versus ϕ.

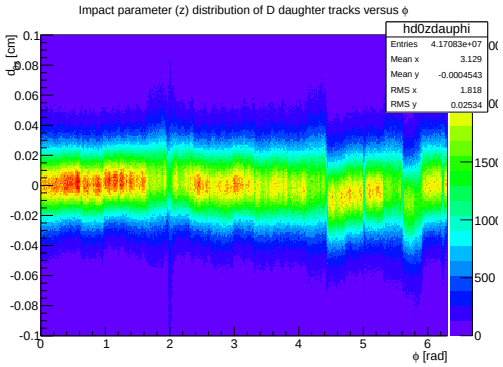

Figure 62: Data period 12C trigger INT7, Impact parameter $d_{0,z}$ versus ϕ.

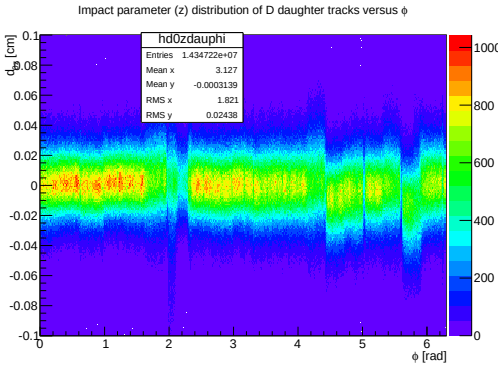

Figure 63: Data period 12G trigger INT7, Impact parameter $d_{0,z}$ versus ϕ.

The d_0 resolution is poorer in the z direction than in the r, ϕ direction, as can be seen by comparing figures 60 till 63 with those for the other impact parameter. Due to this the distribution seems a little less continuous and the distribution is wider. A careful examination of the point of the dip for the impact parameter on $r\phi$,($\phi \approx 5.8$ rad) notes there is a small dip visible in these figures as well.

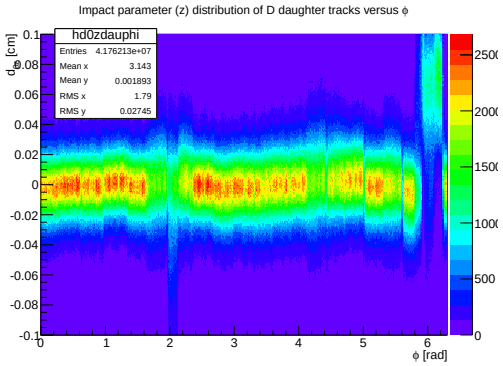

Figure 64: Data period 12D trigger INT7, Impact parameter $d_{0,z}$ versus ϕ.

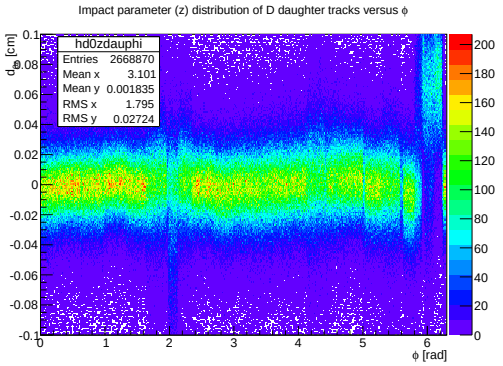

Figure 65: Data period 12E trigger INT7, Impact parameter $d_{0,z}$ versus ϕ.

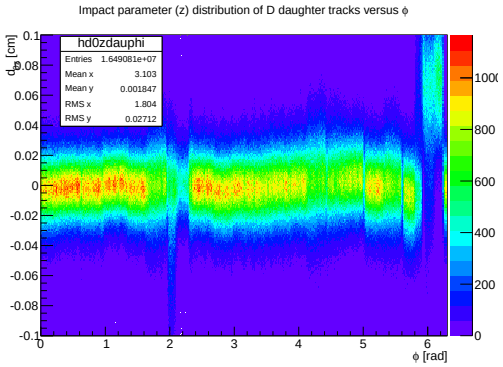

Figure 66: Data period 12F trigger INT7, Impact parameter $d_{0,z}$ versus ϕ.

The bump in the $d_{0,z}$ distribution does not originate from $\phi = 5.8$ rad exactly but seems to be originating from approximately 5.9 till 6.25 rad as can be seen in figures 64, 65 and 63. This means that there is also the influence of the wrong geometry in the reconstruction on the tracks coming from this section.
There are misalignments that should be fixed by the experts. This was requested to be done in a new reconstruction with for all 2012 pp datasets. As a temporary fix all the data coming from these angles will be disregarded.
One of the final parts of the quality assurance will test the particle identification, as this mechanism will be responsible for filtering out a large amount of background in later analyses.

4.6 Particle Identification detectors

The trigger should not influence the Particle Identification. As indeed the performance is mainly independent on the trigger, the focus is on the trigger with larger statistics. Both the TOF and the TPC distribution will be used. For clarity only a small set of the available figures is shown.

4.6.1 TOF

The first results for the TOF were swiftly checked for the INT7 trigger by the author[21] during her summer student project. The errors were considered relatively small with respect to that of the TPC, and thus of later concern. In later discussion of the TOF figures the problems were discussed: for ABCD there is a shifted band visible crossing the kaons towards the protons and below 0.6 GeV/c, the n sigma is shifted up for the proton (and kaons for period CD). For period EFG there seems to be a band between the pion and the kaon, as well as the shift in the n sigma for the protons and kaons still being there. A distribution at very large time differences for period D and G and possibly E is also seen[22]. These effects can only be seen in distributions with high statistics, such as the pure EMC7 and INT7 triggered distribution. Therefore figures for the INT7 trigger are shown[23].
The TOF particle identifications works by taking the time-zero of the T0 or of the TOF itself depending on availability, and calculating the time the particles need to reach the TOF. These times are then compared with the expected time for each species, which would ideally give a Gaussian around the specific time of a type of particles for a certain momentum.
Figures 67-70 show the difference between the time hypothesis for a specific type of particle and the measured time as a function of the momentum for different periods. Figures 71-74 (75-78) show the corresponding number of sigmas for the kaon (proton) hypothesis, equivalent to the time difference normalized by the time resolution vs momentum. The black markers indicate the fitted means for each momentum slice and the red markers indicate the fitted pulls for each momentum slice. Overall the mean is expected to be around 0 and the pull is expected to be around one due to the normalization. Note that for low momentum there is a range were the TOF does not function (optimally), as the Gaussian around the particle specific time overlap for low momenta it cannot distinguish between them at those momenta, as has been mentioned in section 3.2.5.

The distributions from period 12C and 12D feature a band crossing the kaons, and figures 12F and 12G show a band between the pions and the kaons. These sets are chosen for there relatively large statistics and in order to demonstrate the issues clearly.

[21] under supervision of Chiara Bianchin
[22] These results are taken from the internal research note of Chiara Bianchin
[23] In appendix A the figures containing the EMCal JET7 trigger for which the author did the checks are shown.

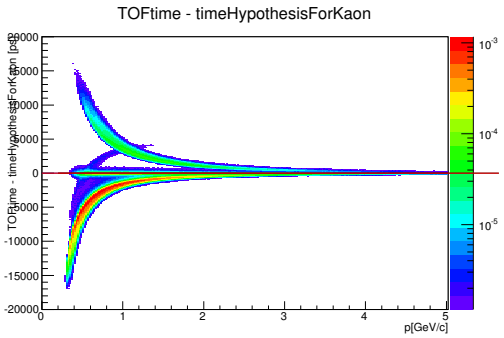

Figure 67: Time of Flight measured-time hypothesis for the kaon versus momentum in LHC12C, triggered with INT7 minimum bias.

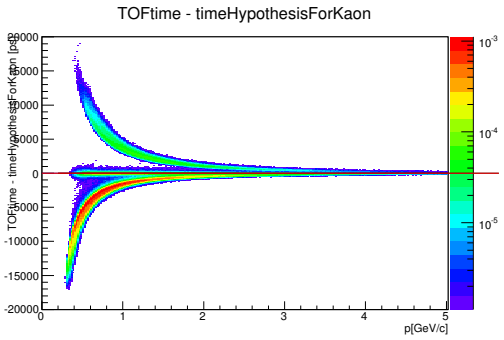

Figure 68: Time of Flight measured-time hypothesis for the kaon versus momentum in LHC12F, triggered with INT7 minimum bias.

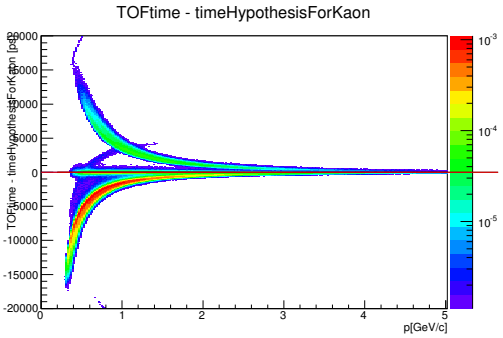

Figure 69: Time of Flight measured-time hypothesis for the kaon versus momentum in LHC12D, triggered with INT7 minimum bias.

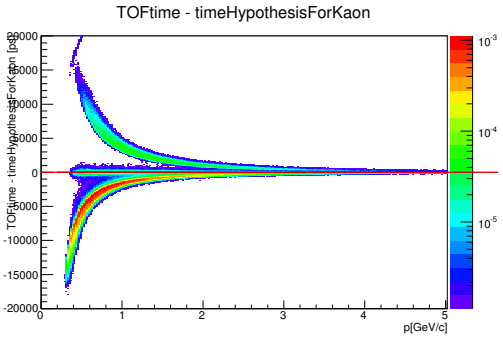

Figure 70: Time of Flight measured-time hypothesis for the kaon versus momentum in LHC12G, triggered with INT7 minimum bias.

In figures 67 and 69 a crossing band for the kaons in the direction of the protons is visible. This could be due to a problem in the calibration. An extra distribution sitting at large time differences for figures 69 and 70 is also noted. Figure 68 does not a priori point out a problem with period 12F. In order to examine the effects of the crossing band on the kaons the n sigma versus p distribution is discussed next.

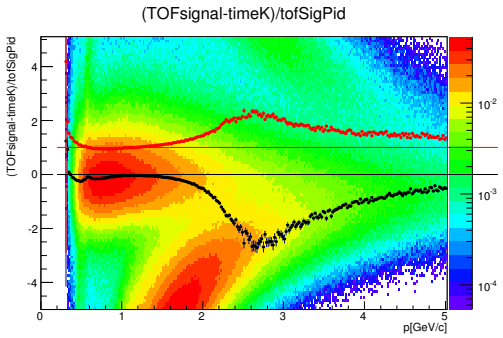

Figure 71: Time of Flight measured-time hypothesis for the kaon versus momentum in LHC12C normalized by sigma, triggered with INT7 minimum bias.

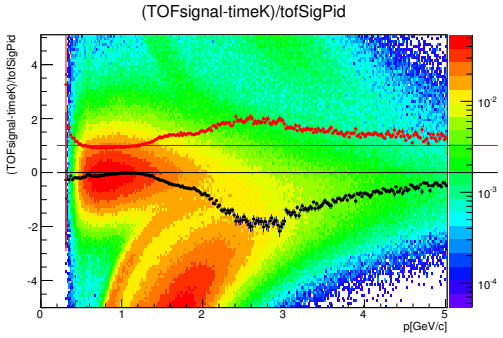

Figure 72: Time of Flight measured-time hypothesis for the kaon versus momentum in LHC12F normalized by sigma, triggered with INT7 minimum bias.

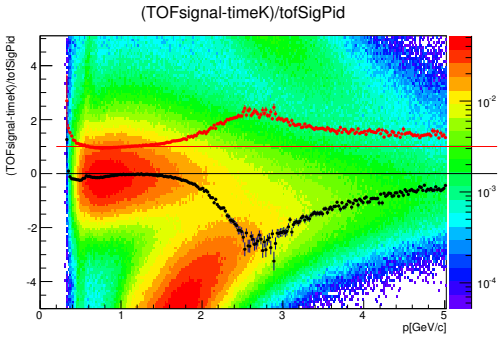

Figure 73: Time of Flight measured-time hypothesis for the kaon versus momentum in LHC12D normalized by sigma, triggered with INT7 minimum bias.

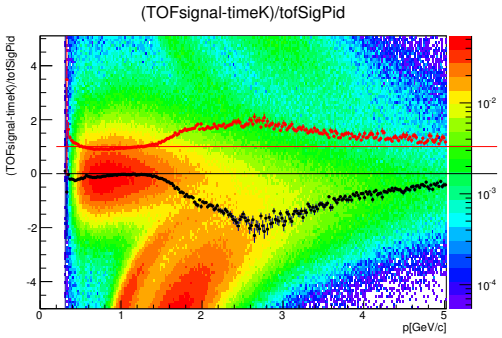

Figure 74: Time of Flight measured-time hypothesis for the kaon versus momentum in LHC12G normalized by sigma, triggered with INT7 minimum bias.

The crossing band shown earlier is visibly figures 71 and 73 as a small green band crossing between 0.4 and 0.6 GeV/c. In figures 72 and 74 there is a clear band visible between the kaons and the protons. These bands are due to a time shift in some of the crates of the TOF. All figures show that the n sigma is slightly shifted up for low momenta. Finally the distributions for the protons versus momentum normalized by the sigma is shown, to demonstrate the problems found for low momenta.

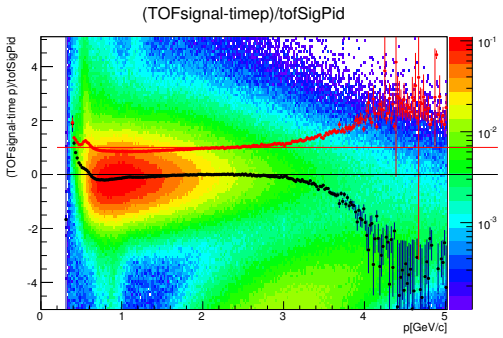

Figure 75: Time of Flight measured-time hypothesis for the proton versus momentum in LHC12C normalized by sigma, triggered with INT7 minimum bias.

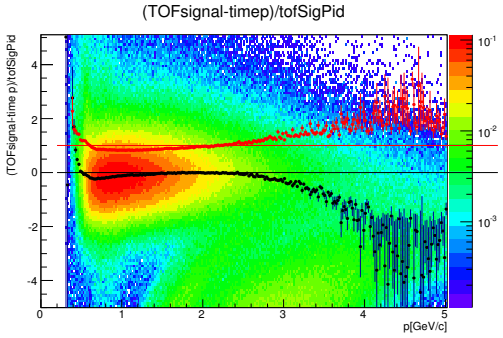

Figure 76: Time of Flight measured-time hypothesis for the proton versus momentum in LHC12F normalized by sigma, triggered with INT7 minimum bias.

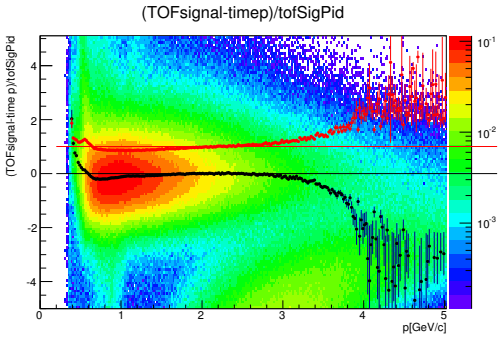

Figure 77: Time of Flight measured-time hypothesis for the proton versus momentum in LHC12D normalized by sigma, triggered with INT7 minimum bias.

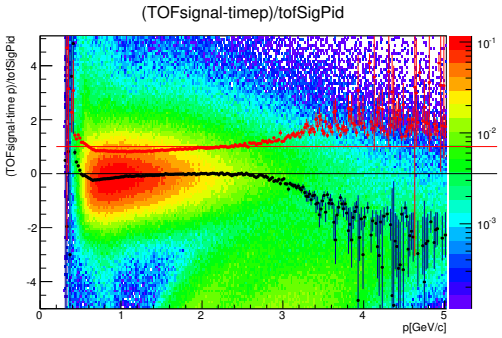

Figure 78: Time of Flight measured-time hypothesis for the proton versus momentum in LHC12G normalized by sigma, triggered with INT7 minimum bias.

Figures 75, 76, 77 and 78 show that the n-sigma distribution is shifted up below 0.6 GeV/c. There are some indications of the band that was crossing the kaons towards the protons in figures 75 and 77. Overall the problems are relatively small and can be fixed by some re-calibration of the data. The the TOF results will be generally accepted for the current results.

4.6.2 TPC

First the specific ionization energy loss dE/dx versus the transverse momentum of the particles will be discussed in order to check the validity of the TPC data.

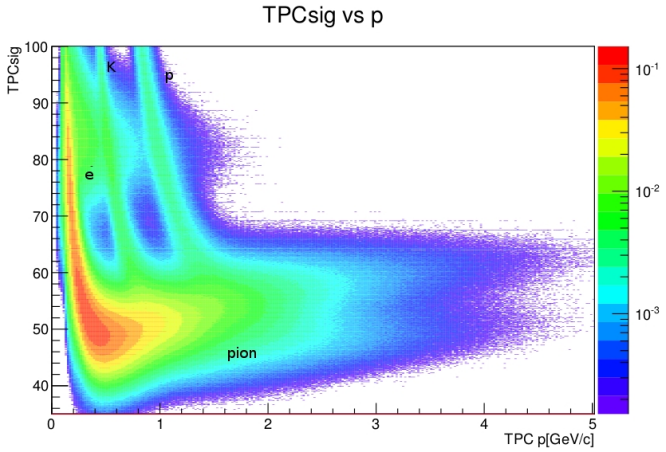

Figure 79: Specific ionization energy loss dE/dx versus partial momentum in data period LHC12F, trigger kINT7.

Besides these overviews a zoom is made around the proper energy loss of a certain type of particle. For each momentum slice the mean and the pull are extracted and shown through markers inside the figure. The pull should be approximately 1, while the mean should be close to 0, due to normalisation and the comparison to the expected energy loss for this specific particle. As can be seen in figure 79 the electron line overlaps and the kaon and proton lines get quite close to the pion for higher momenta. The pion one, thus will influence the other two particles strongly, as pions are the most common detected particles. The other two particles are so much less common detected and will only slightly influence the pion lines.
The INT7 results are used such that it is comparable to the first check of the splines[24], which was also done using the INT7 trigger, in order to detect possible improvements of the results. In order to increase the legibility of this thesis only proton n sigma vs p distributions for 12D/E/F/G are shown. The figures for the pion and kaons as well as periods 12A/B/C are mentioned in Appendix B.

[24]The splines are a way of normalizing the TPC results with respect to the specific running conditions. As an example: the results depends among others on the voltage on the cathode.

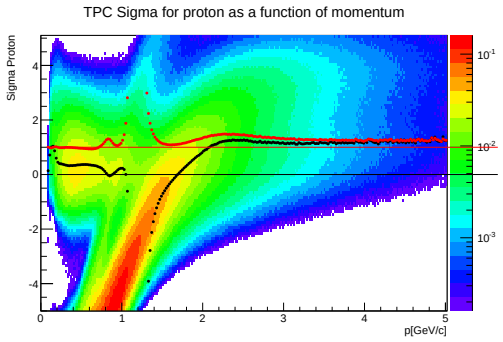

Figure 80: TPC Sigma Proton versus momentum, in data period 12D with trigger INT7.

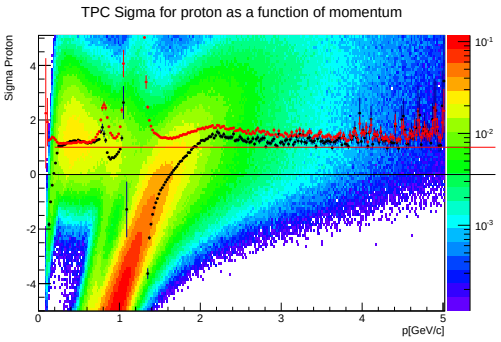

Figure 81: TPC Sigma Proton versus momentum, in data period 12E with trigger INT7.

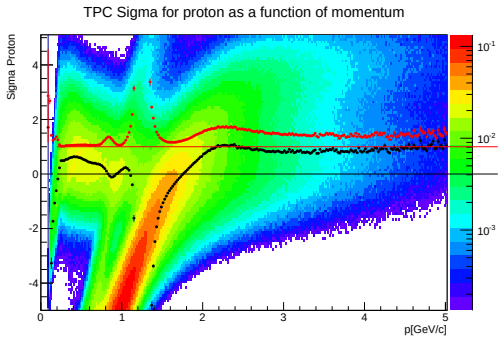

Figure 82: TPC Sigma Proton versus momentum, in data period 12F with trigger INT7.

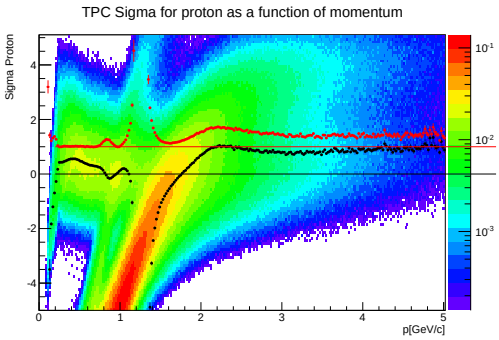

Figure 83: TPC Sigma Proton versus momentum, in data period 12G with trigger INT7.

Figures 81 and 83 indicate a large discontinuity in the mean and pull between approximately 1.1 and 1.5 GeV/c. This is mostly due to the pions, with a minor contribution of the kaons. However for period 12E the effect that it does not work properly for the p_T below 1 GeV/c as well as the difference in shapes between figures 81 and 83 are due to problems in the splines. No improvements will be made for period 12E as it contains very little statistics and combined with the fact that the parametrization is hard because the voltage of the TPC has been unstable in this period, has lead to the exclusion of this period for final results. For the other data periods studied the corrections have been found to be reasonable.
The effects of the improvement of the TPC PID performance can be seen in figure 84, where the signal extraction with the old and new parametrization both divided by the total signal without the use of PID for the D^{*+} are shown. The signal extracted should be approximately 5 percent lower for a signal with PID versus that of a signal without PID[25], as the PID strategy used is aimed to be fully efficient. This hints that the new splines have improved the TPC PID performance.

[25]The cuts allows particles to be used as a certain type if they are within 3σ's of that types mean.

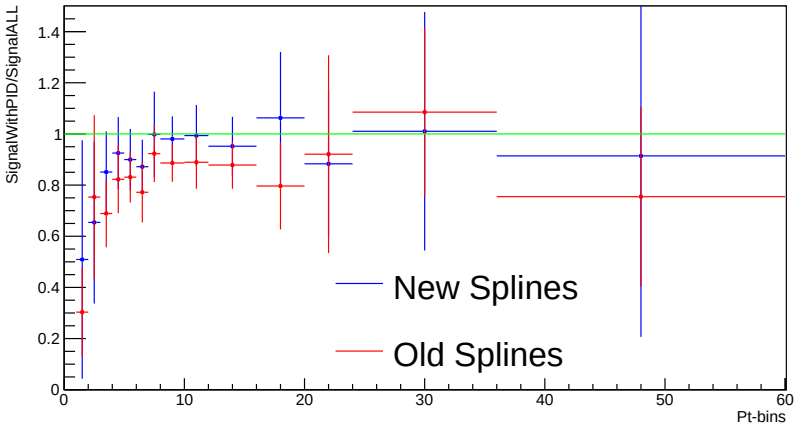

Figure 84: Ratio between the Signal with PID and the Signal without taking into account PID versus momentum calculated on the D^{*+} spectrum, taking into account dataset 12A/B/C/D/E/F/G.

4.7 Pile-up rejection via multi-vertexing method

A different attempt to reject pile-up events is studied on all periods, the results are similar to 12G which is shown here. This has been reviewed for the INT7 and the INT8 trigger, in which the latter is less effected by pile-up. Which are compared to the INT7 triggers with normal pile-up settings, to see if this pile-up rejection will influence the multiplicity distribution of the tracks/tracklets.

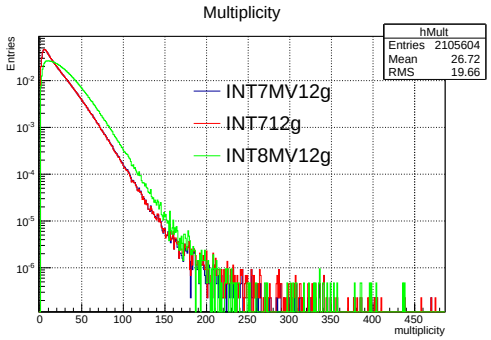

Figure 85: Multiplicity INT7MV,INT7 and INT8MV in period 12G normalized with respect to their integral.

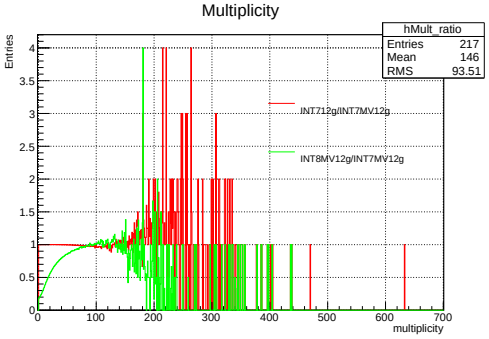

Figure 86: Multiplicity ratio of INT7MV (multivertexing corrected) over INT7 normal and INT8MV/INT7 in period 12G.

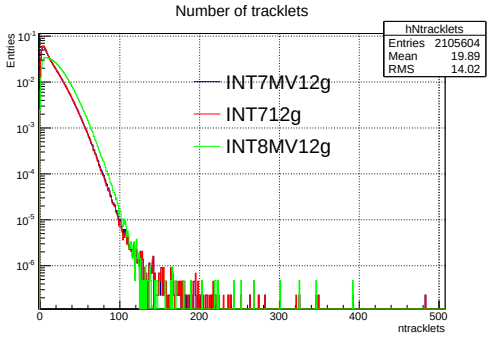

Figure 87: Number of N-tracklets of INT7MV, INT7 and INT8MV in period 12G, normalized with respect to their integral.

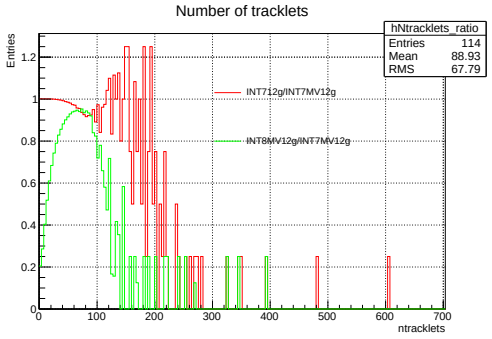

Figure 88: Number of N-tracklets ratio of INT7MV (multivertexing corrected) over INT7 normal and INT8MV/INT7 in period 12G.

Figures 86, 85, 88 and 87 indicate that the Multivertexing[26] does indeed influence the results, but it seems that it influence the N-tracklets at high multiplicity with only approximately 10%. As the tail/bump in period F is not cancelled out by this pile-up rejection, this indicates that the tail/bump is not due to pile-up formed purely through multiple vertices. Other attempt on new pile-up rejection have been found to be even less effective, concluding that the often used pile-up rejection does not successfully reject this high multiplicity effect.

[26] A cut that will take out events that contain multiple vertexes that seem primary, as they come from pile-up event combined with a main event.

4.8 Conclusions and Outlook of the quality assurance

From the checks made we conclude that there is a difference between the data taking periods that should be sorted out. There are different amounts of overlap between the triggers in different periods and the multiplicity distributions of tracks and tracklets as well as the impact parameters behave differently.
However discomforting these conclusions might be, as was seen from other tests done on this set, a reasonable signal can still be found for the different D mesons. Moreover the '12D-Multiplicity' set should be excluded from the physics data period. While the other data sets should eventually yield reasonable results.
The PID on the reconstruction data will be used, as the Particle Identification is found to be nearly reasonable for the TOF for all sets and for the TPC for all sets minus 12E. The problems with the latter will not influence our results strongly as this is a data set with low statistics.
As the EMCal trigger was not constant in period 12A and 12B, these periods will be excluded for the extraction of the yield.
The high multiplicity effects could possibly be due to non-effective pile up rejection. However, if this would be the problem then different types of pile-up rejection, for instance one based on multi-vertex recalibration, could have been a remedy. This is not the case as the effect of a multi vertexing pile-up correction only cancels out approximately 10% of the high-multiplicity tail, which is not sufficient to eliminate the problem.
Finally the misalignments in the ITS will influence all measurements, because it means that some track have been reconstructed with the wrong geometry. For this reason the decision was made to reconstruct the entire data set, to correct these misalignments and also improve some other problems. After the new reconstruction the multiplicity and tracklet distribution should be studied again.

Thus any results given for the $\sqrt{s} = 8$ TeV data sets with respect to D meson reconstructions will be improved in the future. For this thesis the choice has been made to, due to time constraints, do the analysis with the flawed data set. While the new reconstruction is not yet completed for the extraction of the yield a temporary patch was issued eliminating candidates with tracks with ϕ angles in the 5.6 to 2π region.
The errors on the raw yield will still be increased with respect to the correct reconstruction, but reasonable cuts can extracted as well as an estimate of the results possible with the new reconstruction. The misalignments will influence the impact parameter resolution for the selection of the D^{*+}. However as the problems are local, a cut optimization run on the current reconstruction can be used for the new reconstruction. The results of the corrected data will thus be processed faster as the optimization step can be skipped and the yield extraction can be run on the new reconstruction without further work.

5 D^{*+} reconstruction

5.1 Data sample

For this second part a few technical notes will be made. The run-numbers that are used within a certain period have been mentioned in table 1 in section 4.1 . Unless mentioned the trigger was set to be EMCal7. For the optimization on data periods LHC12A to LHC12G were used, and the problems found in the quality assurance are not taken into account.
For the final invariant mass distributions periods LHC12C/D/E/F/G were used, and the tracks from $5.6 < \phi \leq 2\pi$ were rejected via **fApplySPDMisalignedPP2012** of the RDHF-cuts.
The set of cuts that was used can be found in Appendix C, taking into account that the the pile-up rejection was turned on.
The filtering cuts are the standard for the pp dataset and can be found in the **vertexingHF** folder of AliRoot.

5.2 Reconstruction method

The D^{*+} is a reconstructed particle. The reason this particle has to be reconstructed is that it has a mean life-time of $6.9 \pm 1.9 \cdot 10^{-21}$s which implies that even if it goes with the speed of light it has a mean path of 2.1 pico meter before decaying which is far too small to reach any detectors. The main hadronic decay mode of this particle is $D^{*+} \rightarrow D^0\pi^+$ with a branching ratio of $67.7 \pm 0.5\%$ [8]. This is the decay mode this thesis will focus on and for which the yield will be reconstructed.[27]
This decay contains a so called soft pion, which is a pion that carries very little energy, and a D^0 meson. This D^0 will also decay in $410.1 \pm 1.5 \cdot 10^{-15}$s, before it can reach the detector, so it is reconstructed from its decay products. The D^0 decay used is $D^0 \rightarrow K^-\pi^+$, which has a branching ratio of $(3.88 \pm 0.05)\%$ [8].
.

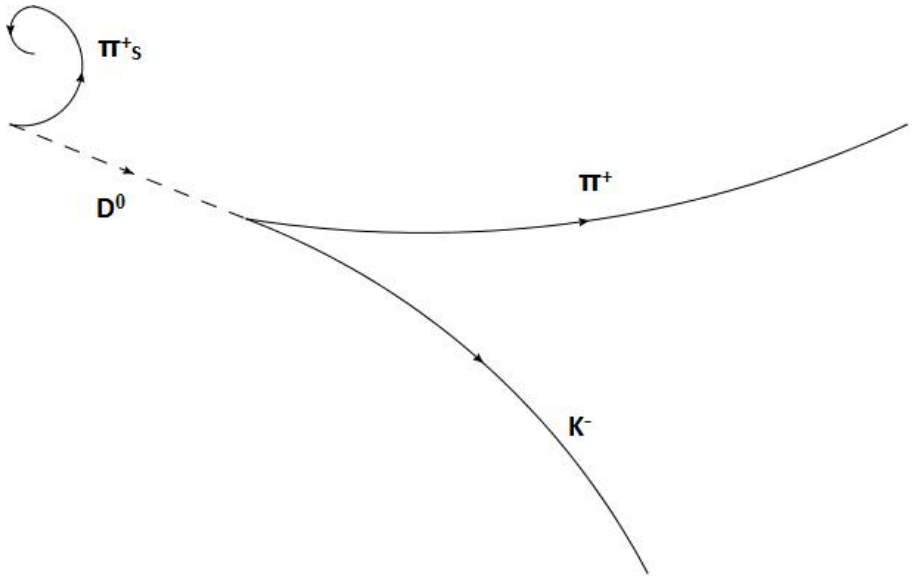

Figure 89: Sketch of a $D^{*+} \rightarrow D^0\pi_s^+ \rightarrow K^-\pi^+\pi_s^+$ decay. [18]

[27]The others are $D^{*+} \rightarrow D^+\pi^0$ and $D^{*+} \rightarrow D^+\gamma$, taken from the Particle Data Group charm mesons, version 2012.

The decay products of many processes are detected and through multiple detectors their momentum and paths are reconstructed. Of these particles selections are made to exclude particles that coming from different decays and from the accepted reconstructed particles the amount of D^{*+} is extracted. Strict selections of the particles used in the reconstruction are made to reject background, while the selection may not be so strict that reconstructions within the errors of the detector are rejected.
In the recognition of the decay product, the selection has to be strict enough to exclude other species while keeping into mind that mild fluctuations of the mass with respect to the real mass must be accepted. These fluctuations could be due to detector uncertainties in the measurement of momentum of the particle which is used to calculate the mass. Thus cutting too strictly can lead to either missing data or miss identification. Even if a particle is identified the selections or cuts have to be made carefully as the uncertainties can still influence the measurement.
Note that whenever the D^{*+} is mentioned the D^{*-} has also been taken into account for which the charge conjugation of all particles should be considered.

5.3 Topological selections for the reconstruction

The topological selections that are used are first explained. The precise values that will be used for the extraction of the yield can be found in Appendix C.

- (D0) Invariant Mass Window allowed for the D^0 (max)
  The allowed deviation of the reconstructed D^0 mass from the current Particle Data Group (PDG) value[8].

- (D0) DCA Distance of Closest Approach (max)
  The distance of closest approach between the, non soft, pion and kaon. The distance should be close to zero because if these particles are from a decayed D^0 they should come from one point, and every deviation from that should come from small impreciseness of the measurements.

- (D0) Cosine of the θ^* angle (max)
  θ^* is the angle between the path of the kaon and the direction in which the D^0 would have continued had it not decayed. The cosine of this angle peaks if the difference between them is zero. This cuts of those kaons which are not really decayed from the D^0 as the pion is not supposed to be soft.

- (D0) p_T Kaon (min)
  The kaon must have a minimal momentum to take care of the energy difference ($1,864.84$ MeV/c^2 versus $139.57 + 493.67 = 633.24$ MeV/c^2).

- (D0) p_T Pion (min)
  The pion must also have a minimal momentum, to make sure the energy difference between D^0 and the masses of the pion and the kaon is possible.

- (D0) $|d_0|$ Kaon (max)
  This is calculated by using the reconstructed path of the kaon followed by calculating the shortest distance with respect tot the primary vertex.

- (D0) $|d_0|$ Pion (max)
  This is calculated by using the reconstructed path of the pion followed by calculating the shortest distance with respect tot the primary vertex.

- (D0) $d_0 \times d_0$ (max)
  The product of the impact parameters is the maximal allowed product of the two previously mentioned parameters, which can be negative if they are on different sides of the primary vertex. Due to kinematics it is asymmetric on the negative side for pions and kaons coming from the chosen process.

- (D0) $\cos\theta_{point}$ (min)
  The angle θ_{point} is the angle between the reconstructed D^0 momentum and the vector pointing from the primary vertex to the point of the secondary vertex. The cosine of this angle tends to be a lot closer to 1 for D^{*+}/D^0 than for combinatorial background.

- (D^*) invariant mass half width of D^* (max)
  The full width at half minimum of the Gaussian representing the D^{*+} peak.

- (D^*) half width of $(M_{K\pi\pi} - M_{D^0})$ (max)
  The full width at half minimum for the difference between a reconstruction of the $k\pi\pi$ minus the mass of the associated reconstructed D^0. Takes out background in an earlier stage, and is here to cut down in computer time.

- (D^*) Minimal p_T of π_s
  The pion should have a low p_T, thus it has to have a small momentum, but not too small in order to not exclude high momentum D^{*+}. The two π_s momenta cuts are thus meant to give a minimum and a maximal momentum for this pion.

- (D^*) Maximal p_T of π_s
  As mentioned with the minimal p_T for π_s, ensures it is a soft pion.

- (D^*) Angle between the π_s and the decay plane of the $D0$ [rad] (min)
  The angle between the soft pion and the D^0 plane, this cut checks if these particles have possibly decayed from one particle. Therefore a minimal angle between them in needed.

- (Pb-Pb) |cos Theta point XY|

- (Pb-Pb) NormDecayLength XY

- (PID) PID strategy

The () name given to the selection criteria is to identify which process this selection is influenced by. The D^0 cuts are demands that will ensure there was a D^0 created, the pion in those selections is always the pion coming from the D^0. The D^* cuts are the demands in place to make sure there is a decay of the D^* to D^0, π_s. The $Pb - Pb$ cuts will not be studied here as they are not used in this reconstruction, they are quite strict cuts used to take out a lot of background in lead-lead collisions. The last category is the PID cut, which contains the PID strategy which is meant to reject reconstruction particles that have been identified as a different species.
Note that if a D^0 or D^{*+} mass or momenta is mentioned it is the reconstructed momentum or mass found by reconstruction of a possible candidate for a D^0 or D^{*+}.

5.3.1 PID strategy

The PID strategy is set up to be optimally efficient for the signal while excluding combinatorial background. On both TOF and TPC do a 3 σ cut is applied. As was shown in the QA-PID section of this thesis for high momenta the particles are barely distinguishable. So for very high momenta more particles will be accepted and for these momentum ranges this will be a less successful background cut. In figure 84 it was shown that the new splines have improved the efficiency of the particle identification compared to the old splines. The 1-2 GeV/c range is not to be taken into consideration, as no significant D^{*+} peak was found due to the trigger requirements of 2.01 GeV cluster energy.

5.4 Optimization

The optimization was done with a multidimensional optimization code. Not all selections have been optimized as there is not a lot to gain by most, while the computational cost grows extensively in higher dimension. Thus the focus is on those selection criteria from which there is the most to gain, their identities are known from previous analyses. These are three selection criteria used for the reconstruction of the D^0, namely: the product of the impact parameters ($d_0 \times d_0$), the distant of closest approach between the Pion and Kaon (DCA) and the cosine of the pointing angle ($\cos\theta_{point}$).
A multidimensional approach was chosen, because the multiple criteria effect one another. If there is a tight selection with respect to one criterion and another criterion is tightened it is possible to cut away signal. So by checking all three in all combinations, aka multidimensional, the best results are received. As the the optimal situation could not be simulated, due to the fact that the Monte Carlo simulation was not yet available, the 7 TeV optimal situation was used as a base and a data driven optimization was done.
For the ranges of the variations there were two criteria: the maximum had to be within the cut ranges and the detector precision had to be taken into account. For instance the DCA has a precision of about 0.003 cm, thus difference smaller than that are due to fluctuations.
The selection criteria are optimized with respect to the significance, however for the optimization to be correct there were demands on the Gaussian to which the peak is fitted, in order to reject fits coming from something else than the signal of the D^{*+}. A rejection was done if the mean of the Gaussian was to far away from to mass-difference between the $D^{*+}$and D^0 or the σ was too large. The later was done to exclude fits that do not correctly distinguish between the background and the signal, as these fits have a very wide Gaussian containing not only the signal but also a large amount of background. The fit was rejected if σ >0.95 MeV/c^2 for D^{*+} with a p_T below the 16 GeV/c and for $\sigma > 1.2$ MeV/c^2 for higher p_T D^{*+} mesons. Starting from these demands the first p_T range with reasonable data, 2-3 GeV/c, could not be optimized as the combination of the trigger influence and a very large background rejected most fits. Due to these effects the fits where to wide or to small and both are not considered signal. Therefore the optimization of the $2-3$ GeV/c p_T range was not possible, thus the best approximation has been used. The optimization gave significant results for momenta ranges between 3 and 60 GeV/c and for these ranges the optimization value was used for the yield extraction.
Note that for this optimization the EMCal7 triggered datasets LHC12A/B/C/D/E/F/G were used, which were not yet corrected for the improper working ϕ region, nor were data periods A and B excluded yet. However because these two data periods contain little statistics, they are not expected to influence the optimization process in such a way that optimizing without these periods will result in significantly different selection cuts.
In appendix D momenta ranges 2-5 and 6-36 GeV/c are shown, to illustrate the process the 5-6 GeV/c momentum range and the 36-60 GeV/c momentum range are shown, the later will be excluded for the final spectrum due to lack of statistics.

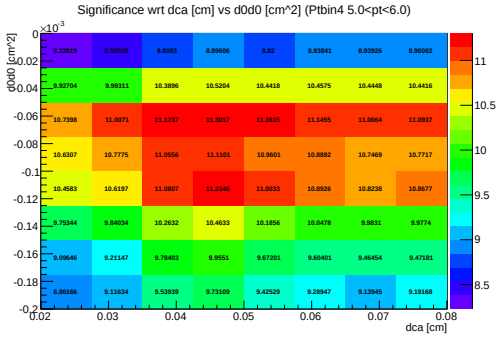

Figure 90: Significance values with respect to DCA [cm] vs $d_0 \times d_0$ [cm^2] for the 5-6 GeV/c D^{*+}p_T range.

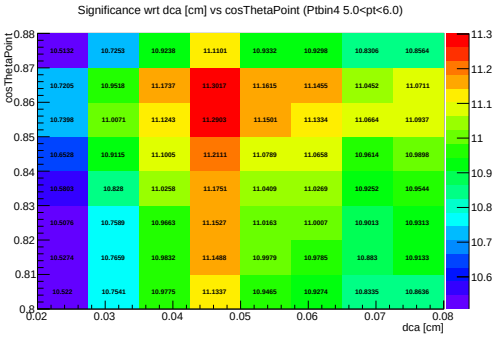

Figure 91: Significance values with respect to DCA [cm] vs Cos θ_{point} for the 5-6 GeV/c D^{*+}p_T range.

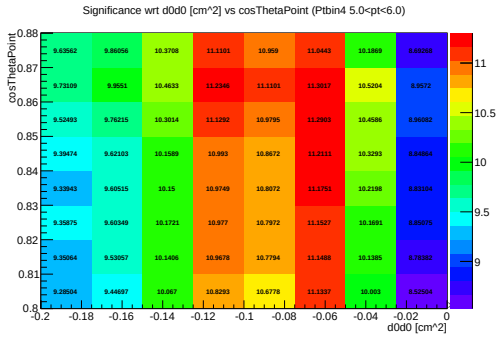

Figure 92: Significance values with respect to $d_0 \times d_0$ [cm^2] vs Cos θ_{point} for the 5-6 GeV/c D^{*+}p_T range.

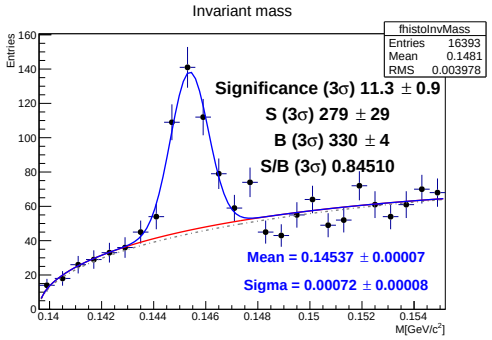

Figure 93: Invariant mass distribution of the K^-, π^+ combined with π_s pair, shifted back by the D^0 mass, with pair p_T range 5-6 GeV/c with the highest significance with respect to DCA, $d_0 \times d_0$ and Cos θ_{point}.

In figures 90, 91 and 92 the significance is mentioned with respect to the selection criteria shown on the axis. An optimal significance peak for a DCA of 0.047 cm combined with a $d_0 \times d_0$ of between -0.06 and -0.12 cm^2 and a cosine θ_{point} of 0.865 is found and shown in figure 93. This has been the selection process for most momentum ranges, while only considering selection criteria which can be reasonably stable and will give reasonable acceptance criteria for the D^{*+}.

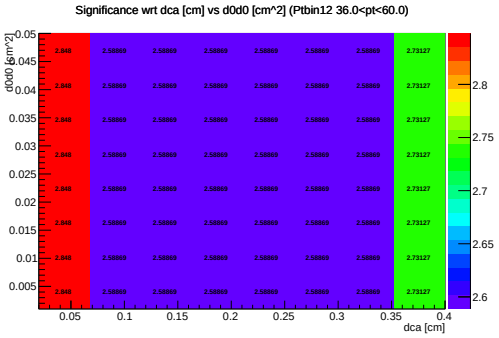

Figure 94: Significance values with respect to DCA [cm] vs $d_0 \times d_0$ [cm^2] for the 36-60 GeV/c D^{*+} p_T range.

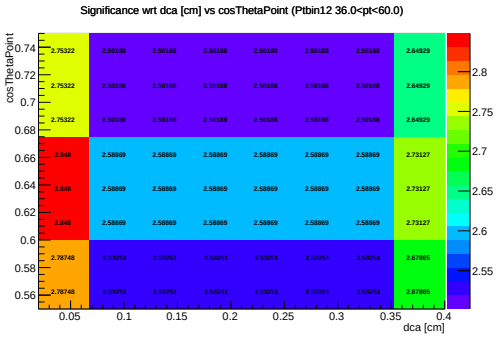

Figure 95: Significance values with respect to DCA [cm] vs Cos θ_{point} for the 36-60 GeV/c D^{*+} p_T range.

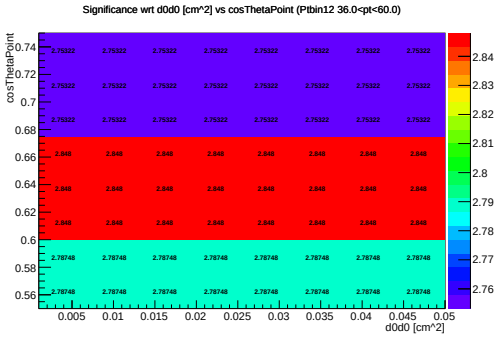

Figure 96: Significance values with respect to $d_0 \times d_0$ [cm^2] vs Cos θ_{point} for the 36-60 GeV/c D^{*+} p_T range.

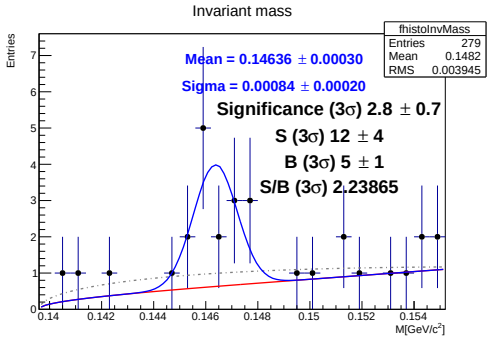

Figure 97: Invariant mass distribution of the K^-, π^+ combined with π_s pair, shifted back by the D^0 mass, with pair p_T range 36-60 GeV/c with the highest significance with respect to DCA, $d_0 \times d_0$ and Cos θ_{point}

For the highest momentum range the requirements were a priori assumed to be of no effects, as this low signal implies there would be no or hardly any background in this data. From figures 94 and 96 that can be concluded to be correct for the $d_0 \times d_0$. However if these significance distributions are combined with figure 95, it becomes clear that some significance can be gained by putting requirements on the DCA and cosine of the pointing angle. The gain is minimal, only 1 or 2 background reconstructions rejected. Figure 97 indicates that there are only 12 signal events, and 5 background points, thus even such a rejection can be useful. Therefore it is advised to use the optimal loose selection criteria on the DCA and the cosine angle. However as the significance still suffers from low statistics the choice has been made not to include this momentum range for this centre of mass energy, as this range will not yield significant results. The reconstructions done for this momenta indicate that a cross-section can be given up to 36 GeV/c as the range of our experiment has been proven to be larger than this for the chosen trigger and collision energy.

5.5 Systematic uncertainties

The optimized requirements (found in Appendix C) are used to extract the invariant mass distribution in figure 98.[28] This invariant mass distribution is not directly that of the D^{*+}reconstructed, but that of the $D^{*+} - D^0$. This shift means that one would expect a peak to be approximately at the difference between the PDG values of the D^{*+} and the D^0 thus at $2010.28 - 1864.86 = 145.42$ MeV/c^2. For the background function a background of the from $a\sqrt{\Delta M - m_\pi}e^{-b(\Delta M - m_\pi)}$ is used and the peak is fitted with a Gaussian fit. The blue lines in figure 98 contain the combination of the Gaussian and the background function. The background function itself is shown in red. The uncertainties shown are due to the statistical error. The choice of background function and peak function is further discussed in section 5.5.2.

In the following section the width and mean of the peak are discussed in order to check the quality with respect to the minimum bias triggers available for this analysis. The extracted mean and width of the invariant mass distribution should be within limited range of each other for each trigger, in order for it to be reasonably independent of the trigger.

After addressing this the systematic uncertainty is discussed, which is categorized into the systematic uncertainty on the yield, the uncertainty due to the particle identification process and the systematic uncertainty on the cut efficiency.

[28] A invariant mass distribution of triggers EMCal 7, EMCal 8, INT7, INT8, SPI7 and SPI8 combined uncorrected for overlap can be found in Appendix E

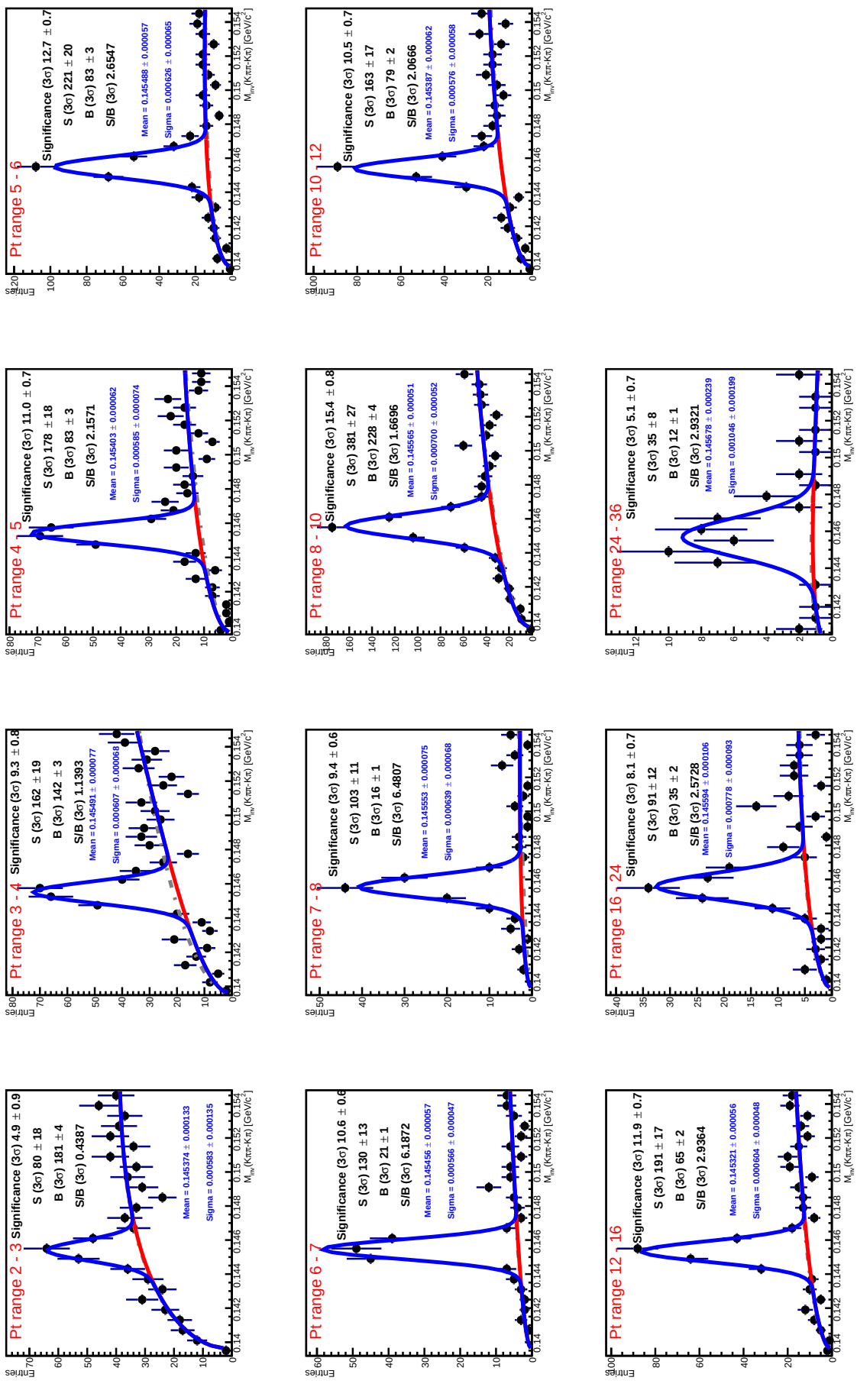

Figure 98: Invariant mass distribution of the $K^-\pi^+$ pair combined with π_s, shifted back by the D^0 mass, with pair pT range 2-36 GeV/c, EMCal 7 trigger for pp collision at $\sqrt{s} = 8$ TeV.

5.5.1 Mean and width

The peak position of the Gaussian with respect to the reconstructed momentum of the D^{*+} is shown in figure 99 and compared with those values found for the same cuts but different trigger, as well as the PDG value (black line). The width of the Gaussian that is used to fit the D^{*+} meson peak is due to the effects of the detector, the width will be compared to those widths found for different triggers in figure 100.
A particle spectrum, without detector effect, consists of a flat distribution with a sharp Breit-Wigner peak at those energies that are precisely equal to the mass of a particle. However the detectors influence our measurements, the shape and width are influenced such that the Breit-Wigner peak becomes a Gaussian. The detectors effect is smallest for those energies for which the detector functions optimally, the optimum for kaons and pion coming from a D^{*+} meson is reached for kaons and pions coming from D^{*+} mesons with a transverse momentum between 4 and 8 GeV/c. Thus the width is expected to be the smallest at those momentum ranges and the width is expected to increase if the momentum difference increases.
The EMCal biased sample will be shown in comparison to the two minimum bias samples, INT7 and SPI7 triggered, to check if the mean and width are independent of the trigger.

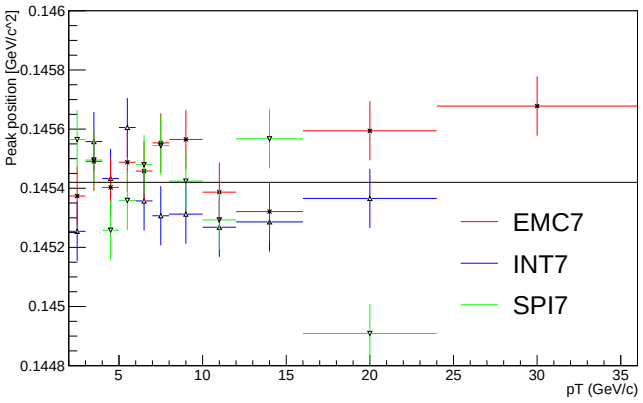

Figure 99: Mass difference between the D^{*+} and D^0 found per p_T range.

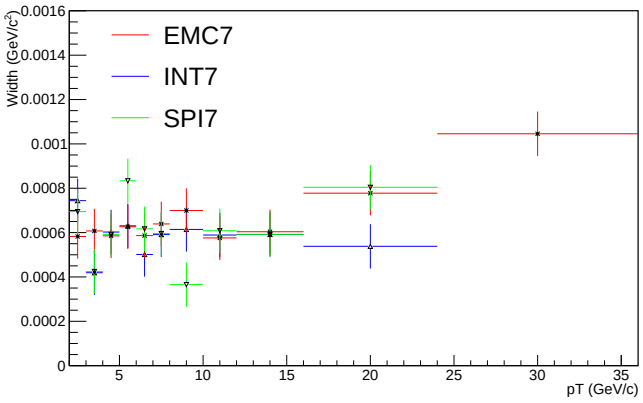

Figure 100: Sigma (width) difference between the D^{*+} and D^0 found per p_T range.

There is no peak found for the minimum bias triggers for the 24-36 GeV/c region as the statistics are too low for those triggers. Note that peak for their last bin (16-24 GeV/c) while still quite acceptable for the Int 7 (21 points of signal and a significance of 4.2), was not significant for the SPI7 (10 points and a significance of 3), therefore the difference between the values at that momentum range could be due to the statistics. With respect to the peak position take into account that the range shown is 0.0012 GeV/c^2 which is $< 1\%$ of the mass of the particle, thus any difference shown is $< 0.5\%$ of the mass.
For the width, the typical increase of the width for low momenta is missing, which is possibly due to the selection criteria used. These criteria are optimal for the EMCal 7 trigger which is suppressed in these ranges due to trigger effects, however the criteria are not optimized for the minimum biased triggers. For higher momentum ranges it is concluded that the width increases as expected as the measurements are outside the optimal range of the detectors.

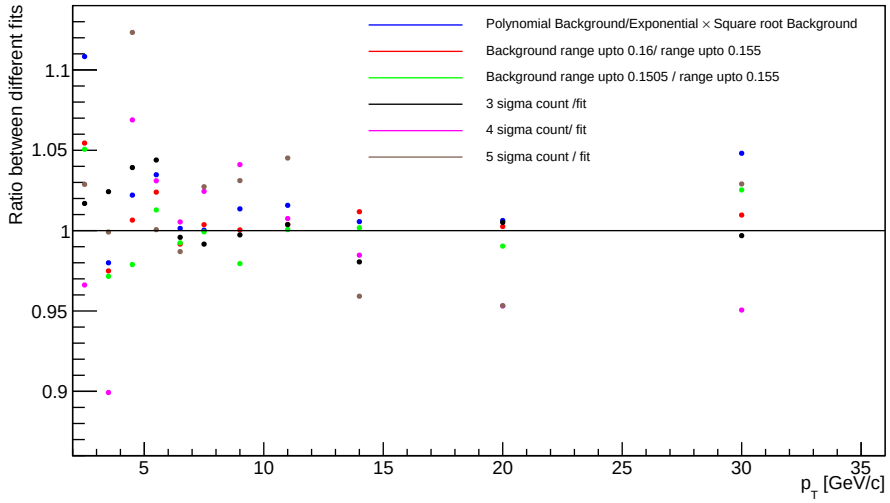

Figure 101: Ratio between the different fittings and counting ranges, the systematic error on the yield (due to the fit) is given by $|1 - ratio| \cdot yield$.

5.5.2 Yield extraction.

A statistical error is extracted from the fits, but this uncertainty does not take into account the effects of the range, background function, particle identification process or the effects of the cuts as those effects are systematics. In this section the systematic uncertainty on the yield extraction will be considered, taking into account the effects of the fitting range, the background function and the fit of the peak.
For the background function a background of the form $a\sqrt{\Delta M - m_\pi}e^{-b(\Delta M - m_\pi)}$ is used and alternatively a background of the from $a(\Delta M - m_\pi)^b$. The upper limit of the fitting range varies between 0.1505, 0.155 and 0.16 GeV/c^2, with a constant lower limit of the pion mass. Finally the fit of the peak is discussed with respect to signal counting. The counting is done within 3,4 or 5 sigma of the peak position, and the difference between the background function and the data points is extracted.
If the background and Gaussian mimic reality perfectly the counting of the data points only deviates of the integral under the peak due to statistics, which averages out. These deviations of the yield extraction approximate the systematic uncertainty due to the fitting of the yield. These systematic uncertainties are expected to be within 5% of the data, which implies that the model mimics the results up to 3σ.
There are some larger errors in the low momenta range (2-5 GeV/c) as is shown in figure 101. The lowest momentum range has relatively low statistics and is easily influenced by the choice of background function due to high background. For this range the relatively large error should be excepted. For the 3-4 GeV/c momentum range there are large statistical fluctuations, as can be seen in the mass distribution for lower masses there are a few high fluctuations that are close together and including one inside the counting without the lower fluctuations could cause such a high errors. In the 4-5 GeV/c range there is a relatively large fluctuation just above the mass of the Gaussian the background seems to be a little bit underestimated. If a larger range than 5 σ would be considered for the counting the difference with respect to the fit will decrease as this range misses some the lowering fluctuations that occur for a slightly higher reconstructed mass[29]. These fluctuations strongly increase the systematic uncertainties in the 2-5 GeV/c momentum ranges.

[29]Note that it counts from 0. 1434 till 0.1484 approximately which means one just misses the points where it drops down again, see figure 98.

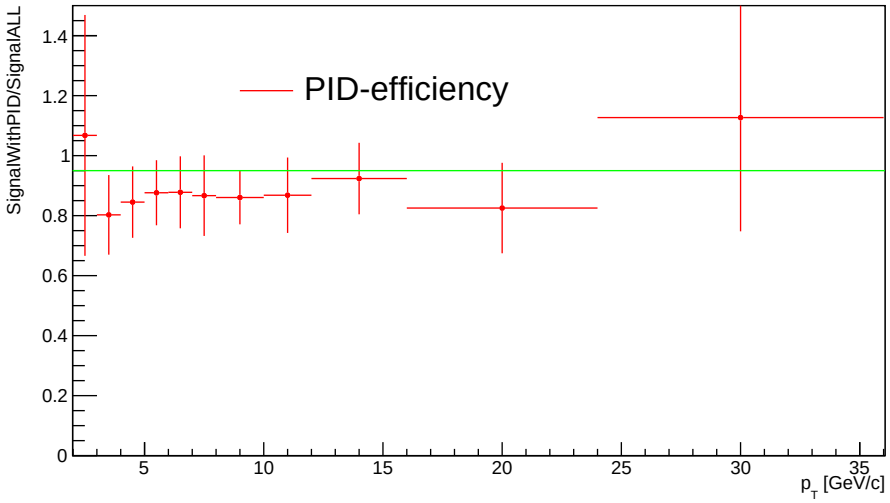

Figure 102: Ratio between the raw yield measured with and without PID

5.5.3 PID cuts

The PID strategy is designed such that the combined signal loss from the cuts on the particle identification detectors is expected to be in the range of 5%. However as mentioned in the QA the PID is not optimal for these periods. It is still not clear if the results are due to the normalization, or that a Monte Carlo simulation would also predict some differences here.

In figure 102 the lowest and highest p_T ratios are above 1. These are fluctuations, as extra statistics are not introduced when using PID. For the first momentum bin the explanation lays in the bad fit of the peak without PID, which therefore misses a couple of data point. For the $24 - 36$ GeV/c momentum range the low statistics influence the result, with PID the Gaussian fitted on the peak is a little broader, because a data point which gave some fluctuation on the edge of the Gaussian is filtered out. The difference for this last bin is completely within the systematic error of the fitting, and is therefore not considered problematic.
Overall the PID efficiency is factor 2 to 3 lower than would be expected, which results in relatively large systematic uncertainties due to the PID. This might be either explained or corrected with the Monte-Carlo simulations or the new reconstruction of the data.

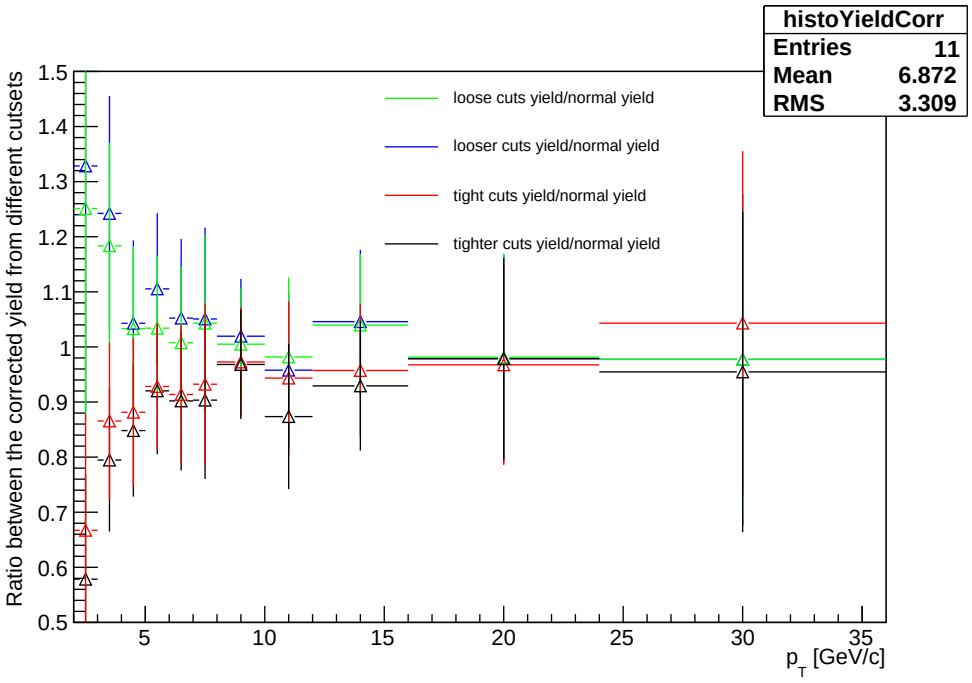

Figure 103: Ratio between the corrected yields which were corrected with $\sqrt{s} = 7$TeV MC minimum bias efficiencies.

5.5.4 Cut variation

The stability of the cuts chosen gives rise to the systematic uncertainty due to the chosen cuts. This uncertainty is calculated by varying the DCA, the $d_0 \times d_0$ and the cosine of the pointing angle. For low p_T ranges (2-8 GeV/c) the varying of the cuts was done with a variation of 15-20 % for the DCA and the $d_0 \times d_0$, and a variation of approximately 10% for the cosine of the pointing angle. For high p_T (8-36 GeV/c) the varying of the cuts was done with a 20-40% variation for the DCA and the $d_0 \times d_0$, and a variation of approximately 10-20% for the cosine of the pointing angle. This distinction was made to demonstrate the limited influence of the cuts at high p_T.

Note, regarding figure 103, that the large systematic uncertainty for the reconstructed particles with a momentum between the 2 and 4 GeV/c is not necessarily due to the cuts. In these momenta regions the trigger can influence the particle yield strongly, as in these ranges a lot of D^{*+} could be missed due to the trigger. Whether this effect is due to the trigger or something else can be understood through Monte-Carlo simulations with and without this trigger present, which are currently unavailable.

6 D^{*+} production cross-section

The extraction of the yield as well as the first production cross-section will be discussed. This will be followed by a conclusion and outlook on the results in which the improvements necessary for publications are discussed.

6.1 D^{*+} yield

The raw-yield is the amount of particles extracted from the background after the selection criteria have been used on the data samples. This is done by making a fit with a background of the form $a\sqrt{\Delta M - m_\pi}e^{b(\Delta M - m_\pi)}$ combined with a Gaussian peak function.
For the systematic uncertainty the PID and the systematic uncertainty on the yield extraction are taking into account as well as the tracking efficiency. The cut efficiency is not taken into account as it extracted via the $\sqrt{s} = 7$ TeV Monte Carlo simulations, and can therefore be influenced by the incorrect simulation. The error in the tracking efficiency is assumed to be 12%.

p_T interval [GeV/c]	Raw Yield ± stat. unc. ± syst. unc.
2-3	$80 \pm 18 \pm 10$
3-4	$162 \pm 19 \pm 42$
4-5	$178 \pm 18 \pm 43$
5-6	$221 \pm 20 \pm 40$
6-7	$130 \pm 13 \pm 22$
7-8	$101 \pm 11 \pm 18$
8-10	$381 \pm 27 \pm 72$
10-12	$163 \pm 17 \pm 29$
12-16	$191 \pm 17 \pm 29$
16-24	$91 \pm 12 \pm 20$
24-36	$35 \pm 8 \pm 6$

Table 3: Table of the raw yield extracted from $\sqrt{s} = 8$ TeV pp measurements in an EMCal 7 triggered data set.

6.2 D^{*+} cross-section

To extract a production cross-section the detector and cuts efficiencies are taken into account, as well as the different processes that could create a D^{*+} meson. The process for which the cross-section will be extracted is the direct c-quark hadronization to D^{*+}, thus the results will be corrected for the $B \rightarrow D^{*+}$ processes. The production cross-section is formulated as:

$$\frac{\mathrm{d}\sigma^{\mathrm{D}^{*+}}}{\mathrm{dp_T}} \mid_{|y|<0.5} = \frac{1}{2}\frac{1}{\Delta y \Delta p_T}\frac{f_{prompt}(p_T)\cdot N^{\mathrm{D}^{*\pm}}(p_T) \mid_{|y|<y_{fid}}}{(Acc\times\epsilon)_{prompt}(p_T)\cdot Br \cdot L_{int}}. \tag{2}$$

Here $f_{prompt}(p_T)$ is the correction factor to take only the prompt fraction of the yield.
The $N^{D^{*\pm}}(p_T)$ is the raw yield as given in table 3.
The $(Acc \times \epsilon)_{prompt}(p_T)$ is the acceptance times the efficiency of the cuts, where in the cuts the vertex and track reconstruction are included as well as the efficiency of the cuts and the PID efficiency.
The factor $\frac{1}{2}$ in front of the cross-section is to calculate the cross-section for D^{*+} instead of $D^{*+} + D^{*-}$ and the $\Delta y = 2y_{fid}$ is the width of the fiducial rapidity coverage. This last term is used to correct for the rapidity coverage of the detector.

The Br and the L_{int} will now be addressed. The Br gives the branching ratio taken from the PDG[8] and the L_{int} is the integrated luminosity which is calculated as $L_{int} = N_{pp,emc}/\sigma_{pp}$ where $N_{pp,emc} \approx 33.1$M is the amount of Emcal 7 events and the σ_{pp} is the cross-section of the events. No measurements of the cross-section was available for this data set at the current date, thus an approximation of the σ_{inel} was used instead. Due to this the results will be calculated up to an normalization factor, with σ_{inel} =75mb used as an approximation for σ_{pp}. The $(Acc \times \epsilon)_{prompt}(p_T)$ and its correction for the rapidity coverage are based upon the 2010 7 TeV Monte Carlo set, which was based upon the GEANT3 transport code. The efficiency was calculated separately for B-mesons decaying into D^{*+} and for c quarks directly going to D^{*+}.
The $f_{prompt}(p_T)$ correction factor was calculated based upon similar factors as well as the FNOLL pQCD calculations for the beauty production, the kinematics for the B-meson to D^{*+} decay (EvtGen package) and the $(Acc \times \epsilon)_B$, which is the acceptance times efficiency for D mesons coming from B decays.
The formula of f_{prompt} gives us:

$$f_{prompt}|_{|y|<y_{fid}} = \frac{1}{N^{\mathrm{D}^{*\pm},\mathrm{raw}}} \left(N^{\mathrm{D}^{*\pm},\mathrm{raw}} - \left(2 \frac{\mathrm{d}\sigma^{\mathrm{D}^{*+},\,\mathrm{from\,B}}_{\mathrm{FNOLL\,pQCD}}}{\mathrm{dp_T}}|_{|y|<0.5} \cdot \Delta y \Delta p_T \cdot (Acc \times \epsilon)_B \cdot Br \cdot L_{int} \right) \right). \tag{3}$$

This is the method depending the least on the pQCD calculations, alternatively it is also possible to use:

$$f_{prompt} = \left(1 + \frac{Acc \times \epsilon)_B}{(Acc \times \epsilon)_{prompt}} \frac{\frac{\mathrm{d}\sigma^{\mathrm{D}^{*+},\,\mathrm{from\,B}}_{\mathrm{FNOLL\,pQCD}}}{\mathrm{dp_T}}|_{|y|<0.5}}{\frac{\mathrm{d}\sigma^{\mathrm{D}^{*+},\,\mathrm{C}}_{\mathrm{FNOLL\,pQCD}}}{\mathrm{dp_T}}|_{|y|<0.5}} \right)^{-1} . \tag{4}$$

The first method was used in this thesis as it was shown in [4][30] that this method underestimates the D-mesons coming from charm less than the alternative method.

[30]The method for calculating the cross section has been taking from [4], the explanation of such methods has also been based upon this paper.

Production cross-section

The production cross section is shown in figure 104 including the systematic errors in the data sets based upon the current Monte Carlo simulation.

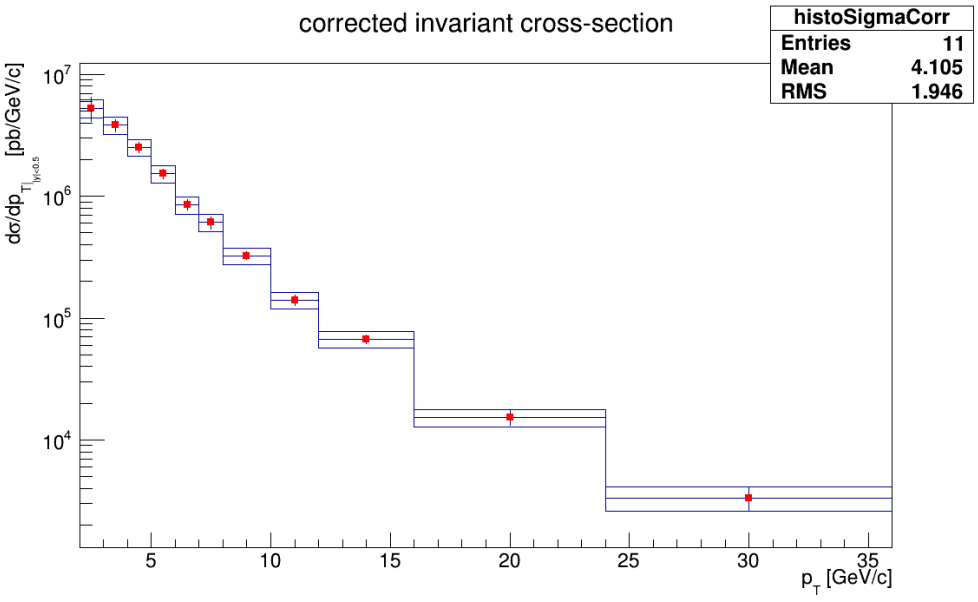

Figure 104: D^{*+} cross-section, corrected with $\sqrt{s} = 7$ TeV minimum bias efficiencies and using an inelastic $\sigma = 75$mb cross-section as estimate for the total pp cross-section.

The influence of the earlier mentioned systematic errors are discussed with respect to figure 105, which contains an overview of the systematic uncertainties with respect to the cross-section.

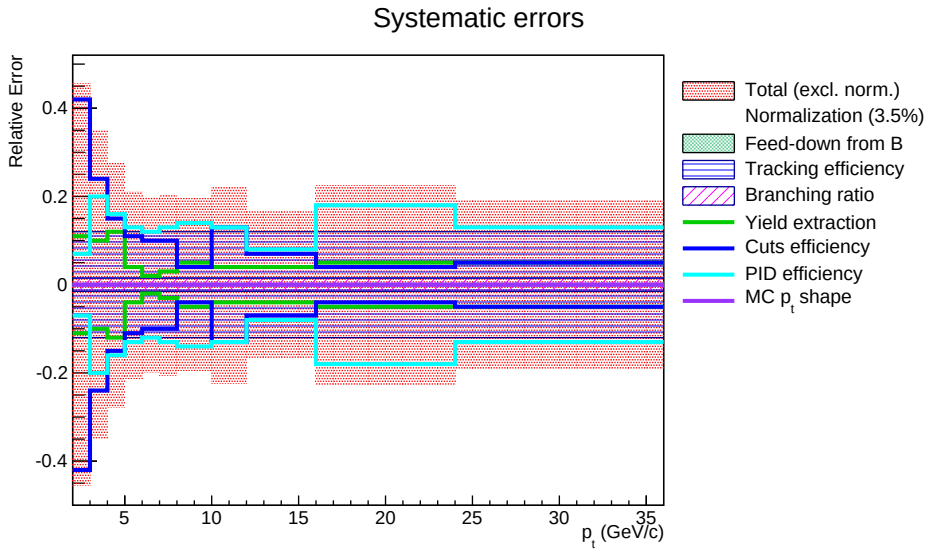

Figure 105: D^{*+} systematic errors with respect to the cross-section corrected with $\sqrt{s} = 7$ TeV minimum bias efficiencies and using an inelastic $\sigma = 75$mb cross-section as estimate for the total pp cross-section.

Due to the sensitivity of the cuts, the systematic uncertainty is large for D^{*+} with a low trans-

verse momentum compared to the uncertainty found in previous studies [4]. In the lowest momentum ranges it should be taken into account that at a range of 2-4 GeV/c the chosen trigger will have a strong influence on the results[31]. Therefore the low momenta bins can improve once they are matched with a Monte-Carlo simulation which does take this trigger into account. With respect to the $\sqrt{s} = 7$ TeV studies [4], the overall shape of the cross-section is considered reasonable. These results can be considered as a guideline for the later results that will be extracted with the new reconstruction of the data and the appropriate Monte-Carlo simulations.

[31] As is noted earlier the trigger has a cluster energy threshold of 2.01 GeV.

6.3 Discussion and Outlook

Discussion

In this second part of the thesis a production cross-section is extracted by combining the $\sqrt{s} = 8$ TeV pp collision sets LHC12C/D/E/F/G (2012) with Monte-Carlo simulations made for the detector situation for 2010 at $\sqrt{s} = 7$ TeV minimum bias pp data. These situation differ not only by centre of mass energy, but also by trigger and exact detector settings, which will influence the production cross-section extracted from this data.

The chosen trigger biases data differently than the trigger effects seen in minimum bias triggers. For low momenta a part of the events is excluded due to the trigger, which implies an underestimation of the low momentum data, and lingering effects are possible in higher momentum ranges.

As for the detector situation, from the quality assurance it can also be concluded that there are changes made in the detectors since 2010. On a positive note some SPD parts have been brought back to life, thus an improvement of the resolution of the ITS is expected. However it is not completely clear which of the differences found in the distributions with respect to the distributions found for lower energies are due to detector or normalization problems (as mentioned in section 4), and which come from new settings, which can be taken into account when doing the Monte-Carlo simulations.

Finally, the data that is used is the first reconstruction of the *pp* data of 2012, which has been found to have some flaws following the first part of this thesis. Therefore the after mentioned results can be slightly different once they contain the final data. The results mentioned in this thesis should be considered as an estimate of the final amount. The extraction process that was discussed is a correct process which will also be used in the final data sample.

Due to these issues with the data and the incorrect simulation it is possible that the effects of the cut efficiency are smaller both have been corrected.

As for a possible improvement on the statistics, the amount of statistics excluded due to the issues with the ITS is not significant. However, if high luminosity periods H and I could be corrected for and used in analyses, the uncertainties due to a lack of statistics can decrease.

The selection criteria are expected to be optimal for the new reconstruction. Due to the data-driven optimization process and because the new reconstruction will only correct local effects, the selection criteria are not expected to be influenced strongly. Thus the selection criteria, Appendix C, can be used to extract a final production cross-section, for which the shown production cross-section can be used as a prediction.

Outlook

When the new reconstruction of this data set will be done and the quality of that reconstruction is assured, a short check is advised to see if these results found are comparable to those found in this thesis. If this is the case, and a Monte-Carlo simulation for this specific data set and trigger is available, a rerun of the codes used in this thesis should be sufficient to find a precise D^{*+} cross-section. This could then be combined with the other D mesons for the overall cross-section.

Finally this thesis concludes that the extracted yield and production cross-section indicate that it is possible to look at higher momenta ranges if a non minimum bias trigger is used. This would lead to an expansion of the R_{AA} calculations for the D-mesons to a higher momentum region, improving the understanding of the effects of QGP on highly energetic heavy flavour particles. While at the same time these results indicate that it is possible to extract a complete production cross-section for the D-mesons and thus a charm cross-section for collision energies of $\sqrt{s} = 8$ TeV improving pQCD calculations.

7 Acknowledgements

I would like to thank those who taught me the language and 'the D-hadrons dialect' so to speak. First and foremost I thank my supervisor Alessandro Grelli and my group leader and supervisor André Mischke, for proposing the research and answering all silly and less silly questions that I got stuck on. I would also like to thank Chiara Bianchin, who supervised me during my CERN summer project and gave me the ropes to tackle the quality assurance to the best of my abilities. I also owe a big thank you to the entire D2H group of ALICE, as quite a lot of them pointed me to mistakes or problems and gave me ideas how to fix them. In the same sense the Utrecht/Nikhef ALICE group also contributed, giving me the space to learn, their time and explanations of tiny things I might have missed otherwise. Finally, I am thankful for the moral and spell-checking support of Darius, who always told me that, and what, I could do better.

A QA-TOF

From figures 106 to 110 it can be seen that the peak around zero (the red area), which is the pion peak, is quite clear, and the green arm, around 2 GeV/c from the top, is the influence of some kaons that are also seen. The biggest difference between these figures seems the difference in clearness. This due to a lack of events in period 12E and 12G, as this problem stays occurring only will be shown 12C/D/F for the kaons and protons.

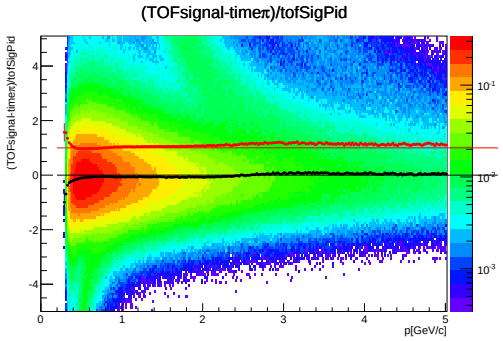

Figure 106: Data period 12C trigger EMCal JET7, amount of sigma for the difference between hypothesis for the pion time of flight and the measured as a function of pion momentum.

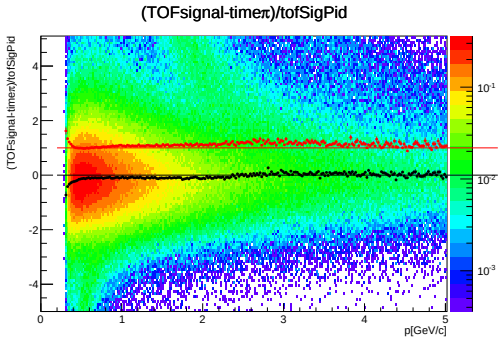

Figure 107: Data period 12E trigger EMCal JET7, amount of sigma for the difference between hypothesis for the pion time of flight and the measured as a function of pion momentum.

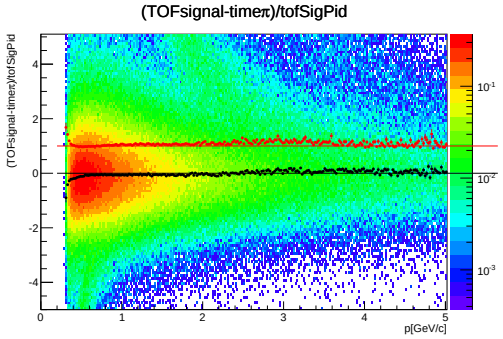

Figure 110: Data period 12G trigger EMCal JET7, amount of sigma for the difference between hypothesis for the pion time of flight and the measured as a function of pion momentum.

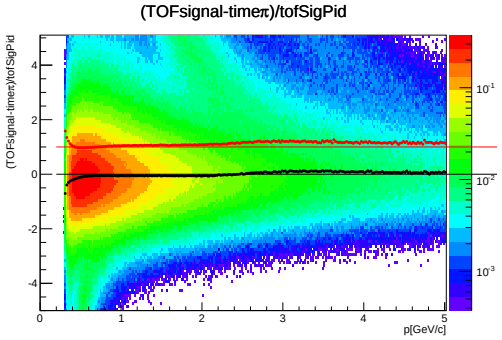

Figure 108: Data period 12D trigger EMCal JET7, amount of sigma for the difference between hypothesis for the pion time of flight and the measured as a function of pion momentum.

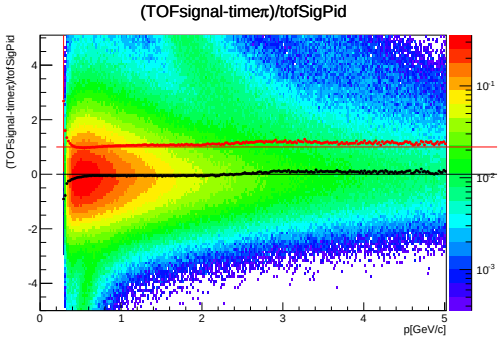

Figure 109: Data period 12F trigger EMCal JET7, amount of sigma for the difference between hypothesis for the pion time of flight and the measured as a function of pion momentum.

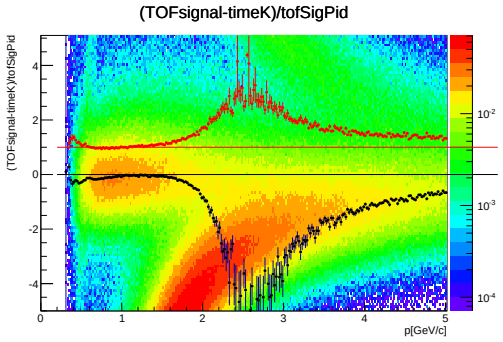

Figure 111: Data period 12C trigger EMCal JET7, amount of sigma for the difference between hypothesis for the kaon time of flight and the measured as a function of kaon momentum.

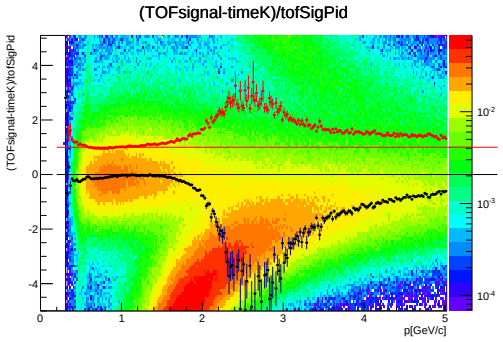

Figure 112: Data period 12D trigger EMCal JET7, amount of sigma for the difference between hypothesis for the kaon time of flight and the measured as a function of kaon momentum.

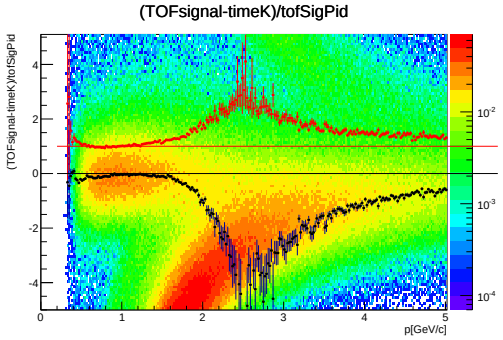

Figure 113: Data period 12F trigger EMCal JET7, amount of sigma for the difference between hypothesis for the kaon time of flight and the measured as a function of kaon momentum.

In figures 111, 112 and 113 it can be seen that the kaons, being less common, have less neat figures. However, they are still separable and all the peaks seen in the figure can be identified. Note that the left peak comes from the kaons, the lower peak results from the pions and the upper right arm comes from the protons.

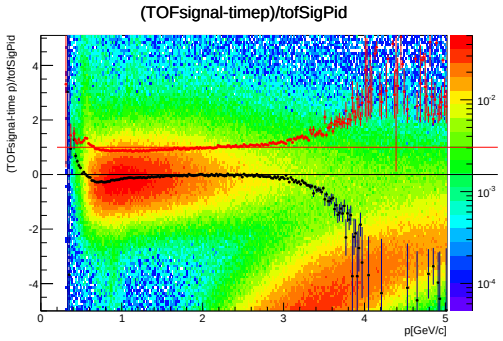

Figure 114: Data period 12C trigger EMCal JET7, amount of sigma for the difference between hypothesis for the proton time of flight and the measured as a function of proton momentum.

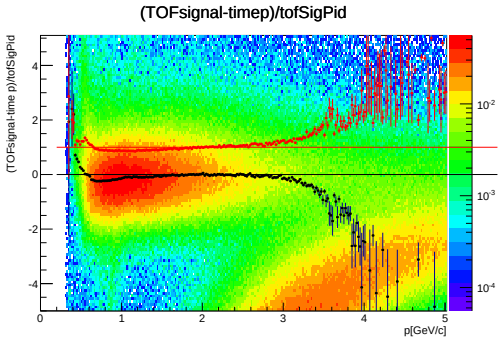

Figure 115: Data period 12D trigger EMCal JET7, amount of sigma for the difference between hypothesis for the proton time of flight and the measured as a function of proton momentum.

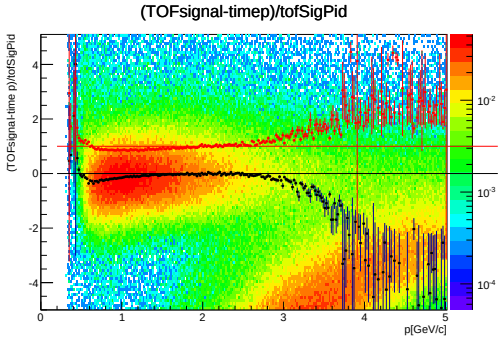

Figure 116: Data period 12F trigger EMCal JET7, amount of sigma for the difference between hypothesis for the proton time of flight and the measured as a function of proton momentum.

The protons in figures 114, 115 and 116 seem less good, but this is also partly due to the limited amount of data that was used here. The results shown here are within reasonable limits and the corresponding TOF data will therefore be used.

B QA-TPC

B.1 Protons

The last three Proton figures.

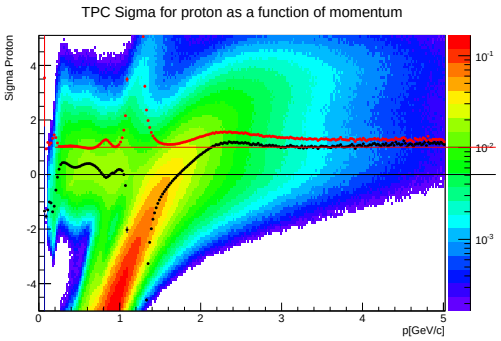

Figure 117: TPC Sigma Proton versus momentum period 12a

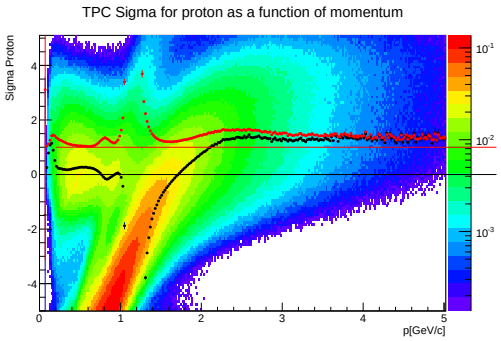

Figure 118: TPC Sigma Proton versus momentum period 12b

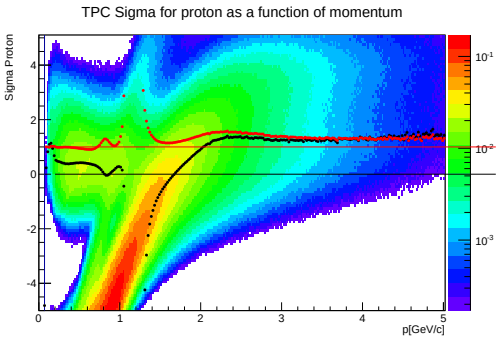

Figure 119: TPC Sigma Proton versus momentum period 12c

B.2 Pions

The first three Pion figures.

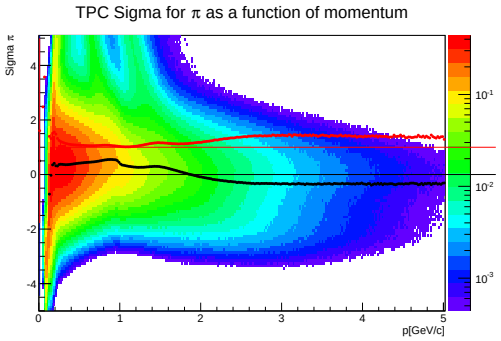

Figure 120: TPC Sigma Pion versus momentum period 12a

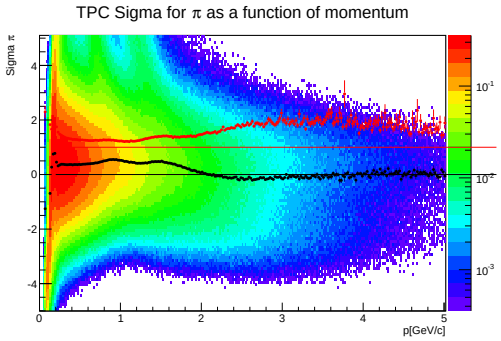

Figure 121: TPC Sigma Pion versus momentum period 12b

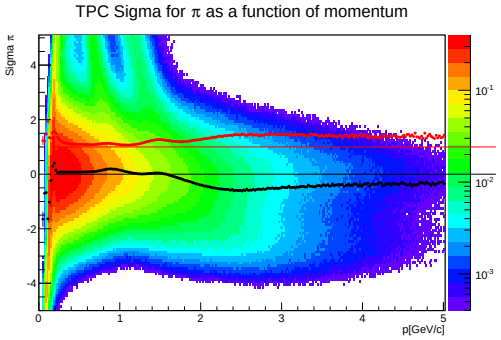

Figure 122: TPC Sigma Pion versus momentum period 12c

The last four Pion figures for the TPC.

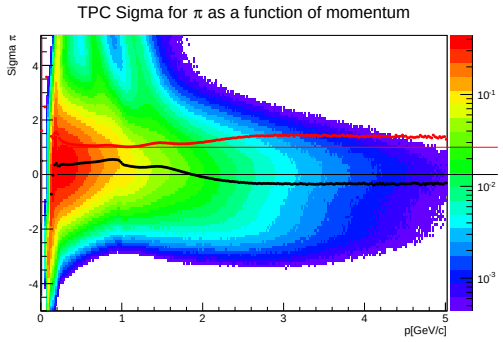

Figure 123: TPC Sigma Pion versus momentum period 12d

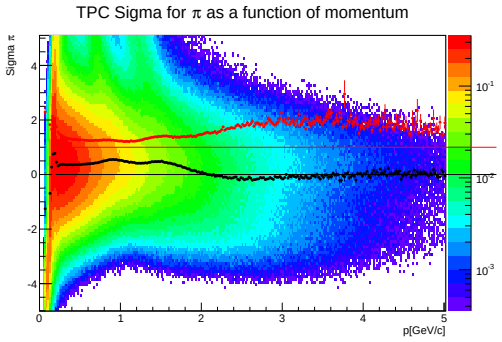

Figure 124: TPC Sigma Pion versus momentum period 12e

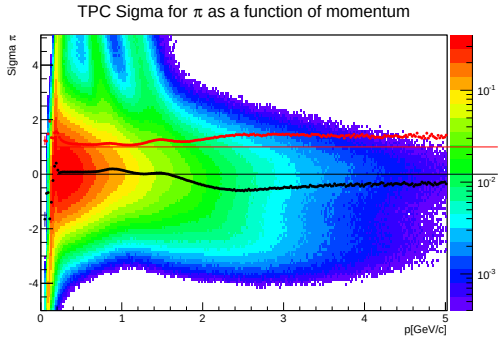

Figure 125: TPC Sigma Pion versus momentum period 12f

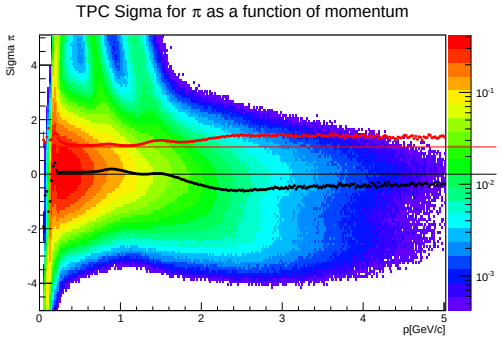

Figure 126: TPC Sigma Pion versus momentum period 12g

B.3 Kaons

The first three Kaon figures.

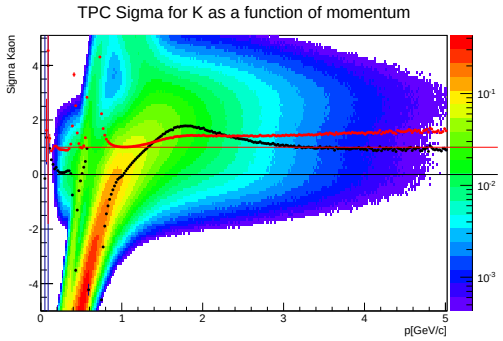

Figure 127: TPC Sigma Kaon versus momentum period 12a

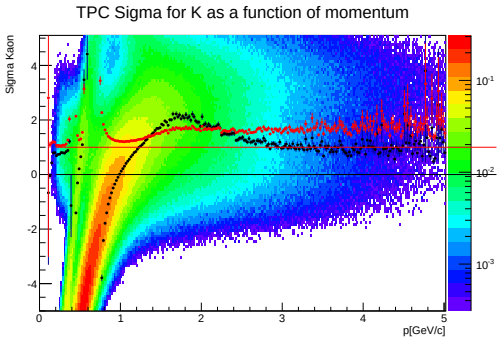

Figure 128: TPC Sigma Kaon versus momentum period 12b

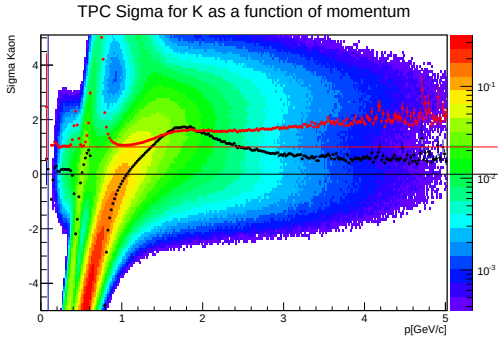

Figure 129: TPC Sigma Kaon versus momentum period 12c

The last four Kaon figures for the TPC.

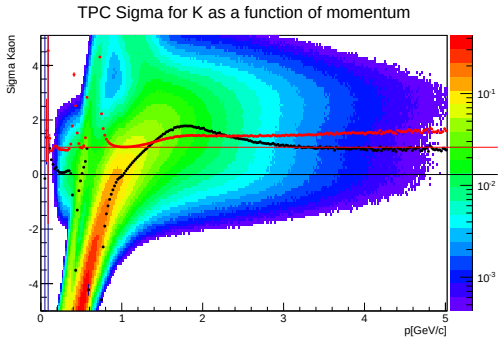

Figure 130: TPC Sigma Kaon versus momentum period 12d

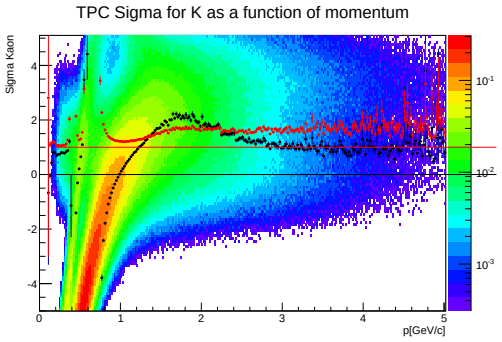

Figure 131: TPC Sigma Kaon versus momentum period 12e

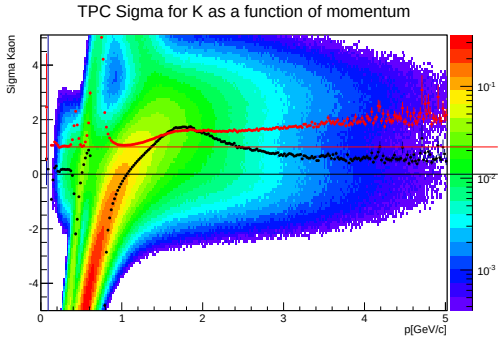

Figure 132: TPC Sigma Kaon versus momentum period 12f

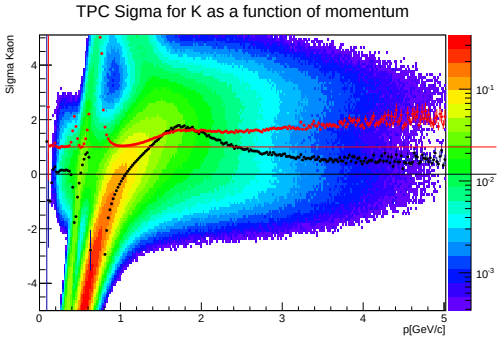

Figure 133: TPC Sigma Kaon versus momentum period 12g

C Selection Criteria

The D^{*+} p_T range has been given above the amount.

Cut parameter	2-3 [GeV/c]	3-4 [GeV/c]	4-5 [GeV/c]	5-6 [GeV/c]	6-7 [GeV/c]	[7-8 GeV/c]
Inv. Mass Window D^0 [GeV/c^2]	0.32	0.32	0.32	0.36	0.36	0.4
DCA [cm]	0.025	0.035	0.035	0.05	0.035	0.035
$cos\theta^*$	0.8	0.8	0.9	1	1	1
p_T kaon [GeV/c]	0.8	1	0.8	0.6	0.8	0.6
p_T non-soft pion [GeV/c]	0.8	1	0.8	0.6	0.8	0.6
d_0 kaon [cm]	0.1	0.1	0.1	0.1	0.1	0.1
d_0 pion [cm]	0.1	0.1	0.1	0.1	0.1	0.1
$d_0 \times d_0$ [cm^2]	-0.00019	-0.000101	-0.0001	-0.00005	-0.00005	-0.00005
$cos\theta_{point}$	0.905	0.905	0.8	0.86	0.794	0.835
Inv mass half-width D^{*+} [GeV/c^2]	0.3	0.3	0.2	0.15	0.3	0.3
Half-width $M_{K\pi\pi} - M_{D^0}$ [GeV/c^2]	0.15	0.15	0.15	0.15	0.15	0.15
p_T min soft pion [GeV/c]	0.05	0.05	0.05	0.2	0.2	0.2
p_T max soft pion [GeV/c]	0.5	0.5	10	10	100	100
Angle between π_s and decay plain of D^0 [rad]	1	1	1	1	1	1
$\lvert cos\theta_{pointXY}\rvert$	0	0	0	0	0	0
Norm decay Length XY	0	0	0	0	0	0

Cut parameter	8-10 [GeV/c]	10-12 [GeV/c]	12-16 [GeV/c]	16-24 [GeV/c]	24-36 [GeV/c]
Inv. Mass Window D^0 [GeV/c^2]	0.55	0.7	0.94	0.74	0.3
DCA [cm]	0.0725	0.07	0.045	0.05	0.125
$cos\theta^*$	1	1	1	1	1
p_T kaon [GeV/c]	0.5	0.4	0.3	0.3	0
p_T non-soft pion [GeV/c]	0.5	0.4	0.3	0.3	0
d_0 kaon [cm]	0.1	0.1	0.1	0.1	999999
d_0 pion [cm]	0.1	0.1	0.1	0.1	999999
$d_0 \times d_0$ [cm^2]	0.007	0.0005	0.00025	0.000575	0.002125
$cos\theta_{point}$	0.62	0.84	0.85	0.8225	0.85
Inv mass half-width D^{*+} [GeV/c^2]	0.3	0.3	0.3	0.3	0.3
Half-width $M_{K\pi\pi} - M_{D^0}$ [GeV/c^2]	0.15	0.15	0.15	0.15	0.1
p_T min soft pion [GeV/c]	0.3	0.3	0.3	0.05	0.05
p_T max soft pion [GeV/c]	100	100	100	100	10^{13}
Angle between π_s and decay plain of D^0 [rad]	1	1	1	1	1
$\lvert cos\theta_{pointXY}\rvert$	0	0	0	0	0
Norm decay Length XY	0	0	0	0	0

D Optimization figures

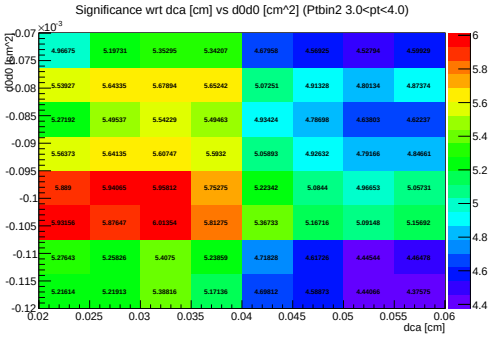

Figure 134: Significance values with respect to DCA [cm] vs $d_0 \times d_0$ [cm^2] for the 3-4 GeV/c D^{*+} p_T range.

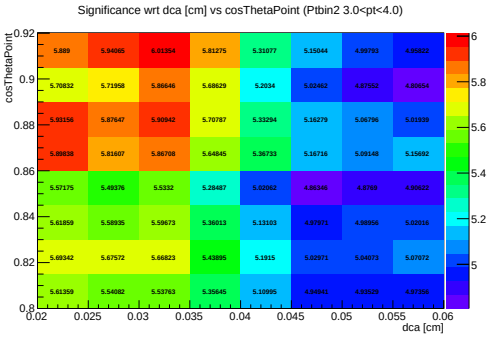

Figure 135: Significance values with respect to DCA [cm] vs Cos θ_{point} for the 3-4 GeV/c D^{*+} p_T range.

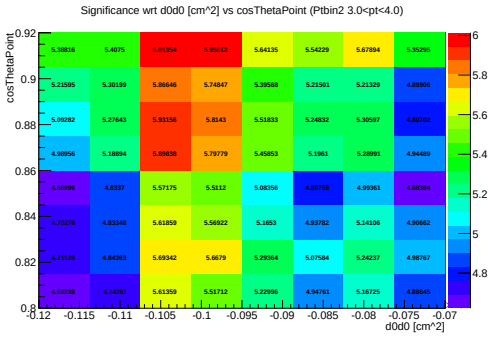

Figure 136: Significance values with respect to $d_0 \times d_0$ [cm^2] vs Cos θ_{point} for the 3-4 GeV/c D^{*+} p_T range.

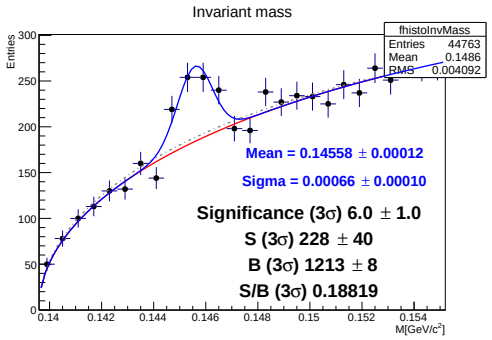

Figure 137: Invariant mass distribution of the K^-, π^+ combined with π_s pair, shifted back by the D^0 mass, with pair p_T range 3-4 GeV/c with the highest significance with respect to DCA, $d_0 \times d_0$ and Cos θ_{point}.

From figures 134, 135, 136 and 137 the optimal DCA is concluded to be between 0.2 and 0.35 mm, the product of impact parameters should be between -0.108 and -0.095 cm^2. The cosine of the pointing angle is optimally higher than is shown here, however this cannot be used as this makes selection criteria very instable. Therefore for all p_T ranges the range of the cosine of the pointing angle is limited to 0.92. The best cuts with respect to significance and within range of the optimization have been used for the spectrum.

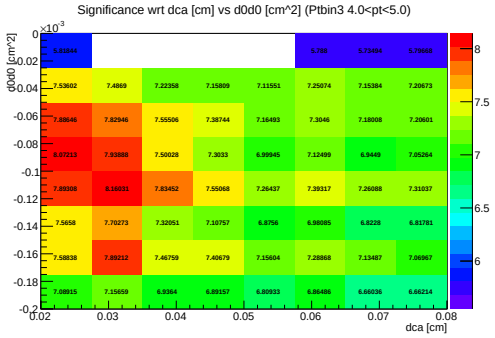

Figure 138: Significance values with respect to DCA [cm] vs $d_0 \times d_0$ [cm^2] for the 4-5 GeV/c D^{*+} p_T range.

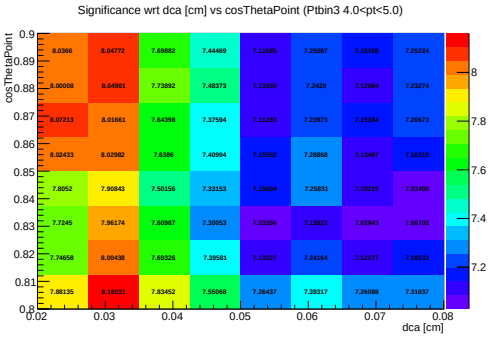

Figure 139: Significance values with respect to DCA [cm] vs Cos θ_{point} for the 4-5 GeV/c D^{*+} p_T range.

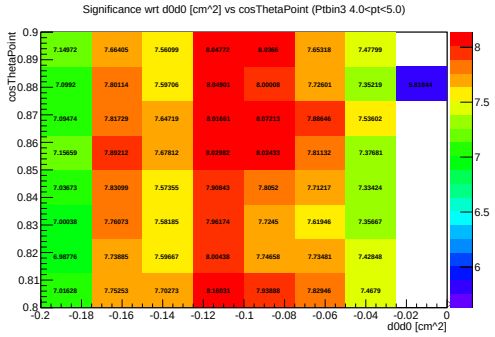

Figure 140: Significance values with respect to $d_0 \times d_0$ [cm^2] vs Cos θ_{point} for the 4-5 GeV/c D^{*+} p_T range.

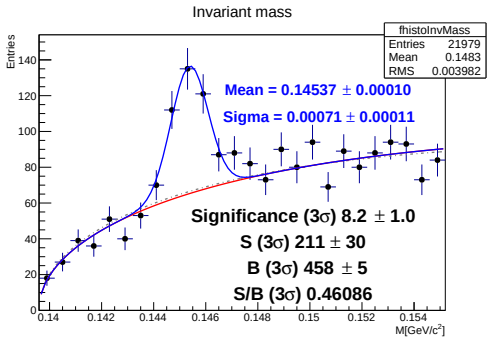

Figure 141: Invariant mass distribution of the K^-, π^+ combined with π_s pair, shifted back by the D^0 mass, with pair p_T range 4-5 GeV/c with the highest significance with respect to DCA, $d_0 \times d_0$ and Cos θ_{point}.

Figures 138, 139, 140 and 141 indicate that the optimal significance for this momentum range bin is found at approximately 0.03 cm for the DCA with a $d_0 \times d_0$ between -0.12 and -0.08 cm^2 and a relatively loose cosine angle of 0.8.

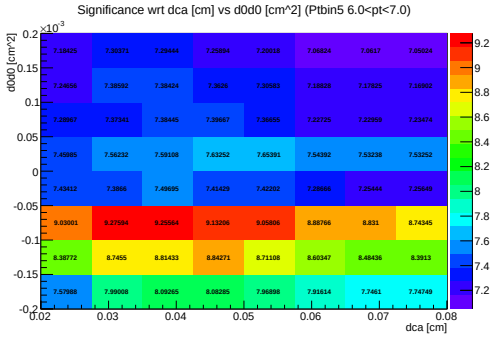

Figure 142: Significance values with respect to DCA [cm] vs $d_0 \times d_0$ [cm^2] for the 6-7 GeV/c D^{*+} p_T range.

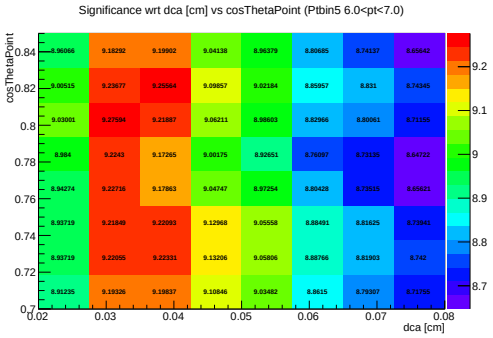

Figure 143: Significance values with respect to DCA [cm] vs Cos θ_{point} for the 6-7 GeV/c D^{*+} p_T range.

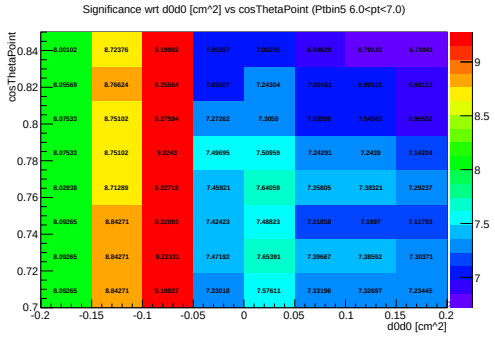

Figure 144: Significance values with respect to $d_0 \times d_0$ [cm^2] vs Cos θ_{point} for the 6-7 GeV/c D^{*+} p_T range.

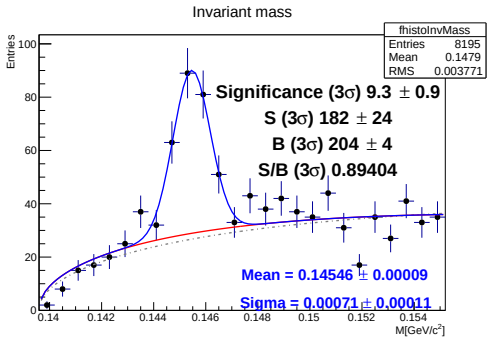

Figure 145: Invariant mass distribution of the K^-, π^+ combined with π_s pair, shifted back by the D^0 mass, with pair p_T range 6-7 GeV/c with the highest significance with respect to DCA, $d_0 \times d_0$ and Cos θ_{point}.

In previous optimization of minimum biased data sets the D^{*+} the optimal significance was received with looser $d_0 \times d_0$ selections, thus the optimization was done for a wide range. But as can been seen in figures 142 and 144, the preferable values are between -0.05 and -0.1 cm^2. In figure 143 it is shown that significance is higher for a DCA between 0.028 and 0.042 cm and a cosine of the pointing angle of approximately 0.8. Note that the significance in figure 145 is less than for the previous p_T range, but the signal over background is better than for the previous p_T range.

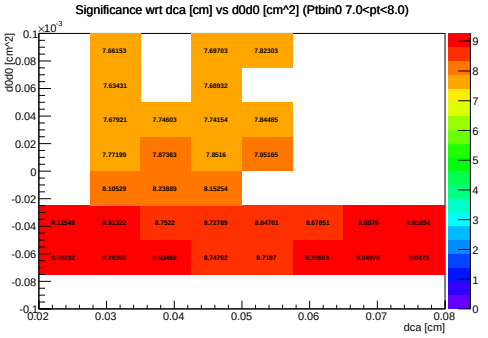

Figure 146: Significance values with respect to DCA [cm] vs $d_0 \times d_0$ [cm^2] for the 7-8 GeV/c D^{*+} p_T range.

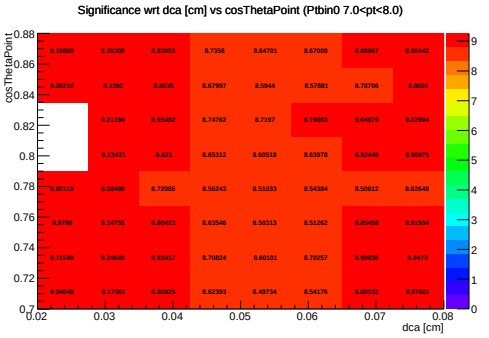

Figure 147: Significance values with respect to DCA [cm] vs Cos θ_{point} for the 7-8 GeV/c D^{*+} p_T range.

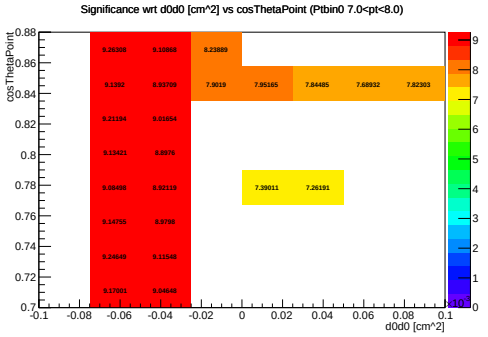

Figure 148: Significance values with respect to $d_0 \times d_0$ [cm^2] vs Cos θ_{point} for the 7-8 GeV/c D^{*+} p_T range.

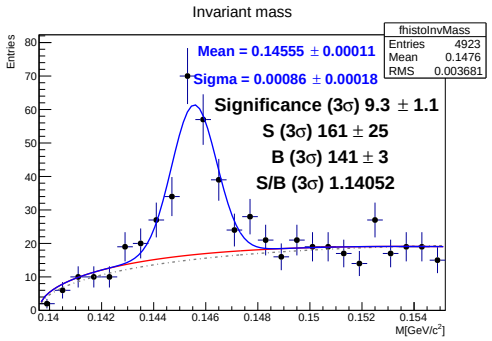

Figure 149: Invariant mass distribution of the K^-, π^+ combined with π_s pair, shifted back by the D^0 mass, with pair p_T range 7-8 GeV/c with the highest significance with respect to DCA, $d_0 \times d_0$ and Cos θ_{point}.

Note here that in figure 149 the peak is a little wide, this is just a fluctuation of the width. Figures 146, 147 and 148 differ from the other figures as there are zero values mentioned, which makes the other values seem more similar. This decreases the clarity of optimal value and was due to the earlier mentioned exclusion of overly wide fits. The significance peaks for a DCA of 0.3 cm, a $d_0 \times d_0$ of approximately -0.06 cm^2 and a cosine of 0.87. Note that these are quite strict cuts, rejecting a lot of background and some signal but resulting in a high significance.

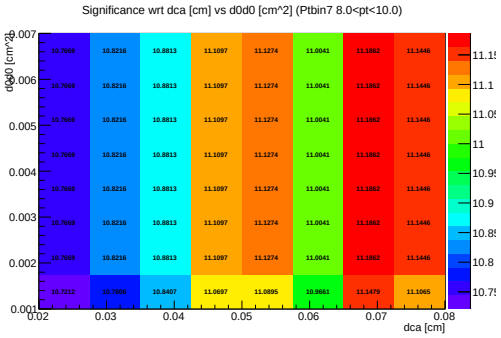

Figure 150: Significance values with respect to DCA [cm] vs $d_0 \times d_0$ [cm^2] for the 8-10 GeV/c D^{*+} p_T range.

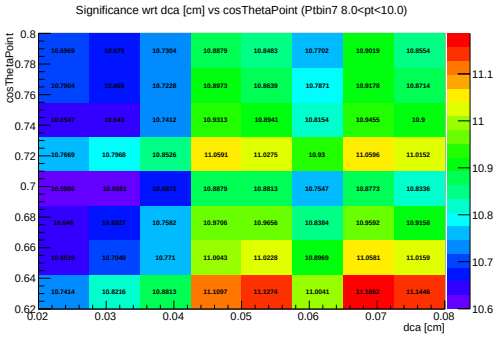

Figure 151: Significance values with respect to DCA [cm] vs Cos θ_{point} for the 8-10 GeV/c D^{*+} p_T range.

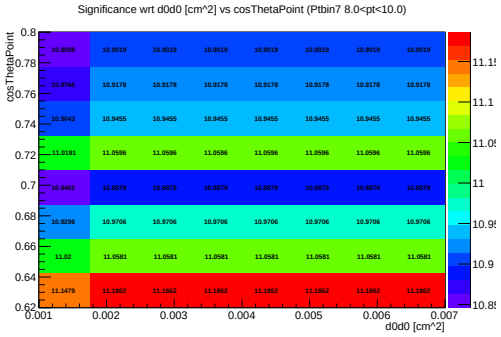

Figure 152: Significance values with respect to $d_0 \times d_0$ [cm^2] vs Cos θ_{point} for the 8-10 GeV/c D^{*+} p_T range.

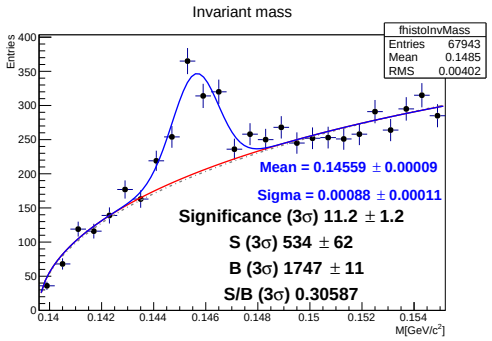

Figure 153: Invariant mass distribution of the K^-, π^+ combined with π_s pair, shifted back by the D^0 mass, with pair p_T range 8-10 GeV/c with the highest significance with respect to DCA, $d_0 \times d_0$ and Cos θ_{point}.

Figure 153 indicates that the significance is optimal for relatively loose cuts that will minimally effect on the signal. Here the optimal significance is found but it has a very low signal/background. From figure 150, 151 and 152 the optimum is found at a DCA of approximately 0.07 cm, a pointing angle of 0.62 and a $d_0 \times d_0$ of $\geq$0.002 cm^2.

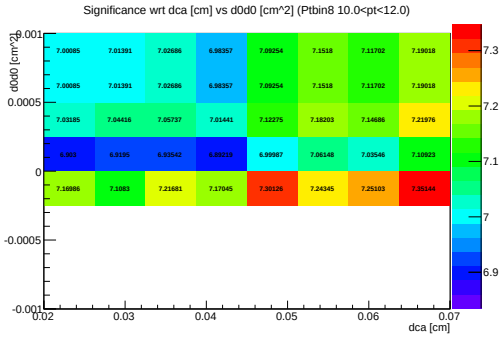

Figure 154: Significance values with respect to DCA [cm] vs $d_0 \times d_0$ [cm^2] for the 10-12 GeV/c D^{*+} p_T range.

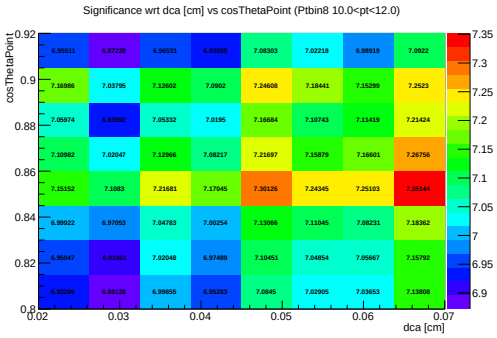

Figure 155: Significance values with respect to DCA [cm] vs Cos θ_{point} for the 10-12 GeV/c D^{*+} p_T range.

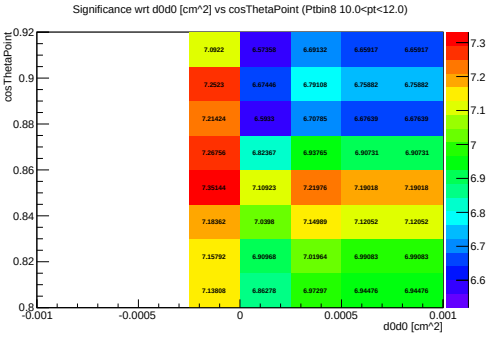

Figure 156: Significance values with respect to $d_0 \times d_0$ [cm^2] vs Cos θ_{point} for the 10-12 GeV/c D^{*+} p_T range.

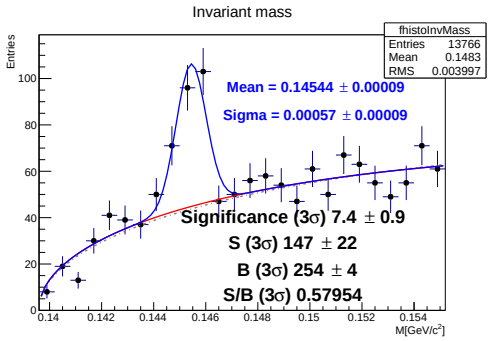

Figure 157: Invariant mass distribution of the K^-, π^+ combined with π_s pair, shifted back by the D^0 mass, with pair p_T range 10-12 GeV/c with the highest significance with respect to DCA, $d_0 \times d_0$ and Cos θ_{point}.

A comparison between the requirements for figure 157 and those for the previous momentum range concludes that the optimum is found at stricter requirements than the previous bin. As can be seen in figures 154, 155 and 156 the cuts are now limited via the fact that no proper fit could be found for tighter $d_0 \times d_0$ cuts. However, due to the efficiency, the optimal selection criteria with respect to the significance were exclude. To many real D^{*+} were excluded, as was seen in simulation of the data. A $d_0 \times d_0$ cut of 0.00035 and cosine angle of 0.84 and a loose DCA cut of 0.07 cm have been used.

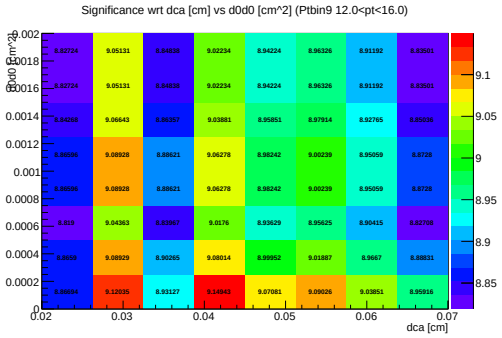

Figure 158: Significance values with respect to DCA [cm] vs $d_0 \times d_0$ [cm^2] for the 12-16 GeV/c D^{*+} p_T range.

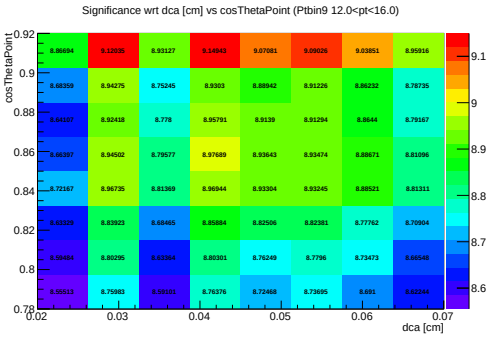

Figure 159: Significance values with respect to DCA [cm] vs Cos θ_{point} for the 12-16 GeV/c D^{*+} p_T range.

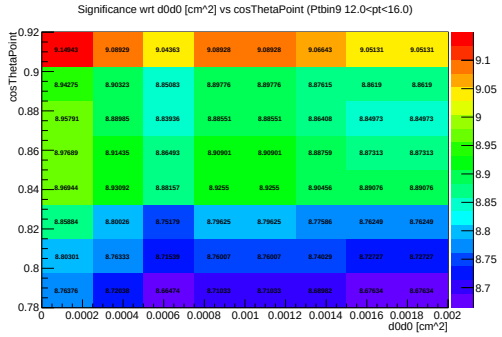

Figure 160: Significance values with respect to $d_0 \times d_0$ [cm^2] vs Cos θ_{point} for the 12-16 GeV/c D^{*+} p_T range.

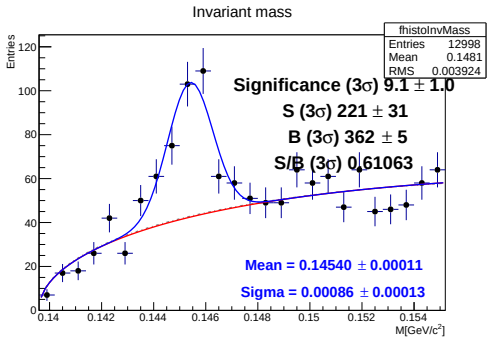

Figure 161: Invariant mass distribution of the K^-, π^+ combined with π_s pair, shifted back by the D^0 mass, with pair p_T range 12-16 GeV/c with the highest significance with respect to DCA, $d_0 \times d_0$ and Cos θ_{point}.

Figures 158, 159, 160 and 161 indicate the same effect with respect to the cos θ_{point} is seen as in the p_T range of $3-4$ GeV/c, the cosine angle is quite high (0.91). The $d_0 \times d_0$ is around 0 cm^2, and the DCA is 0.04 cm for the optimal significance.

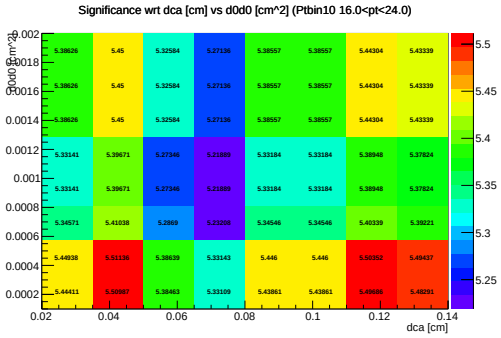

Figure 162: Significance values with respect to DCA [cm] vs $d_0 \times d_0$ [cm^2] for the 16-24 GeV/c D^{*+} p_T range.

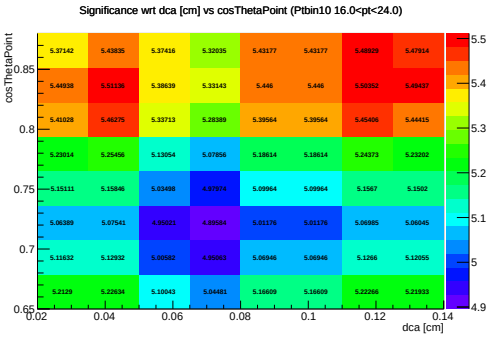

Figure 163: Significance values with respect to DCA [cm] vs Cos θ_{point} for the 16-24 GeV/c D^{*+} p_T range.

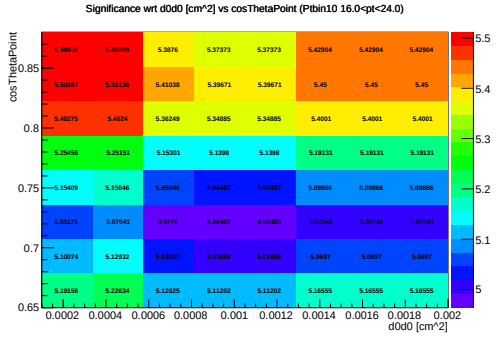

Figure 164: Significance values with respect to $d_0 \times d_0$ [cm^2] vs Cos θ_{point} for the 16-24 GeV/c D^{*+} p_T range.

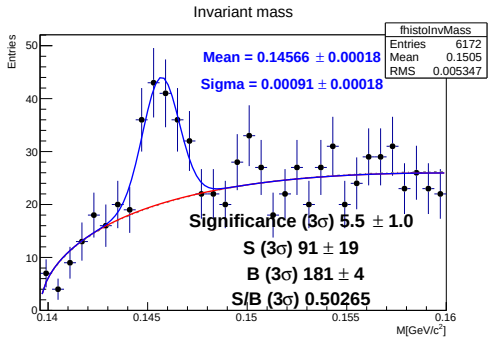

Figure 165: Invariant mass distribution of the K^-, π^+ combined with π_s pair, shifted back by the D^0 mass, with pair p_T range 16-24 GeV/c with the highest significance with respect to DCA, $d_0 \times d_0$ and Cos θ_{point}.

In figures 162, 163 and 164 and 165 indications are found for a loosely selected as well as a more strictly selected optimum. This is due to the fact that strict criteria also negatively influence the signal, thus the 0.04 DCA optimum contains less signal and less background than the 0.12 DCA optimum. For the angle and the $d_0 \times d_0$ there is one optimum, for the $d_0 \times d_0$ at 0.0004 cm^2 and for the angle for a cosine of 0.84.

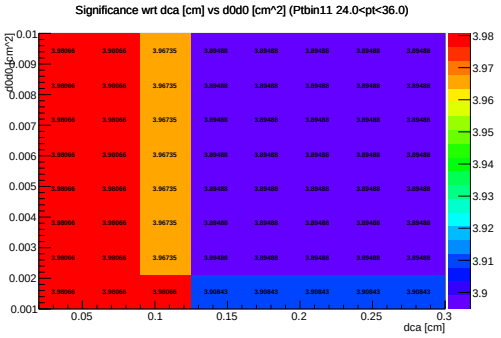

Figure 166: Significance values with respect to DCA [cm] vs $d_0 \times d_0$ [cm^2] for the 24-36 GeV/c D^{*+} p_T range.

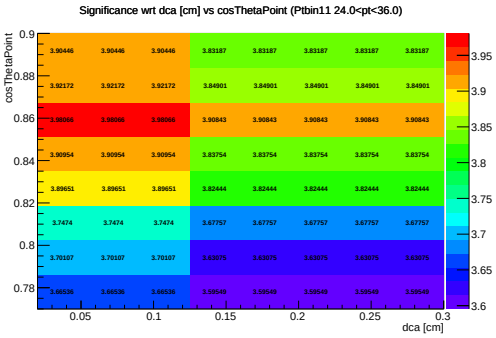

Figure 167: Significance values with respect to DCA [cm] vs Cos θ_{point} for the 24-36 GeV/c D^{*+} p_T range.

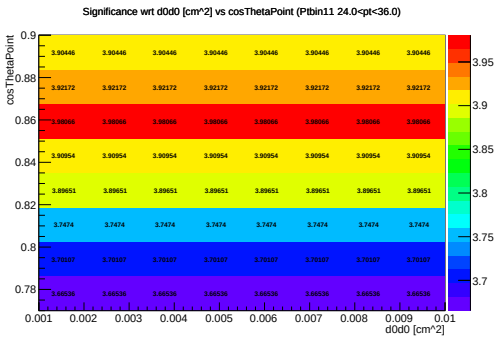

Figure 168: Significance values with respect to $d_0 \times d_0$ [cm^2] vs Cos θ_{point} for the 24-36 GeV/c D^{*+} p_T range.

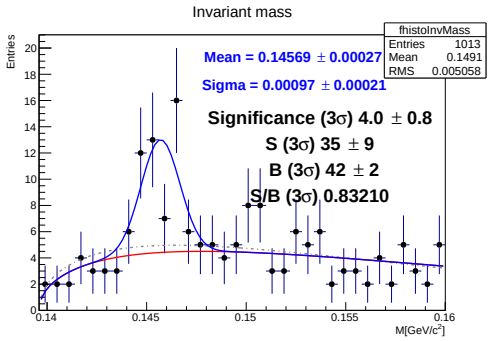

Figure 169: Invariant mass distribution of the K^-, π^+ combined with π_s pair, shifted back by the D^0 mass, with pair p_T range 24-36 GeV/c with the highest significance with respect to DCA, $d_0 \times d_0$ and Cos θ_{point}.

In the momentum range of figures 166, 167 and 168 not all requirements influence the significance. For a DCA strict enough (< 0.1 cm), the $d_0 \times d_0$ does not influence the significance. In this momentum range the cosine angle is the most important requirement with an optimal value of 0.86. For high momentum ranges earlier research has concluded that the requirements only mildly influences the significance. This is due to the low background in these ranges as can be seen in figure 169.

E Invariant Mass distribution of triggers combined

The combined triggers give an invariant mass distribution shown in figure 170.

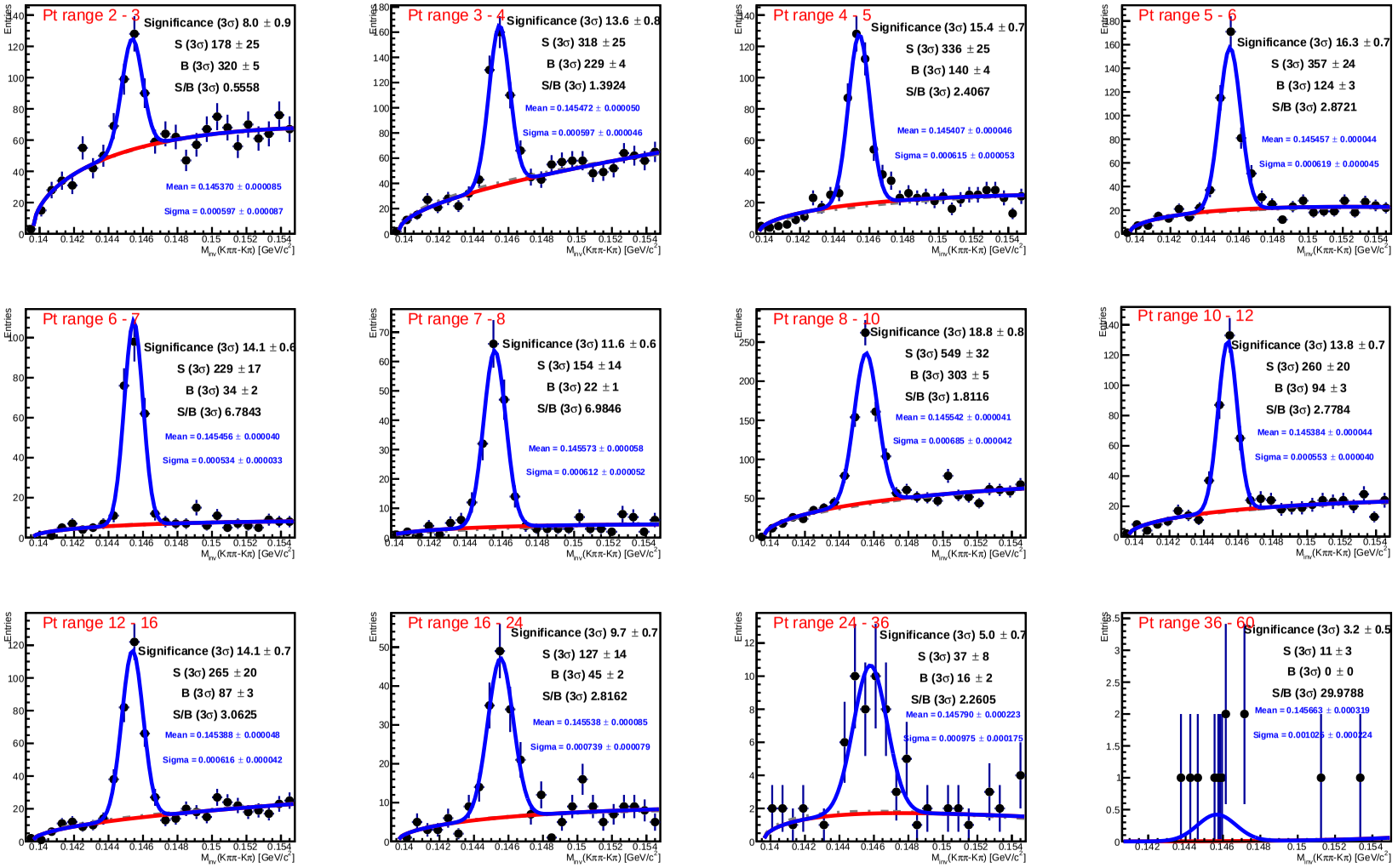

Figure 170: Invariant mass distribution of the $K^-\pi^+$ pair combined with π_s, shifted back by the D^0 mass, with pair p_T range 2-36 GeV/c, EMCal 7/8 & INT 7/8 & SPI 7/8 trigger for pp collision at $\sqrt{s} = 8$ TeV, uncorrected for overlap.

References

[1] ALICE Environment for the GRID. http://alien2.cern.ch.

[2] An object-oriented data analysis framework. http://root.cern.ch.

[3] K. Aamodt et al. The ALICE experiment at the CERN LHC. *JINST*, 3:S08002, 2008.

[4] B. Abelev et al. Measurement of charm production at central rapidity in proton-proton collisions at $\sqrt{s} = 7$ TeV. *JHEP*, 1201:128, 2012.

[5] B. Abelev et al. Suppression of high transverse momentum D mesons in central Pb-Pb collisions at $\sqrt{s_{NN}} = 2.76$ TeV. *JHEP*, 1209:112, 2012.

[6] ALICE Collaboration. *ALICE Photon Multiplicity Detector (PMD): Technical Design Report*. Technical Design Report ALICE. CERN, Geneva, 1999.

[7] Alme, J. et al. The ALICE TPC, a large 3-dimensional tracking device with fast readout for ultra-high multiplicity events. *Nuclear Instruments and Methods in Physics Research A*, 622:316–367, Oct. 2010.

[8] J. Beringer et al. The review of particle physics. *Phys. Rev.*, D86:010001, 2012.

[9] M. Cacciari, M. Greco, and P. Nason. The P(T) spectrum in heavy flavor hadroproduction. *JHEP*, 9805:007, 1998.

[10] P. Cortese et al. *ALICE forward detectors: FMD, TO and VO: Technical Design Report*. Technical Design Report ALICE. CERN, Geneva, 2004. Submitted on 10 Sep 2004.

[11] English Wikipedia, user MissMJ, based upon Nova, Fermilab, PDG. Standard Model of Elementary Particles, http://en.wikipedia.org/ (Standard Model), 2006.

[12] I. Foster and C. Kesselman, editors. *The grid: blueprint for a new computing infrastructure*. Morgan Kaufmann Publishers Inc., San Francisco, CA, USA, 1999.

[13] M. Kweon. The Transition Radiation Detector for ALICE at LHC. *Nucl. Phys.*, A830:535C–538C, 2009.

[14] G. Martinez. Advances in Quark Gluon Plasma. *ArXiv 1304.1452 e-prints*, 2013.

[15] L. Molnar. The ALICE HMPID detector ready for collisions at the LHC. *Nucl. Instrum. Meth.*, A595:27–30, 2008.

[16] P. Christiansen for the ALICE Collaboration. High pt identified particle production in ALICE. *ArXiv 1208.5368 e-prints*, 2012.

[17] C. Pagliarone and A. Fernandez-Tellez. Cosmic Ray Physics with ACORDE at LHC. *J. Phys. Conf. Ser.*, 110:062021, 2008.

[18] Piotr Kukla. D^{*+} analysis in proton-proton collisions at $\sqrt{s} = 2.76$ TeV using the ALICE detector at CERN. Master's thesis, Utrecht University.

[19] Rene Bellwied for the ALICE EMCal Collaboration. ALICE EMCal Physics Performance Report. *ArXiv 1008.0413 e-prints*.

[20] S. Siddhanta et al. The readout system for the ALICE zero degree calorimeters. *IEEE Trans. Nucl. Sci.*, 58(4):1759–1765, 2011.

[21] A. Smilga. *Lectures on Quantum Chromodynamics*. World Scientific Publishing Company, 2001.

[22] The ALICE experiment. Detector layout, http://aliceinfo.cern.ch/Figure/.

[23] The ALICE experiment. Offline project, http://aliweb.cern.ch/Online/AliRoot/Manual.html.

[24] The ALICE experiment. Our Mission, http://www.aliweb.cern.ch.

[25] Walter Greiner, Stefan Schramm, Eckart Stein. *Quantum Chromodynamics, 3rd edition.* Springer, 2007.

[26] B. Zakharov. Nuclear modification factor for light and heavy flavors within pQCD and recent data from the LHC. *JETP Lett.*, 96:616–620, 2013.

[27] X. Zhang, D. Zhou, and W. Xiang. Dead cone effect of heavy quark in medium. *Int.J.Mod.Phys.*, E16:2123–2129, 2007.

[28] D. C. Zhou and the ALICE Collaboration. PHOS, the ALICE-PHOton spectrometer. *Journal of Physics G: Nuclear and Particle Physics*, 34(8):S719, 2007.